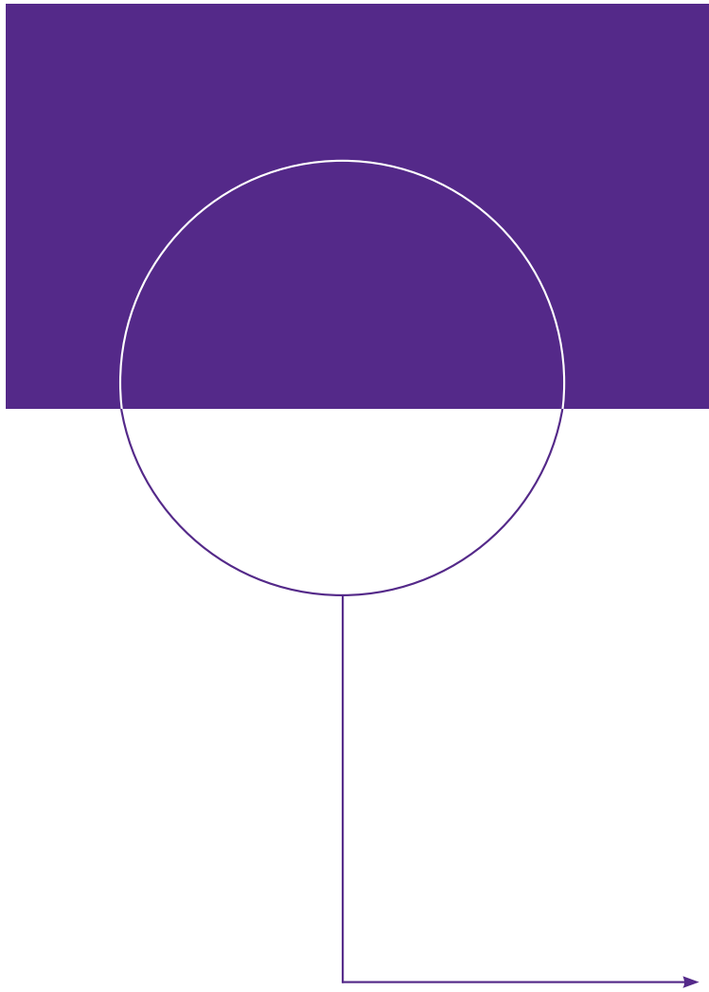

Master's thesis

2020

Kishore Rajendran

NTNU
Norwegian University of
Science and Technology
Faculty of Natural Sciences
Department of Chemical Engineering

Kishore Rajendran

Design and setup optimization of ex-situ catalytic up-gradation of renewable biomass into fuel range hydrocarbons

August 2020

NTNU
Norwegian University of
Science and Technology

NTNU
Norwegian University of
Science and Technology

NTNU

Norwegian University of
Science and Technology

Design and setup optimization of ex-situ catalytic up-gradation of renewable biomass into fuel range hydrocarbons

Kishore Rajendran

Chemical Engineering
Submission date: August 2020
Supervisor: Professor De Chen
Co-supervisor: Associate Professor Kumar Ranjan Rout

Norwegian University of Science and Technology
Department of Chemical Engineering

Abstract

The fast depleting fossil fuel reserves and its environmental impact paved the path for alternative renewable resources. Bio-fuel portrays an attractive opportunity to substitute conventional fossil fuels. This leads to positive driven effects on the environment and reduced dependency on fossil fuels. The recent Paris agreement in 2015 had provided momentum for the renewable energy market in the near future. In this regard, Norway sets an ambitious goal to reduce half of its current greenhouse gas emission from the transportation sector by 2030. This is set by replacing at least 30% of aviation fuel by biofuels. Therefore, the development and up-scaling of the new and established biomass conversion technology had currently piqued the interest. Limited biomass conversion technology had progressed to production level at pilot scale. In this work, inspired by H_2-Bio-oil technology and atmospheric pressure working condition, small scale fast catalytic screening setup was developed. The experimental setup involved two fixed-bed tubular reactors in series, in which non-catalytic hydropyrolysis was conducted in the first reactor, and ex-situ catalytic up-gradation is carried out in the second reactor. The biomass feeding compartment, biomass feeding device, biomass calibration, tubular reactor, temperature calibration, condenser and condensing medium had been extensively optimized in the final experimental setup. Further, the GC instruments were calibrated to quantify the gaseous and liquid products from the successful experiments.

Tandem catalytic system was approached in the ex-situ catalytic up-gradation of non-catalytic biomass hydropyrolysis products. The main objective was to upgrade smaller oxygenates (C3-C7) by the carbon-carbon coupling reaction (ketonization and aldol condensation) and consecutive hydrodeoxygenation to improve the yield and quality of bio-oil. To validate the setup, carbon-carbon coupling catalyst, 0.5, 1, 3 and 7 wt.% Cu-TiO_2, 1 wt.% Ru/TiO_2, 1 wt.% Au/TiO_2 and hydrodeoxygenation catalyst 1 wt.% Ru-MoFeP/Al_2O_3 was synthesized. The prepared catalyst was characterized by BET, XRD, SEM, NH_3-TPD and CO_2-TPD and briefly discussed its catalyst structural and surface properties such as specific surface area, crystallinity, surface morphology, acidity and basicity. However, the synthesized catalyst could not be validated due to numerous technical difficulties faced during the development of the setup. To get a better understanding over the catalytic system, an overview of the last ten years of literature study on the atmospheric carbon-carbon coupling and hydrodeoxygenation catalyst had also been presented.

Preface

The master thesis was completed in the KinCat group at the Department of Chemical Engineering, Norges Teknisk-Naturvitenskapelige Universitet (NTNU), Trondheim, Norway. The project on biomass to fuel conversion started with optimization of the H_2-Bio-oil mini pilot plant during the Autumn 2019 specialization project.

The master thesis started with a preliminary plan to synthesize active carbon-carbon coupling/hydrodeoxygenation catalyst to test in the H_2-bio-oil mini-pilot plant and correlate the findings with Density Functional Theory study. Unfortunately, there was no small scale experimental setup available for screening the active catalyst. In this regard, hydropyrolysis with ex-situ up-gradation reactor similar to H_2-Bio-oil setup configuration was developed. Therefore, the majority of the time was spent in developing a fast active catalyst screening unit for H_2-Bio-oil plant during the master thesis. However, the limited technical support and time restriction on-campus, which is crucial for the completion of this project became an unexpected scenario due to the COVID-19 pandemic. Therefore, the final testing phase with the catalyst in the developed setup could not be completed as planned. Additionally, this master thesis also provides an extensive review of the atmospheric hydrodeoxygenation and carbon-carbon coupling catalyst reported in the last ten years.

I want to express my deepest gratitude to my supervisor Professor De Chen, and my co-supervisor Associate Professor Kumar Ranjan Rout, for their insightful suggestions and feedback during the ceaseless modification for building the experimental setup from scratch.

I would like to thank Zhenping Cai (Postdoc.), Dumitrita Spinu (PhD Student, NTNU), Martina Cazzolaro (PhD Student, NTNU) for their valuable suggestions, assistance and technical support.

Special thanks to staff engineer Ketil Torset Helland and Erland Strendo who helped to modify the experimental setup countless times on short notice during these stressful periods.

Table of Contents

List of Tables

List of Figures

Abbreviations

LHV	Lower Heating valve
IH^2	Integrated Hydropyrolysis and Hydroconversion
GTI	Gas Technology Institute
GC	Gas Chromatographyy
MS	Mass Spectrometer
FID	Flame Ionization Detector
TCD	Thermal Conductivity Detector
HPLC	High Pressure Liquid Chromatography
HRMS	High Resolution Mass Spectroscopy
NMR	Nuclear Magnetic Resonance
FTIR	Fourier Transform Infrared Spectroscopy
LLE	Liquid-Liquid Extraction
SFE	Supercritical Extraction
GPC	Gel Permeation Chromatography
SPE	Solid Phase Extraction
SPME	Solid Phase Micro Extraction
SMR	Steam Methane Reformer
C-C	Carbon-Carbon
AC	Activated Carbon
DDO	Direct Deoxygenation
HDO	Hydrodeoxygenation
CNF	Carbon Nano Fiber
BTX	Benzene, Xylene, Toluene
FCC	Fluid Catalytic Cracking
PAH	Poly Aromatic Hydrocarbon
WHSV	Weight Hourly Space Velocity
BET	Brunauer–Emmett–Teller
BJH	Barrett-Joyner-Halenda
XRD	X-Ray Diffraction
TPD	Temperature Programmed Desorption
S(T)EM	Scanning Transmission Electron Microscope
SEM	Scanning Electron Microscope
EXD	Energy-Dispersive X-ray
SS	Stainless Steel
RBF	Round Bottom Flask

Chapter 1

Introduction

1.1 Motivation

At present, the rise in energy demand had been intertwined together with the world's population. The current world's energy demand is majorly fueled by fossil fuels such as petroleum (33%), coal (24%) and natural gas (19%) [2]. Herein, 94 % of global transport is dominantly fulfilled by fossil fuel [3]. This is widely due to the high hydrogen/carbon ratio coupled with high volumetric efficiency of fossil fuels available at low-cost [4]. Diminishing petroleum reserves, rising energy demand, environmental regulation, political push and slow regeneration of fossil-derived fuels had motivated human community to make a transition from fossil fuel energy towards the renewable energy sources [5, 6].

Biomass as an energy source had been used throughout the existence of humankind [7]. However, advancement in biomass conversion technology had shown slow progress due to relatively complete replacement by coal and consecutively by crude oil and natural gas in order to compensate the surge in energy demands in the past two centuries [7]. Until recently, biomass conversion technology had shown renewed interest due to depletion of fossil reserves, increased greenhouse gas (CO_2 levels had increased from $\approx$ 280 to $\approx$ 380 ppm compared to pre-industrial concentration, as reported in 2004), ozone layer depletion, the release of volatile organic compounds, soot particles from conventional fuel sector and so on [7]. The recent Paris treaty signed by 195 countries in order to limit the temperature rise by 1.5°C in the upcoming years had also probed the human community to invest in biomass to fuel conversion technology [8].

At present, the biomass is the only sole renewable source of organic carbon. Therefore, the only sustainable source of liquid hydrocarbon transportation fuel is biofuel [9]. The biofuels can be categorized into three different generation where the Third generation biofuel from algae is still in the development stage. The First generation biofuel from edible biomass (simple sugars, starch, vegetable oil) was highly successful with the existing fuel technology, however, intervening with the food supply, expensive feedstock had been highly debated to continue its production [10]. The Second generation biofuel had

shed lights in terms of non-intervention in food supply due to non-edible biomass content (forest, municipal, household, agriculture residue, dedicated energy crops) and the low cost of feedstock [10]. Despite processing difficulties, second generation feedstocks portrays a sustainable source for delivering renewable hydrocarbon fuels and chemicals [3]. Therefore, renewed attention had been dedicated in improving the technologies for fuel and energy production from Second generation biomass feedstock.

The conversion of complex raw biomass into fuels is accompanied by unaided fuel properties such as Lower Heating Value (LHV), diverse chemical composition, high oxygen content, reactive chemical components and poor miscibility with conventional fossil fuels. Consequently, the biofuel becomes incompatible as an drop-in fuel in transportation sector and speciality chemicals [3, 11, 12, 13]. Therefore, catalytic up-gradation is necessary for successful utilization of the biomass-derived products in the transportation and chemical sector. Thus, prolonged research activity, including this master thesis, is devoted to the conversion of biomass to fuel range compounds and chemicals.

1.2 Objective

The main objective of the master thesis are as follows:

- Review the progress of carbon-carbon coupling and hydrodeoxygenation reaction of biomass-derived oxygenates at atmospheric pressure condition in the past ten years;
- Preparation and characterization of carbon-carbon coupling and hydrodeoxygenation catalysts;
- To build and optimize laboratory catalyst screening set-up of hydropyrolysis with ex-situ up-gradation reactor; and
- Optimize the quantification methods for liquid via GC/FID/TCD and gaseous product via GC/FID/MS.

Chapter 2

Literature Review

2.1 Biomass

The lignocellulosic biomass is mainly comprised of three polymers, namely cellulose, hemicellulose and lignin. The composition of the polymers varies from plant species to species with geographical location. For example, poplar and pine belongs to the same species, yet cellulose composition varies 50 and 28%, respectively. Typical cellulose, hemicellulose and lignin in a lignocellulose material varies from 30-35%, 25-30% and 10-30%, respectively. Other minor components include ash, water, lipids and proteins [14, 15]. Herein, A short overview on the components of the lignocellulose will be discussed.

2.1.1 Cellulose

Cellulose is one of the main structural components of the cell wall. It is comprised of linear chains of D-glucose units, as shown in figure 2.1. β (1-4) linkages bonds the two D-glucose units in the cellulose. A high degree of polymerization of the cellulose monomers is observed to reach up to 10,000 units. The cellulose is insoluble in dilute acid/alkali at ambient temperature. Cellulose is widely utilized in the paper and pulp industry. Further, an extensive investigation had been subjected for production of speciality chemical from cellulose [14].

2.1.2 Hemicellulose

Hemicellulose consists of five and six-carbon sugar as opposed to cellulose polymer, as observed in figure 2.1. The former includes arabinose, xylose, and the latter comprises of glucose, galactose. The crucial function of hemicellulose is to adjust the chemical process in plant cell growth and resistance against cell wall degradation.

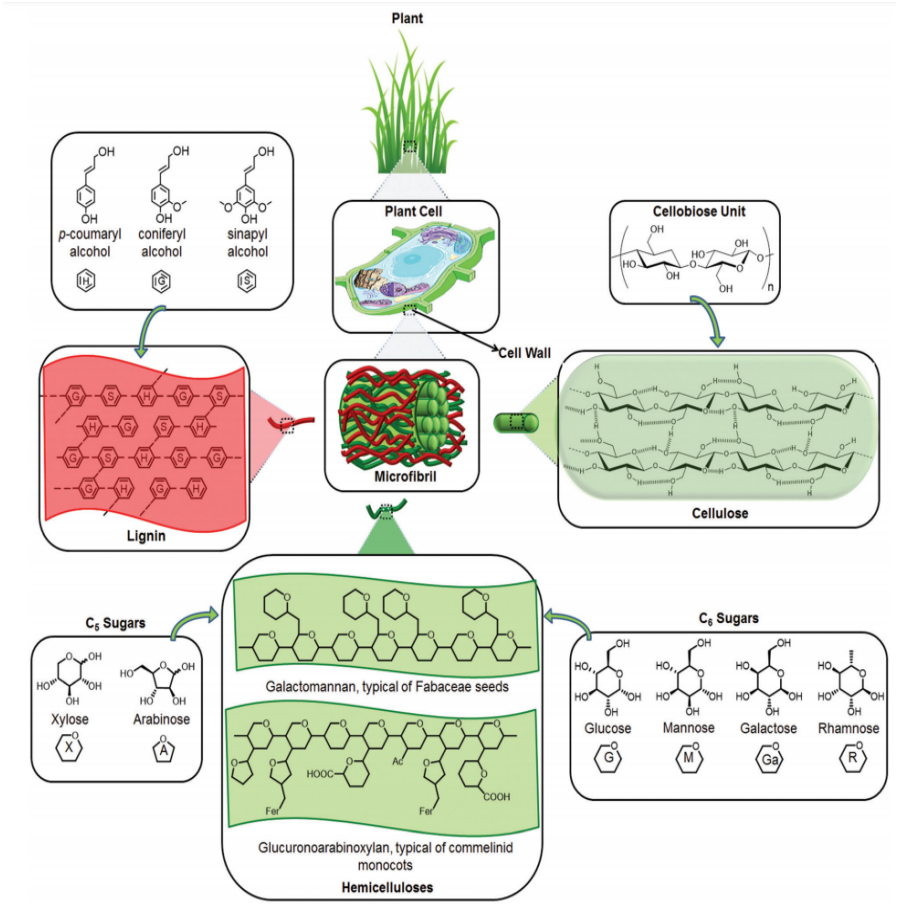

Figure 2.1: Different components of lignocellulose. "GI" – glucuronic acid and "Fer" – esterification with ferulic acid [16]

2.1.3 Lignin

The lignin is a polymer which binds the cellulose and hemicellulose polymer intact in the plant tissue, thereby aiding in structural strength and stiffness. The primary function of lignin is to minimise the harmful effects caused by insects and pathogens. The polymer mainly consists of phenylpropanoid polymer (aromatic and C3 chain), as shown in figure 2.1. The complex structure of lignin is derived from three monolignols: p-coumaryl alcohol, coniferyl alcohol and sinapyl alcohol, as shown in figure 2.1. After polymerization of the three monolignols, three central units to represent lignin structure are p-hydroxylphenyl propanol, guaiacyl-propanol and syringyl-propanol compound. Depending on the plant species and geographical location, the ratio of the three units is varied. This variation causes lignin polymer to be classify into three categories: softwood lignin, hardwood lignin, and grass lignin [16].

2.2 Bio-fuel

Biofuel shares high contribution up to 13% among the non-fossil fuel energy sources such as hydropower, wind power and nuclear power. The biofuel is attributed to its renewable nature, wide availability, low carbon footprint, and sulphur content [1]. Currently, biofuel has a profound application in heat/power generation, speciality chemicals, fertilizer, pesticides etc [11]. The recent Paris-agreement signed in 2015 to limit the temperature rise to 1.5°C compared to pre-industrial levels had increased the momentum for biomass conversion technology to fuels and chemicals [8]. In this regard, global biofuel production had been steadily rising and forecasted to reach 190 billion litres in 2024, thereby reducing the dependency on fossil fuels. A recent study conducted in the U.S. reports that about 31% of total petroleum consumption can be replaced by the biofuel with minimal interference with the food and feed sector [17]. Overall, the biofuel conversion technologies had received immense attention in the past decades.

The available lignocellulosic biomass conversion techniques to fuel and chemicals include thermochemical, biochemical and physical pathway [18]. A crucial factor for these technologies to co-exist in collaboration with the current energy sector are as follows; type of biomass species, availability, economics, environmental regulation, and the efficiency of process equipment [1]. In this regard, the thermochemical route for biomass conversion had been shown promising towards commercialization compared to other routes. This is attributed to its low capital investment, operational cost, utilization of entire biomass coupled with feedstock flexibility, short processing time, non-consumption of enzymes/microbes, solvent separation [3, 9, 18]. The current thermochemical conversion technology is discussed in section 2.5.

Physical property	Bio-oil	Physical property	Bio-oil
Moisture content (wt.%)	15-30	pH	2.5
Specific gravity	1.2	Ash	0-0.2
C (wt.%)	54-58	Higher heating value (MJ/Kg)	16-19
H (wt.%)	5.5-7	Viscosity @ 50° C (cP)	40-100
O (wt.%)	35-40	Solids (wt.%)	0.2-1
N (wt.%)	0-0.2	Distillation residue (wt.%)	50

Table 2.1: Elemental composition and properties of non catalytic biomass pyrolysis [19]

The thermochemical conversion of biomass is processed by the application of heat in an oxygen-deficient atmosphere. This converts the cellulose, hemicellulose and lignin fraction of lignocellulosic material into valuable hydrocarbon, which can be utilized in fuel and speciality chemical sector [3, 20]. A summary on the elemental analysis of the thermochemically treated wood is shown in table 2.1 [19]. The high oxygen content (35-40 wt.%) and water content (15-30.%) are inevitable products and affect the higher heating value, which will be discussed later in this section. The primary decomposition pathways in the thermochemical conversion of wood are shown in figure 2.2 [21]. Majority of the non-catalytic pyrolysis of wood follows dehydration (liberates H_2O), fragmentation of the carbon bonds, isomerization and repolymerization via unstable intermediates.

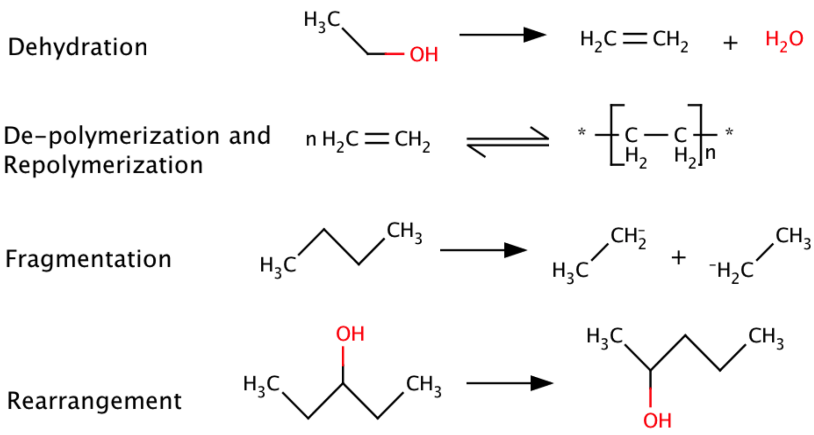

Figure 2.2: Chemical reaction during non-catalytic pyrolysis [21]

It is evident from the above discussion that, bio-oil (pyrolysis oil) is vitally produced via depolymerization and fragmentation of different components of biomass (cellulose, hemicellulose and lignin). Overall, the bio-oil from pyrolysis compared to other thermo-chemical conversion technique, mainly consists of the organic and aqueous fraction, as shown in the figure 2.3. The properties of bio-oil include: 1) Dark brown in appearance, 2) High viscosity and pH, 3) Solid particles (aerosols), 4) High level of oxygen content as observed from in table 2.1, and 5) Stinging odour of grilled biomass [22]. The bio-oil is further characterized by its complex nature of chemical compounds as a result of the random breakdown of the wood's chemical structure. As a consequence, the complete chemical characterization of the bio-oil becomes challenging due to the presence of simple sugars to multifunctional chemical compounds which will be discussed in section 2.8 [23]. Other pyrolysis products, such as char and gas is also produced along with bio-oil.

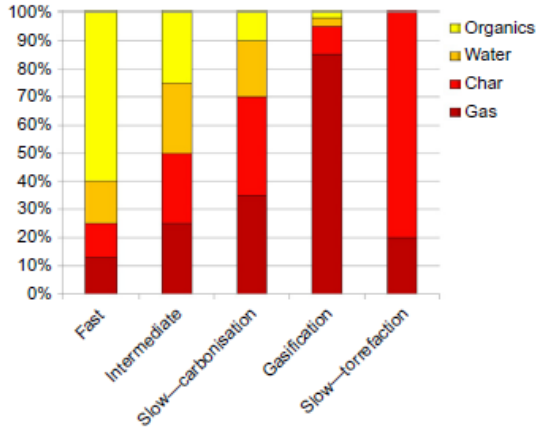

Figure 2.3: Product distribution from non-catalytic pyrolysis of wood. Note: Fast and intermediate refer to variations in pyrolysis process [1]

2.3 Thermochemical conversion techniques

There are four modes of thermochemical conversion techniques such as pyrolysis, gasification, liquifaction and combustion. Others include coke formation and water removal from biomass by carbonisation and torrefaction. Table 2.2 shows its corresponding primary products and commercial application. The pyrolysis is endothermic, whereas gasification is an exothermic process. The former leads to liquid, solid and gases products via decomposition of biomass in the oxygen-deficient atmosphere. On the other hand, the latter produces mostly gaseous product in the presence of limited oxygen/steam (known as syngas in Fischer-Tropsch synthesis for the production of gasoline/diesel range hydrocarbons). Similar to pyrolysis, and gasification, liquefaction and combustion are endothermic and exothermic in nature, respectively. However, differences arise in biomass processing. The liquefaction process converts the wet biomass at elevated pressure into liquid and gaseous products whereas the combustion mainly results in heat, CO_2 and H_2O due to complete oxidation of biomass in an oxygen-rich atmosphere [1].

Thermochemical pathway	**Primary product**	**Commercial Application**
Pyrolysis	Gas, liquid, char	Fuels and chemicals
Liquifaction	Liquid	Fuels and chemicals
Gasification	Gas	Fuel gas
Combustion	Gas, char	Heating

Table 2.2: Primary products and application from thermochemical conversion routes [24]

The superiority of pyrolysis over other thermochemical pathways are due to good storage and transport property, which gives reasonable flexibility in the production of liquid and gaseous hydrocarbon fuels. Based on the type of reactor, residence time and reactor gas atmosphere, there exist 6 different modes of pyrolysis: 1) Fast pyrolysis, 2) Slow pyrolysis, 3) Intermediate pyrolysis, 4) Flash pyrolysis, 5) Vacuum pyrolysis, and 6) Ablative pyrolysis. A common similarity between these modes of pyrolysis is the common product distribution consisting of organic phase, aqueous phase, solid char, light gas and permanent gases such as CO, CO_2, CH_4, H_2. However, the weight percentage of the distribution of the product varies. Therefore, in practice, the product distribution of each component is varied by manipulating the temperature, pressure, residence time and controlling the extent of a secondary reaction in gas phase. [12, 25].

The liquid yield is given the major priority in the production of fuels and chemical via pyrolysis. In this regard, fast pyrolysis is reported to be promising due to its high liquid yield of 70-80 wt.% (dry feed basis), as shown in table 2.3 [1]. This is attributed to the high heating rate of biomass and short residence time of the gas vapours via rapid cooling in the fast pyrolysis reactor. This prevents the primary volatile gaseous fraction undergoing repolymerization and cracking reaction to produce additional gases and char [26]. These characteristics of the fast pyrolysis process led to commercialization at pilot plant stage [13, 12].

Mode	Condition	Liquid	Solid	Gas
Fast	500°C. Short hot vapour residence time 2 sec	75 wt.%	12 wt.%	13 wt.%
Intermediate	500°C. Moderate hot vapour residence time 5-30 sec	50 wt.%	25 wt.%	25 wt.%
Carbonisation	400°C. Long hot vapour residence time hours-days	30 wt.%	35 wt.%	35 wt.%
Gasification	750-900°C. Moderate hot vapour time 5 sec	3 wt.%	1 wt.%	96 wt.%
Torrefaction	280°C, Solids residence time 10-60 min	0-15 wt.%	80 wt.%	20 wt.%

Table 2.3: Product distribution via various thermochemical routes [1]

2.4 Bio-oil up-gradation

The merits of fast pyrolysis are followed by its disadvantages as well. Firstly, high oxygen content in bio-oil lowers the heating value compared to gasoline/diesel fuels (42-44 $\mathrm{MJ\,kg^{-1}}$), as previously shown in table 2.1. Secondly, poor miscibility in conventional fuel due to aqueous products including unstable ketone and acids. These further lead to increase in viscosity [6]. Thirdly, delay in the ignition period due to the presence of water [12, 13]. Fourthly, poor thermal stability due to high molecular weight chemical compounds and oxygenates [11]. Overall, these factors lead to poor fuel characteristic and storage property. This non-catalytic bio-oil is similar in characteristic to the complexity of petroleum residue [3]. Ultimately, the direct utilization of biofuel as a drop-in fuel in the transportation sector or fuel substituents is hindered. Therefore, the bio-oil must be upgraded to overcome its detrimental properties.

The bio-oil can be upgraded by the selective removal of the oxygenates [27]. On average, nearly 40 wt.% of the oxygen present in wood ends up in the bio-oil, as observed from the table 2.1. Therefore, adverse properties of the bio-oil depend on the concentration of oxygenates present in the bio-oil. The earlier approaches include the hydrotreating of re-evaporated bio-oil in the presence of precious noble metals and sulphided CoMo and NiMo in H_2 environment [6, 13]. In this regard, many issues such as elevated pressure (100-170 bar), high volumetric consumption of H_2 relative to the mass of bio-oil had to be faced. In addition, up-gradation of pyrolysis oil already has a massive influence on the economics of the final product. The prevalent influential factors include biomass harvesting, drying, chipping, storing, transportation and pyrolysis process. Therefore, the elevated pressure and high hydrogen consumption for hydrotreatment of bio-oil seem uneconomical [11, 12].

The hydropyrolysis is an attractive option to avoid utilization of external hydrotreater unit. Herein, the thermal degradation (400-600 °C/s) of the biomass occurs in hydrogen instead of inert (nitrogen, helium, argon) atmosphere inside pyrolysis reactor [3, 13]. M. Steinberg et al. introduced the concept of hydropyrolysis, which was previously termed as flash pyrolysis in H_2 atmosphere/ flash hydropyrolysis. A comprehensive comparison be-

tween the pyrolysis, fast pyrolysis and hydropyrolysis has been reported by M. Steinberg et al. [28]. It was observed that the partial pressure of hydrogen influences the proportion of liquid wt.% of the bio-oil. The volatile fraction increased in the order: pyrolysis $<$ flash pyrolysis $<$ hydropyrolysis. Other literature studies also support the improved product distribution of hydropyrolysis compared to its competitors [13, 29]. Overall, the hydropyrolysis seems to be an attractive option compared to hydrotreater and other pyrolysis routes.

2.5 Pyrolysis reactors

There are six reactor available for conducting biomass pyrolysis [23]. These include the fixed bed, fluidized bed, rotating cone, ablative, vacuum and auger reactor, as shown in figure 2.4. The above-mentioned pyrolysis reactor tries to function on the fast pyrolysis principle to deliver high heating rates and short residence time for condensable gaseous products. However, the dissimilarity arises between the bio-oil yield and operational flexibility. A short overview on advantage and disadvantage of each reactor will be discussed.

The fixed bed configuration is shown in figure 2.4 (a). The catalyst is placed inside the reactor, whereas the biomass is introduced either with the catalyst or after the desired setpoint temperature is reached. The sweep gas is either inert (He, Ar, N_2) or reactive (H_2, CH_4). The char remains a residue inside the reactor. In the case of a fluidized bed, as shown in figure 2.4 (b), the biomass is fluidized via carrier gas (N_2, H_2), and the char is removed via a cyclone separator. Scaling up is easier and commercialized in practice. Figure 2.4 (c) and (d) shows the rotating cone and ablative reactor. The former pyrolyzes the biomass by the heat transfer from the attrition created by hot sand in the rotating cone. The latter pyrolyzes the biomass at a contact point of the biomass with a rotating disk. The vacuum and auger reactor is shown in figure 2.4 (e) and (f). In the case of the vacuum reactor, the biomass is pyrolyzed in a large container under vacuum and low temperature. On the contrary, a screw conveyor is utilized to control the residence time of the biomass and char in the auger reactor.

The fixed bed reactor is utilized widely due to its easier screening of catalyst and reaction parameters (temperature, pressure, flow rate, catalyst loading, the effect of sweeping gas). However, up-scaling of the reactor is an issue due to clogging by char formation. In the case of the fluidized bed, the commercialization is more accessible due to better heat transfer by char/sand particle and easy removal of char by a cyclone separator. However, it requires high energy requirement for the gas blowers. In regards to better control over residence time of the volatile vapours, the vacuum reactor and auger reactor is superior to other reactors. However, vacuum reactor requires special inlets, outlets of biomass accompanied by low mass and heat transfer. Despite the simple operation of rotating cone and ablative reactor, high mechanical wear and biomass flexibility (fibrous biomass cannot be utilized) and the size of the blade are still questionable for commercialization. The simplicity of the reactor configuration is also owned by the auger reactor. The advantage and disadvantage include better tuning of the screw speed to control the heating rate, residence time, low energy requirement, no mechanical wear and sweeping gas, respectively [13].

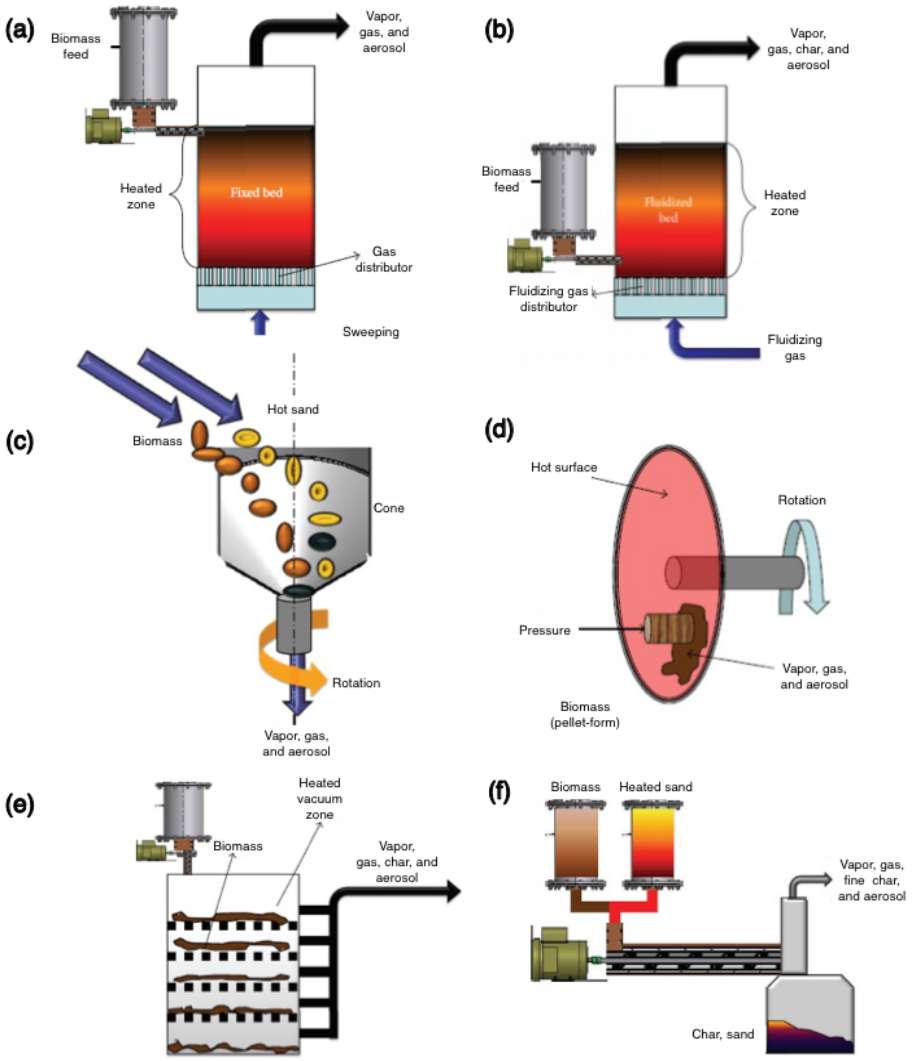

Figure 2.4: Pyrolysis reactors: (a) Fixed bed, (b) Fluidized bed, (c) Rotating cone reactor, (d) Abalative reactor, (e) Vacuum reactor, and (f) Auger/screw reactor [23]

An optimum reactor with better control over the flexibility of the pyrolysis reactor is widely preferred. In terms of bio-oil yield ($\geq$ 70 wt.%), the fixed bed, fluidized bed, rotating cone and ablative reactors are superior to other reactors, as shown in table A.1 (Appendix). Despite high flexibility of biomass particle size over rotating cone and ablative reactor, the operational flexibility and scale-up are the major downsides. Therefore, It becomes easier to foresee the factors behind the utilization of fluidized bed and fixed bed in fast pyrolysis. The combination of the fluidized bed and the fixed bed had been widely accepted, which will be discussed later in the section 2.7.

2.6 Hydropyrolysis

The biomass conversion via hydropyrolysis had emerged recently in the past decades. However, hydropyrolysis of coal for the production of aromatic compounds is dated back to the last century. Earlier studies conclude the encouragement of hydropyrolysis of coal over pyrolysis due to high recovery of volatile matter [30, 31]. It is worth mentioning that similar to pyrolysis, the relative fraction of liquid components from the biomass is still governed by the process condition (temperature, pressure, heating rate, particle size) in hydropyrolysis [32].

A comparative study on volatile fraction between non-catalytic fast pyrolysis of coal in N_2 and H_2 environment was reported by Metta Chareonpanich et al. [30]. In contrary to pyrolysis in a nitrogen atmosphere, the volatile fraction (condensable and non-condensable volatilized biomass vapours) increased with increase in temperature for hydropyrolysis. Figure 2.5 shows up to 58 wt.% of the volatile fraction at 900°C for hydropyrolysis, whereas a maximum of $\approx$ 40 wt.% is observed over the course of temperature increase in pyrolysis. This shows the enhanced devolatilization of coal in H_2 atmosphere by suppressing the intermediate reactive chemical components in the gas phase and thereby increasing the volatile fraction of hydropyrolysis bio-oil compared to pyrolysis [30].

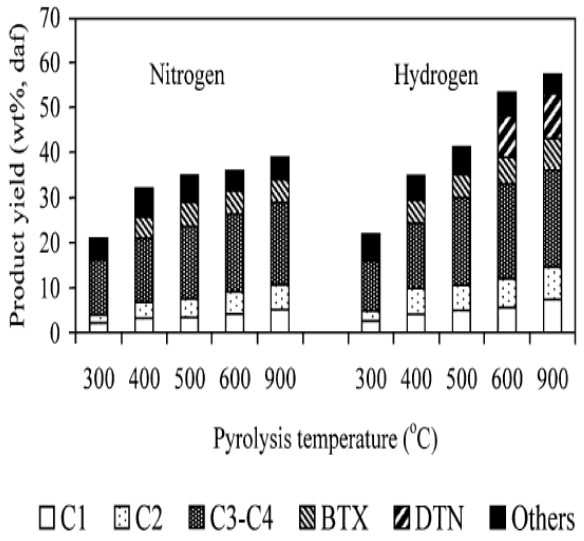

Figure 2.5: Effect of pyrolysis temperature on product yields at the heating rate of 15 ° C/s [30]

A profound similarity was correlated for the increase in volatile fraction for hydropyrolysis of coal with biomass. As previously mentioned, Steinberg et al. introduced the concept of hydropyrolysis of biomass. Figure 2.6 shows the list of the chemical reaction (catalytic and non-catalytic) prevailing under the hydropyrolysis condition. These include deoxygenation (oxygen removal via CO, CO_2 and H_2O), hydrogenation of unsaturated chemical bonds, hydrocracking, transalkylation etc.

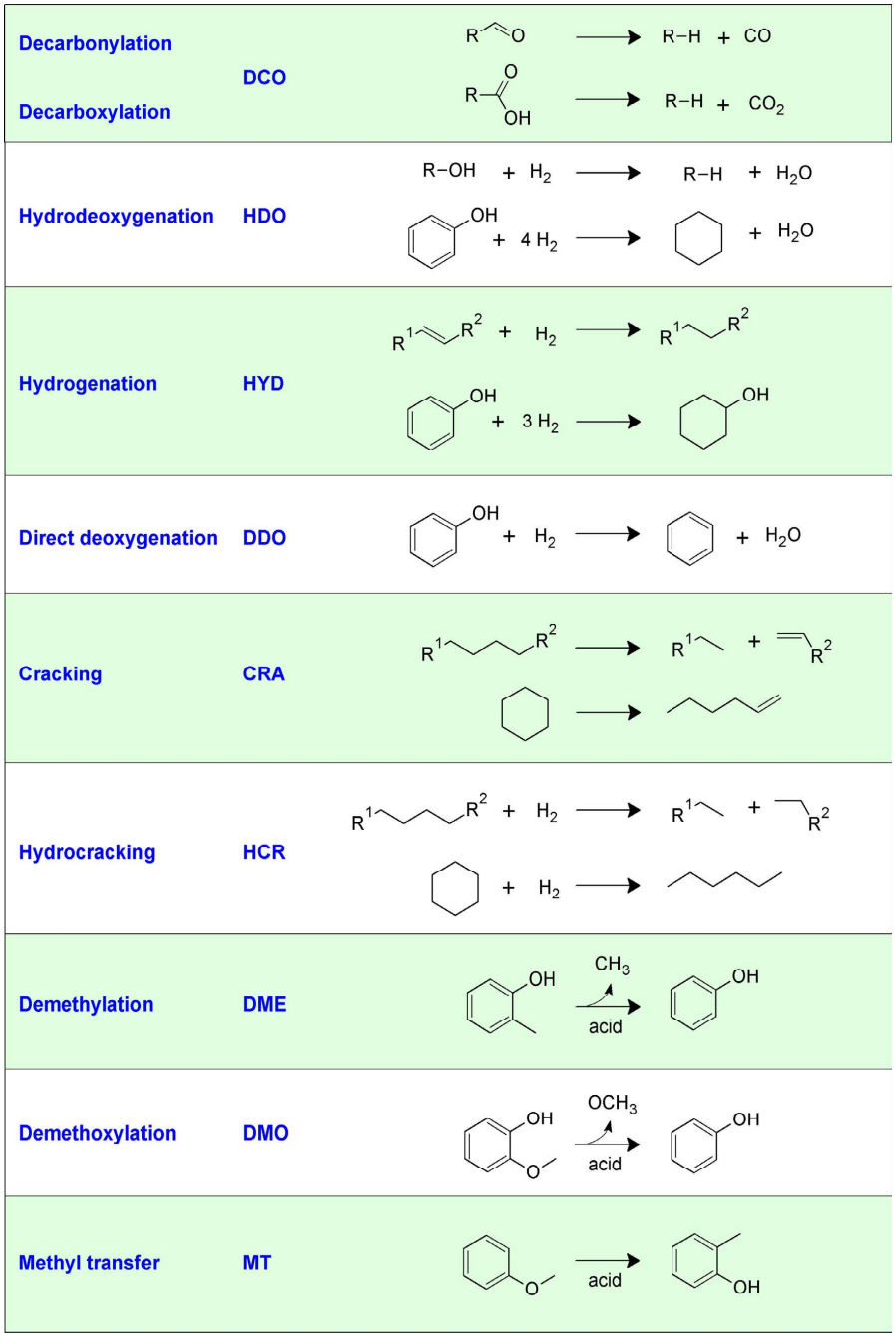

Figure 2.6: Reactions prevailing under hydropyrolysis. R denotes H, CH3, and aromatic/aliphatic groups present in bio-oil [33].

At this point, It is essential to understand the crucial role of hydrogen in the hydropyrolysis. Firstly, suppression of reactive poly-aromatics, olefins and other anhydrous-oligosaccharides by hydrogenation which otherwise undergoes polymerization in conventional non-catalytic pyrolysis of biomass [1, 25, 34]. Secondly, the severity of the cracking is increased in the presence of hydrogen. Thirdly, in-situ hydrotreating of heteroatoms such as oxygen. The carbon recovery is increased due to the removal of oxygen as H_2O instead of CO, CO_2 [6, 29]. The hydrodexygenation reaction is shown in figure 2.6. Fourthly, It is reported that oxygen removal in a hydrogen deficient atmosphere increases coke deposition [35]. However, reduced coke deposition over the catalyst is observed in the presence of hydrogen in hydropyrolysis [36, 37].

2.7 Hydropyrolysis setup configuration

The development of the hydropyrolysis reactor is one of the objectives of this project. Figure 2.7 shows a possible configuration reactor and catalyst placement. Figure 2.7 (a) and (b) shows a single-stage hydropyrolysis reactor with catalyst placed in-situ in the latter. In contrast, figure 2.7 (c) and (d) utilizes 2 stage upgrading configuration. The hydropyrolysis is carried in the 1^{st} stage, and catalytic up-gradation is accomplished in 2^{nd} reactor. The major difference exists in the catalytic/non-catalytic hydropyrolysis carried in the 1^{st} stage reactor. Based on the discussion presented on pyrolysis reactors in section 2.5, it is evident with regards to up-scaling that fluidized bed operates well with biomass flexibility and superior heat transfer compared to other reactors. However, ex-situ upgrading of biomass derived oxygenates over catalyst is still preferred over fixed bed due to simplicity and cost factors.

A brief overview of the existing pyrolysis reactor was discussed in section 2.5. Herein, the hydropyrolysis is easily accomplished by either replacing the sweep gas from N_2 to H_2 gas or co-flowing together with N_2. Similar to fast pyrolysis, hydropyrolysis can be operated in two modes based on the heating rate and residence time. The fast hydropyrolysis operates at a higher heating rate and short residence time, whereas slow pyrolysis operates at a lower heating rate and long residence time [13]. A major advantage of fast hydropyrolysis comes with 20 wt.% of less oxygen in bio-oil compared to slow hydropyrolysis. To the best of my knowledge, fast hydropyrolysis is extensively subjected to research and development from the past decade [13].

The quality of bio-oil shows significant improvement during two-stage hydropyrolysis configuration [38, 39]. This is evident due to customizable reaction temperature for both hydropyrolysis and ex-situ catalytic up-gradation independently. However, both versions of 2-stage hydropyrolysis had been successfully demonstrated [3, 40]. Herein, A short overview of the conceptual designs of hydropyrolysis technology, which is based on aforementioned reactor configuration will be discussed, and it is worth mentioning the IH^2 technology, which had progressed to the commercialization to a pilot plant [41].Further, the potential of H_2-Bio-oil technology will be discussed.

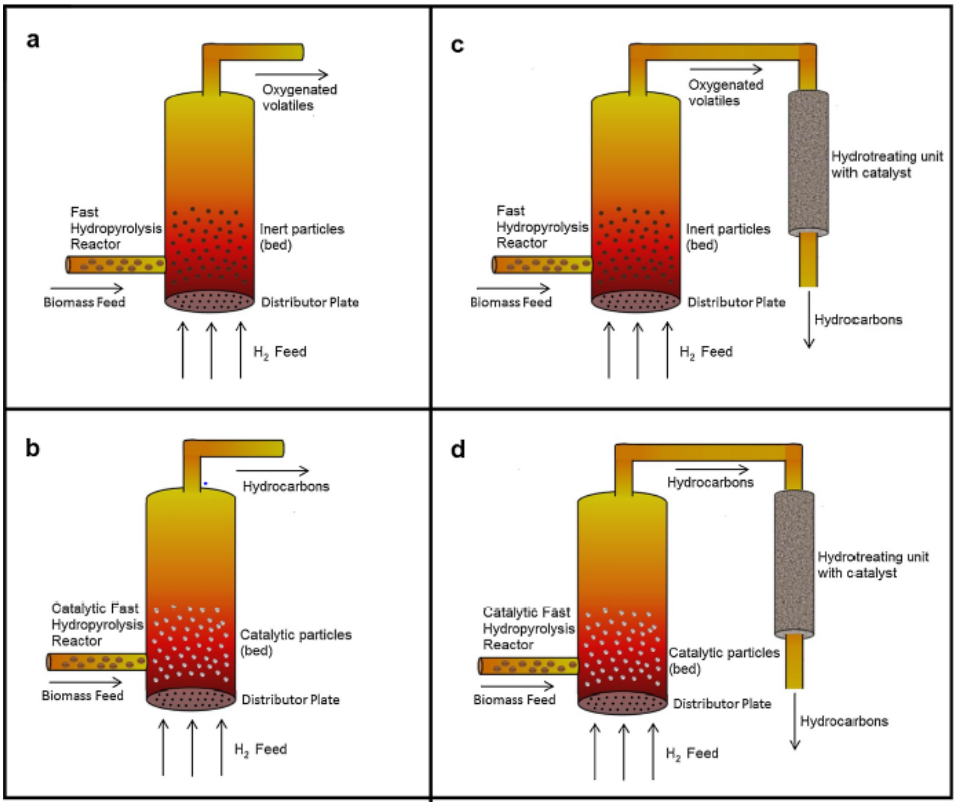

Figure 2.7: Available continuous fast hydropyrolysis system configurations: (a) Non-catalytic fast hydropyrolysis; (b) Catalytic fast hydropyrolysis; (c) Non-catalytic fast hydropyrolysis with ex-situ hydrotreating; (d) Catalytic fast hydropyrolysis with ex-situ hydrotreating [33].

2.7.1 IH^2 technology

IH^2 technology is abbreviated as Integrated Hydropyrolysis and Hydroconversion. This technology was developed by Gas Technology Institute (GTI). Herein, A hydrotreater unit is utilized after the catalytic hydropyrolysis unit. The catalyst composition is unavailable due to the patented process. Figure 2.8 shows the schematic sketch of IH^2 process flowsheet. The overall process is as follows: 1) The process parameter are as follows: Temperature: 350-480° C; Pressure: 14-35 bar: Heating rate: 100 °C/sec. It is worth noting that residence time is in minutes as opposed to seconds in conventional fast hydropyrolysis [40]. 2) The flue gas (C2-C3) is separated from the gasoline/diesel range hydrocarbons by the distillation unit placed after the hydrotreater. 3) The separated flue gas is sent to the steam reforming unit, thereby producing hydrogen in-situ. Internal hydrogen production eliminates the reliance on external hydrogen supply for hydropyrolysis. 4) The hydrogen production can be adjusted depending on the feedstock by varying the temperature. The higher temperature results in high C2-C3 fraction, thereby increasing the input to the steam reformer. 5) Oxygen level $<$10 wt.% is attained in 1^{st} stage catalytic hydropyroly-

sis, however, hydrotreating unit is utilized to furnish the product distribution based on the requirement. These characteristics of the IH^2 technology has led to a demonstration of 50 kg/day pilot plant in Bangalore, India [42].

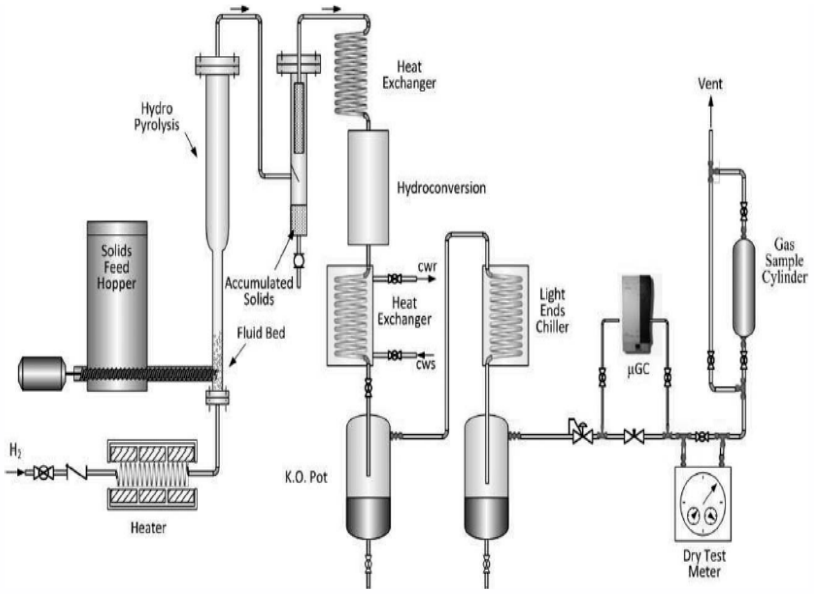

Figure 2.8: Process flowsheet of IH^2 technology [40].

2.7.2 H_2-Bio-oil technology

The researchers developed the H_2-bio-oil process at Purdue University. At first, the biomass is volatilized by non-catalytic fast hydropyrolysis. Consecutively, the gas vapours are sent to the catalytic fixed bed reactor after removal of char. There are two significant variations compared to the IH^2 technology. Firstly, no catalyst is utilized in the 1^{st} stage hydropyrolysis. This can be attributed towards: 1) Avoiding additional deactivation of the catalyst by coke formation which otherwise deactivates by char deposition, 2) No energy consumption for catalyst regeneration in 1^{st} hydropyrolysis reactor. Secondly, the external supply of hydrogen is needed for operation [3].

The researchers at the Purdue university had also proposed variation to the H_2-bio-oil technology. The main objective was to reduce/eliminate the consumption of external hydrogen supply. These include H_2-bio-oil-C, H_2-bio-oil-NG, H_2-bio-oil-B process, as shown in figure 2.9. H_2-bio-oil-C is based on the combination of Integrated Gasification Combined Cycle (IGCC) plant with H_2-Bio-oil process.

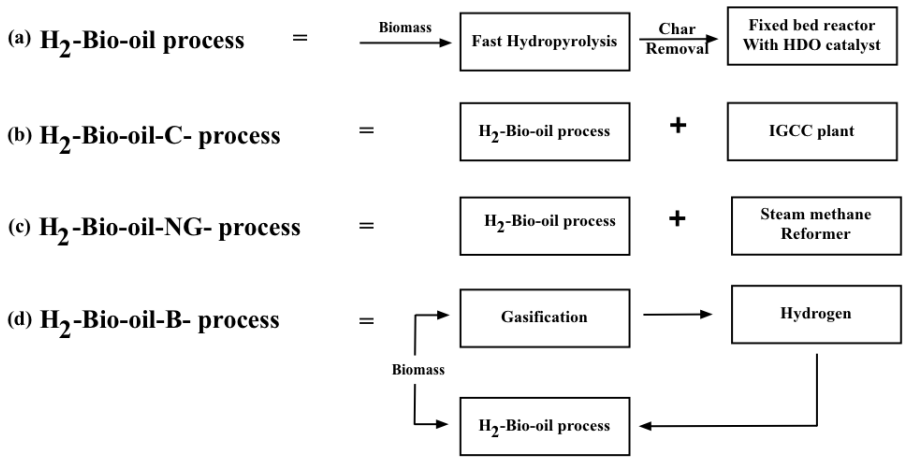

Figure 2.9: Process configuration for H_2Bio-oil process [3]

The main advantage of the process is the in-situ supply of hydrogen from the coal gasifier and heat for hydropyrolysis is supplied by hot syngas. The char and flue gas from hydropyrolysis can be utilized in coal gasifier and gas turbine respectively. The H_2-bio-oil-NG process is similar to H_2-Bio-oil-C concept except for Steam Reformer (SMR) switching the coal gasifier in IGCC. Similar to IH^2, hydrogen is generated in-situ in SMR. In regards to H_2-bio-oil-B process, a small portion of biomass is gasified to produce H_2 required for the operation [3].

2.7.3 Biomass loading-reactor-condenser design utilized in hydropyrolysis experiment

Countless literature is available on hydropyrolysis on model compounds. Limited studies are conducted with real biomass. A summary on the typical loading of real biomass and type of condenser utilized to cool the volatile fraction is shown in figure 2.10. The most contrast variation in the hydropyrolysis in fixed bed is in the introduction of biomass. Biomass is loaded during catalyst loading or introduced after the desired reaction temperature in the heating oven/furnace (mimicking continuous feeding of biomass in large scale pyrolysis reactor into a semi-batch manner) is reached. The former biomass loading is majorly adopted in the literature, whereas the latter is scarcely utilized. Typical loading of 4 to 80 g of biomass is reported in the literature for hydropyrolysis in fixed bed reactor [38, 43, 44, 45, 46, 47, 48, 49].

The type of condenser is also a crucial factor to quench the volatile fraction. The rate of condensation and residence time are important factors. Unfortunately, limited information is available on the design parameters of the condenser. The majority of the condenser are based on shell and tube heat exchanger and modified/unmodified Graham condenser immersed in dry ice, water ice with/without salt.

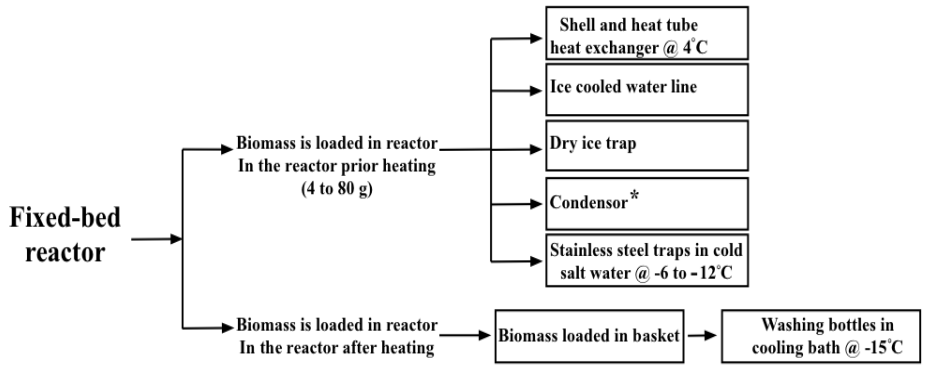

Figure 2.10: Typical real biomass loading and type of condenser in fixed bed hydropyrolysis [38, 43, 44, 45, 46, 47, 48, 49]. *Condenser= No available information [46, 47]

2.8 Characterization of bio-oil

The bio-oil is an diverse mixture of oxygenated compounds comprising of carboxylic acids, aldehydes, ketones phenols, esters, ethers, furans, water and so on [7]. This complex mixtures arises due to number of factors, Firstly, due to the variation in the cellulose, hemicellulose and lignin composition between various biomass sources with geographical location, as previously mentioned in section 2.1 [7]. Other factors include biomass pretreatment such as particle size reduction, experimental setup and condition for pyrolysis (temperature, pressure, heating rate, residence time, condensation method, rate of condensation), biomass moisture and ash content [7]. With regards to identification of bio-oil components, about 20% of water is present, Chromatography methods are able to detect around 55% ($\approx$ 40% and 15% detected by gas chromatography and liquid chromatography (non volatile components) respectively) whereas high molecular chemical compounds are not detectable [7]. Due to this varying components of bio-oil in boiling point, concentration, polarity and molecular weights, the complete chemical characterization remains a challenge [7]. This section will provide a short overview on the commonly reported chemical characterization technique for the bio-oil in the literature.

Gas Chromatography (GC) coupled with Mass Spectrometer (MS) and Flame Ionization Detector (FID) are widely used in the chemical characterization of bio-oil due to its wide availability, easy usage and acceptable prices. Despite these advantages, conventional gas chromatography technique faces issues with poor peak elution, unable to characterize long chain lignin polymers, limitation upto 300-400°C GC column temperature (varies between different columns), unavailability of mass spectra of certain chemical components of bio-oil in MS libraries and pure analyte standards for external standard calibration. It had been reported that over 300 chemical compounds present in bio-oil had been characterized by GC-MS and GC-FID. These limitation can be overcome and the percentage detection of chemical components in the bio-oil can be increased by utilizing two GC columns in series with different polarity and utilizing sample preparation techniques prior injecting the sample into the GC columns [7].

Two dimensional gas chromatography consist of two GC columns connected in series with combination of either non-polar and medium polar or non-polar and polar. The initial separation is based on the boiling points of the compounds in the non-polar column whereas polar/medium polar column utilizes the different polarity for separation. Herein, the modulator after the non-polar column does the injection of chemical compounds in the polar/medium polar column. This allows higher detection level of chemical components present in the bio-oil [7]. Other Characterization technique includes High Pressure Liquid Chromatography (HPLC), High Resolution Mass Spectroscopy (HRMS), Nuclear Magnetic Resonance (NMR), Fourier Transform Infrared Spectroscopy (FTIR).

Sample pre-treatment prior GC analysis had also proven to improve the characterization of bio-oil [7]. The pre-treatment can be categorized into solvent and solvent free categories. The former includes adsorption chromatography, solvent extraction such as Liquid-Liquid Extraction (LLE) and Supercritical Extraction (SFE), Gel Permeation Chromatography (GPC) and Solid Phase Extraction (SPE) [7]. The latter include Solid Phase Micro Extraction (SPME) and molecular distillation.

2.9 Catalytic up-gradation strategies

The discussion presented in section 2.4 concluded the inability of the bio-oil as a drop-in fuel in the transportation sector. Currently, there are two strategies available for the up-gradation of biomass pyrolysis products for the removal of detrimental oxygenate compounds. Firstly, upgrading the pyrolysis vapours after condensation via a hydrotreater unit. Secondly, high-pressure pyrolysis followed by high-pressure hydrotreating unit [50]. However, the former strategy is inefficient due to poor re-evaporation of the bio-oil, and including other factors, as mentioned in section 2.4. Despite the high-quality bio-oil produced from the latter strategy, hydropyrolysis at atmospheric pressure had gained recent attention due to the relatively low consumption of external hydrogen needed for hydropyrolyis experiment. In any case, both the strategies had been able to remove oxygen (via H_2O) on the expense of small oxygenates (C1-C6) leaving as gaseous products [50]. It had been approximated that lost carbon is 15–25 wt % of the input biomass [50]. This carbon loss has a significant impact on the final liquid yield and cost of bio-oil. In response, the attractive strategy for up-grading the bio-oil and reduce carbon losses is the conversion of lower molecular to high molecular weight oxygenates followed by hydrodeoxygenation seems a viable route for the production of gasoline/diesel/jet-fuel range hydrocarbon. Additional hydrodeoxygenation, aldol condensation, hydrogenation of ketone, and dimerization chemical reaction can produce speciality chemicals from biomass derived oxygenates, as shown in the figure.2.11 [50, 51].

The Carbon-Carbon (C-C) coupling reactions can be used to convert biomass-derived oxygenates into fuel range oxygenates. This is comprised of two chemical reactions, known as ketonization and aldol condensation. Recently, ketonization had captured renewed interest due to the presence of carboxylic functional group compounds (acetic acid, valeric acid levulinic acid and so on) present in the product stream of thermochemical conversion of biomass [51, 52, 53]. Additional benefits of ketonization include, increase in

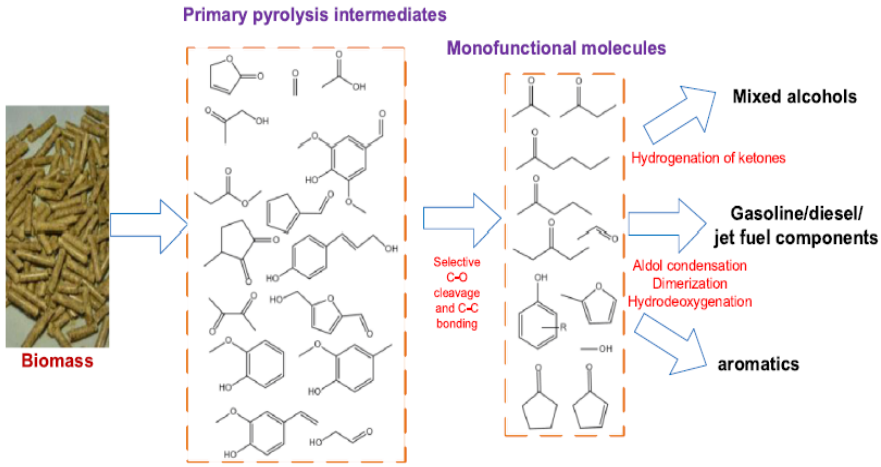

Figure 2.11: Conversion of biomass derived oxygenated to fuels and chemicals [9]

the energy density, molecular stability, and decrease in the acidity and oxygen content of the bio-oil [54, 55]. The Ketonization had also piqued the interest due to the production of speciality chemicals such as methyl nonyl ketone, cyclohexanone, methyl isopropyl ketone and methyl cyclopropyl ketone in the industrial and agricultural sector [56, 57] .

2.9.1 Ketonization

Ketonization is a reaction between two carboxylic acids to yield higher order ketone molecule alongside CO_2 and H_2O molecule. Two different routes of ketonization can take place. One is self ketonization (also known as homo-ketonization) of the same molecule (RCOOH or R$^{'}$COOH) and second is cross-ketonization in which two different carboxylic acids (RCOOH and R$^{'}$COOH) react to yield a ketone molecule. These long-chain oxygenates can be upgraded to gasoline/diesel/jet fuel range hydrocarbons by subsequent aldol condensation and HDO which will be discussed later in the section 2.9.2 and 2.9.3 [53]. Overall, the reaction scheme for ketonization between the two different carboxylic acid molecule shown in figure 2.12, which can yield three different ketones from self and cross ketonization [51]. Further, literature also support carboxylic acids compounds to be the most reactive functional group in ketonization reaction compared to other functional groups [58].

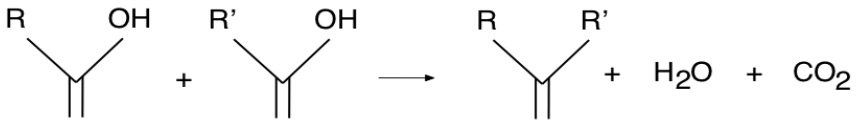

Figure 2.12: Ketonization reaction

Ketonization reaction in heterogeneous catalysis had been exploited over the amphoteric (contains both acidic and basic properties), pure acidic and basic catalyst, hetropoly acid in aqueous or gas phase [51, 52]. There are two pathways for ketonization reaction, namely bulk ketonization and surface ketonization which had been accepted in the literature [52]. The former is based on the thermal decomposition of the bulk carboxylate salt formed by the exposure of carboxylic acids to the catalyst [59], whereas the latter occurs only on the catalytic surface (no bulk crystal reconstruction) [52]. A typical ketonization reaction occurs between 200-500°C, however, the dominant mechanistic pathway depends on the temperature and the type of metal oxide [51, 52, 60, 61]. For example, MgO and CeO_2 can catalyze both surface and bulk ketonization depending on the experimental condition [62, 63, 64]. However, the strength of metal-oxygen bond is of prime importance in both the case [60]. The bulk ketonization is carried out by low lattice energy catalyst such as MgO, CaO, BaO, SrO, and CdO whereas surface ketonization is catalyzed by high lattice energy catalyst such as TiO_2, CeO_2, ZrO_2, SnO_2 and so on [52]. Until now, the pathway for both the mechanism is heavily subjected to debate. Pacchioni et al. and Kumar et al. had collectively summarized various debated mechanisms on ketonization [63, 65].An overview on the debated mechanism is discussed in section 2.10.1. Other reported catalyst for ketonization include mixed oxides of Cu, Co and Ni, potassium carbonate promoted Cr–Znc–Mn catalyst, Sr-$La_0 \cdot 7\,Sr_0 \cdot 3\,MnO_3$, rare earth metal oxides (including La_2O_3, Pr_6O_{11}, Nd_2O_3, Sm_2O_3, Eu_2O_3, Gd_2O_3, Tb_4O_7, Dy_2O_3, Ho_2O_3, Er_2O_3, Tm_2O_3, Yb_2O_3, and Lu_2O_3) and layered double hydroxides of Zn/Al, Mg/Al etc. [9, 62, 63, 66].

The hydropyrolysis at ambient pressure is attractive to obtain an optimal balance between the cost of external hydrogen supply and the bio-oil quality, as discussed in section 2.7. Table 2.5, 2.6, 2.7, 2.8, 2.9 and 2.10 collectively summarizes the important discussion reported in the last ten years on ketonization studies on model compounds and real biomass/bio-oil for direct vapour phase up-gradation of biomass-derived/model compounds representing bio-oil at atmospheric pressure. Majority of the ketonization experiment on model compounds had been conducted in a quartz fixed-bed microreactor, whereas the real biomass as feedstock was conducted in the tubular fixed-bed reactor. The discussion below is exclusively dedicated towards the conversion of biomass-derived oxygenates via ketonization. Therefore, other ketonization studies on fermentation residue as feedstock, speciality chemical production (methyl nonyl ketone, methyl isopropyl ketone, methyl cyclopropyl ketone, cyclohexanone), aqueous phase ketonization is not included in this scope of review. Similar to two stage reactor configuration in figure 2.7 (c) and (d), It is more effective to upgrade via ketonization of biomass-derived vapour in ex-situ configuration after the hydropyrolysis unit instead of re-evaporation of thermally unstable bio-oil compounds after condensation of pyrolysis products [67].

Acetic acid constitutes the major fraction of carboxylic acid in the bio-oil [54, 68]. Therefore, acetic acid and with other similar model chemical compounds are a common choice for screening the catalyst based on activity, selectivity and stability, as observed from the table 2.5, 2.6, 2.7, 2.8 and 2.9. the catalyst deactivation remains one of the serious concern over the commercialization of the ketonization catalyst. Therefore, the prime motivation behind utilization of an individual fraction of bio-oil aids is to get a better understanding over synergism between different mixed mixtures of metal oxide, metal

doping, experimental condition (effect of temperature, gas atmosphere, pressure) and the reaction mechanism for developing an optimal catalyst for ketonization.

It is worth mentioning about the participants of ketonization reaction, the carboxylic acid is not the sole participants, aldehydes and esters also participate in ketonization [51]. Esters are reported to undergo ketonization in the presence of CeO_2, MnO_2, and ZrO_2 at 350–400°C [51]. The water produced from the ketonization of the carboxylic acid is prone to hydrolyze the esters to yield additional alcohol and carboxylic acids. The secondary alcohols are present in higher amounts than primary alcohols in bio-oil. Despite the less reactivity, a detectable amount of esters are still formed [51].

Earlier studies tested metal oxides from group 1-4 in the periodic table for ketonization reaction [57]. Table 2.4 shows the comparison of the catalytic activity in ketonization of the acetic acid molecule at 200 and 300°C. It is evident from the results that amphoteric reducible oxides (CeO_2, MnO_2, La_2O_3) function superior to its counterpart pure acidic and basic oxide catalyst [61, 65]. Additionally, It is well established from the literature that, high ketonization activity had been observed for pure reducible metal oxide catalyst such as TiO_2, ZrO_2 and CeO_2 due to their acid-base properties on the surface [52, 54, 61, 69]. Further, the amphoteric metal oxide is reported to promote ketonization at reduced temperature (300°C) compared to bulk ketonization occurring at 400°C [10]. TiO_2 is reported to catalyze both ketonization and deoxygenation [70]. Another study reports the superiority of MnO_2 and CeO_2 among 20 other metal oxides supported over Al_2O_3, SiO_2, TiO_2 [71]. Further, doping with hydrogenating metal function over the metal oxide and pre-reduction before ketonization experiment had improved catalyst activity by increasing the oxygen vacancy over the surface of the catalyst (oxophilic nature) [52, 54, 61, 69].

Catalyst	Acetone yield (573 K)	Acetone yield (673 K)	Catalyst	Acetone yield (573 K)	Acetone yield (673 K)
SiO_2	2	5	ZnO	6	33
B_2O_3	2	3	MnO	6	33
MoO_3	2	5	PbO	6	76
WO_3	2	5	Cr_2O_3	1	39
P_2O_5	1	12	Fe_2O_3	13	59
V_2O_5	3	21	CoO	13	63
Bi_2O_3	10	18	MgO	7	59
NiO	7	-	Nd_2O_3	3	61
Al_2O_3	0	37	La_2O_3	3	87
CuO	5	39	MnO_2	18	96
CdO	6	94	CeO_2	9	97

Table 2.4: Activity of Various Oxides (10 wt.% MO_x/SiO_2) in catalytic conversion of acetic acid to acetone [65]

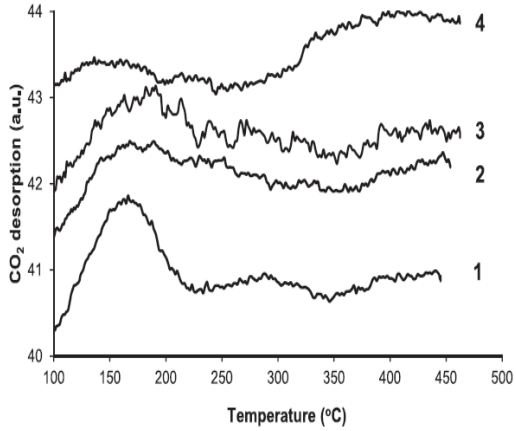

H

Figure 2.13: CO_2 TPD over: 1) CeO_2, (2) ZrO_2, TiO_2, and (4) α-Al_2O_3 [61]

Different support materials had been utilized to support the metal oxide/mixed metal oxide to improve the ketonization activity. The widely used supports are alumina, silica and carbon. Among them, alumina (high surface area) is not only utilized for dispersion of low surface area metal oxides [54, 72], It also serves in two other ways: 1) Provides additional lewis acid sites which aid in adsorption of carboxylic acid on the catalytic surface, and 2) Formation of metal aluminates (example zinc aluminates, calcium aluminates) which is stable at a calcination temperature of 800°C [54]. Glinski et al. recently reviewed 26 metal oxides (Ag, Bi, Cd, Cu, In, Pb, Re, Cr, Mg, Zn, Ca, Ga, Sr, Ba, Al, Eu, Gd, V, Co, Fe, La, Mn, Zr, Ce, Th and U) supported over SiO_2, Al_2O_3, TiO_2 for the ketonization of propanoic acid at 350-450°C. It was reported that Al_2O_3 outperformed TiO_2 and SiO_2 as support material for the active metal oxides [73]. Other studies also include comparison of ketonization activity of alumina with TiO_2, CeO_2, ZrO_2. It was observed that alumina was least active among the catalyst due to its relatively weak number of basic sites, as shown in figure 2.13 [61]. With regards to ketonization over neutral support such as silica, the base modification over silica showed 92% selectivity for pentanone with 84% conversion of propanoic acid at 500°C [74]. The base modification strategy over different catalyst could be a useful pathway to explore its influence on ketonization.

The reducible metal oxide by nature acts as a support material. The enhancement of catalytic activity by doping transition metals is of common practice in catalysis. This had also been extended to ketonization catalyst. Rozmysłowicz el al. reported the usage of copper as dopant over ZrO_2. It was claimed to increase the oxygen vacancy and aid in desorption of oxygenated compounds over the catalyst [75]. Recently, Baylon et al. reported the mechanistic insights on doping the Zn over ZrO_2 in conversion of acetone and methyl ethyl ketone [76]. Ruthenium had been reported to be active both in the presence of water and oxygenated compounds during the upgradation of biomass vapours [70]. In this regard, reducible TiO_2 support had shown to stabilize the Ru species at high temperature both during testing of real biomass vapours and model based compounds from lignin

[70]. The enhancement via doping is not only limited to metal oxide catalyst, the zeolite had also been incorporated with basic metals such as Mg to promote ketonization [77]. Recently, Ma et al. showed that doping Ni over ZSM-5/MCM-41 had improved the ketonization activity [78]. In contrast, Glinski et al. reported that doping with alkali metal over amphoteric oxide will reduce the activity of the catalyst due to neutralization of the acidic sites over the catalyst [73]. Another study by Mansur et al. revealed that alkali and alkaline earth metals such as K and Mg present in bio oil decreased the ketonization activity of the ZrO_2-CeO_2 mixed oxide catalyst [79].

The ketonization reaction is observed to be sensitive to temperature, pressure, carrier gas (H_2, N_2, He), catalyst particle size apart from nature of metal oxide and synergy with various transition/noble metals. Mansur et al. reported the change in crystallinity of the ZrO_2 catalyst led to a decrease in the activity of the catalyst [79]. A similar observation was reported by Lu et al. [80]. In regards to carrier gas, utilizing H_2 as carrier gas increases the ketonization activity of the catalyst. Taimoor et al. showed the increase in activity of α-Fe_2O_3 during the co-flow of hydrogen gas with nitrogen gas flow. This is attributed to the regeneration of the catalyst by creating more oxygen vacancies over the catalyst surface [81]. Therefore, the conversion and selectivity data in table 2.5, 2.6, 2.7, 2.8 and 2.9 should be taken with caution due to the different carrier (mixed/unmixed) gas utilized in the experiments. Finally, the structure sensitive nature of the catalyst was reported by Bennett et al. for the catalyst Fe_3O_4/SiO_2 [82]. The effect of pressure does have a significant positive influence on the catalytic performance of the catalyst. The activity of the catalyst is observed to increase with increase with the partial pressure of hydrogen in the carrier gas. This is due to the abundant availability of hydrogen molecules on the catalytic surface. Additionally, deactivation of the catalyst is observed to slow down. However, the effect of pressure on catalytic activity is not included in this scope of review.

On one hand, the mechanistic elucidation of ketonization using model compounds had been successful in screening the catalyst. On the other hand, the corresponding successful catalyst on model compounds fail to show promising results in real biomass derived feed [83]. Therefore, the observation derived from the model compound on ketonization should be taken again with caution (table 2.5, 2.6, 2.7, 2.8 and 2.9). Table 2.10 reports few ketonization studies on real biomass/bio-oil. The complexity in utilizing ketonization catalyst and observations from model compounds was showed by Liu et al. by introducing the ketonization by-product (CO_2 and H_2O) with acetic acid in the feed. Herein, the author compared the activity among ZrO_2-CeO_2, Mn_2O_3-CeO_2 and CeO_2 at 450 °C. It was proven that the ranking based on the catalytic activity changed during temperature variation and co-feeding/no co-feeding of CO_2 and H_2O with acetic acid [84]. Similarly, it was proven that presence of fufural in the feed was an inhibiting to ketonization [85]. Further, it was shown that furfural, cresol had similar characteristics of reversible deactivation over ZrO_2-CeO_2 mixed oxide whereas phenol did not show any interaction [85]. The ketonization by-product CO_2 and H_2O also had an inhibiting effect on the catalyst [62, 86]. Additionally, primary ketonization product (acetone) was also studied to understand its influential effect on the catalyst Ru/TiO_2 [87]. The ketonization activity decreased upon introduction to acetone, H_2O, CO_2 with acetic acid . The inhibitory effect was ranked in the order of acetone>CO_2>H_2O. Overall, it can be concluded that, either the ketonization

product or the individual components of the biomass feed has an inevitable interaction with the catalytic active centers (Lewis acid and Brønsted basic sites) for ketonization reaction owing to its deactivation. However, different catalyst combination and their corresponding synergism has its own resistant to different components in the feed. For example, Liu et al. observed different trends on ketonization activity (CeO_2, CeO_2-ZrO_2 and CeO_2-Mn_2O_3) upon introduction CO_2+H_2O/CO_2, H_2O with acetic acid [84].

Literature's over ketonization is not only limited to small scale quartz or fixed bed reactor. For example, Kalogiannis et al. studied the MgO catalyst in pilot scale fluidized bed and studied the ketonization activity and stability. Further, it was documented that severe deactivation of the catalyst was observed due to the sintering and decreased porosity [88]. Similarly, observation were reported by Stefanidis et al. [89]. However, MgO regeneration were quite simple by burning of the coke at elevated temperatures.

It is worth to mention studies on utilization of spent catalytic converters as a ketonization catalyst. However, the catalytic activity was attributed to the presence of CeO_2, ZrO_2, MgO with other metals present in the car catalytic converters [90]. This seems an alternative option for utilizing pure metal oxide. Other studies include selective removal of acetic acid present in biomass without any interaction with pyrolysis components. $CaCO_3$ was reported to be superior over ZrO_2, $MgCO_3$, CaO, $Ce_2(CO_3)_3$, CeO_2, TiO_2, MgO [67]. Lately, the ketonization is not been limited to lignocellulosic biomass. For example, ZrO_2, MgO, TiO_2 had been experimented over algal biomass and ketonization activity were successfully proven at its experimental condition [91].

S.No.	Model compound	Reaction temperature	Catalyst	Conversion & selectivity (%)	Comments
1[54][a]	Acetic acid	375-425°C	Ca/Zn/AlO_x (3:3:1)	Conversion = 93-100; Acetone selectivity = 97-100	1)No influence of phenol over catalytic activity and selectivity. 2)Furfural addition decreased catalytic acitivity/selectivity.
2[92][b]	Propionic acid	300-375°C	polymorphic ZrO_2	Conversion = 100; 3-Pentanone selectivity $\geq$ 97.5	1) Importance of lewis acidity is emphasized during the comparison of high activity of tetragonal ZrO_2 compared to monoclinic ZrO_2 structure.
3[93][a]	Acetic, propionic, and n-butyric	350°C	HZSM-5	Conversion = 100; Aromatic selectivity = 50-70	1)Aromatics had an increasing trend with carbon chain length. 2)Higher chain length increases coke deposition on catalyst.
4[94][c]	Acetic acid	500°C	MgO	Conversion = 73; acetone selectivity = 23	1)Catalytic activity and coke production was lower and higher for MgO compared to ZSM-5.
5[95][b]	Propionic acid and furfural	350°C	0.1 wt.%-Pd/Red	Conversion = 100; n-heptane, 3-ethyloctane selectivity = 58, 42	1)n-heptane and 3-ethyloctane was proportional to nobel metal loading. 2)Doping with pottasium reduced coke and methanation reaction and increased the oxidation stability of nobel metals.

a: Quartz fixed-bed microreactor; b: Fixed-bed tubular reactor; c: Fluidized bed reactor

Table 2.5: Atmospheric ketonization of model compounds-I

S.No.	Model compound	Reaction temperature	Catalyst	Conversion & selectivity (%)	Comments
6 [96][a]	Acetic acid	400°C	10 wt.%-Ga-HZSM-5	Conversion = 29; Acetone selectivity = 23	1) Turnover frequency of catalyst was proportional to Gallium loading. 2) Lewis acid sites as active centers for ketonization was emphasized.
7[62][b]	Propionic acid	350°C	$Mg_3Al_{0.9}Ce_{0.1}$	Conversion = 90; Pentanone selectivity = 100	1) Simultaneous bulk and surface ketonization at low temperature and surface ketonization observed at 350°C, respectively. 2) Effect of Ceria doping was studied over catalytic performance.
8[83][a]	Acetic acid, formic acid, acetol, levoglucosan	400°C	Reduced Red Mud (RRM-300)	Conversion= 0.4, 1, 0.9, 1; Acetone, 2-Butanone, cyclic ketones selectivity = 7, 1.5, 1	1)Magnetite was active center for acetic acid conversion. 2)Alkali metal addition reduced & improved coke and ketonization activity, respectively. 3) Reduced iron state (Fe^0) in the catalyst lead to coke formation (reduced selectivity to ketones).
9[82][c]	Acetic acid	400°C	Fe_3O_4/SiO_2	Conversion = 10-35; Acetone selectivity = 60	1) Conversion and selectivity was observed to be structure sensitive.

a: Tubular fixed-bed; b: Quartz fixed-bed; c: Py-GC/MS

Table 2.6: Atmospheric ketonization of model compounds-II

S.No.	Model compound	Reaction temperature	Catalyst	Conversion & selectivity (%)	Comments
10[66][a]	Acetic acid	350°C	$La_{1-x}Sr_xMnO_3$	TPR studies	1)The decrease in total conversion was proportional to Sr loading. 2)High thermal stability and electron conductivity of catalyst was emphasized.
11[97][a]	Acetic acid	350°C	$Ce_{0.8}Fe_{0.2}O_{2-x}$	Conversion= 99.5%; Acetone selectivity= 99.7	1)Doping of Fe over CeO_2 increased conversion by introducing medium basic strength besides weak basic sites present in CeO_2. 2)Temperature dependence of Ce valence state was emphasized.
12[80][a]	Acetic, propanoic acid	450°C	Ca-Mo_2C	Conversion= 100,70 Acetone, 3-Pentanone selectivity= 97,50	1)The catalytic conversion appeared to be temperature sensitive in carbide based catalyst.
13[98][a]	Acetic acid	380°C	20 wt.%-Co-Mo/Al_2O_3	Conversion: 96 ; Acetone conversion: 95	1)Catalytic selectivity decreased with increase in temperature above 380°C due to coke formation.
14[68][b]	Acetic, propanoic acid	335°C	Fe_2O_3[c]	Conversion = 90, 95 ; Acetone, Pentanone selectivity: 65, 70	1)Similar catalytic activity observed over both model compounds.

a: Quartz fixed-bed; b: Tubular fixed bed; c: Catalyst prepared by nanocasting method;

Table 2.7: Atmospheric ketonization of model compounds-III

S.No.	Model compound	Reaction temperature	Catalyst	Conversion & selectivity(%)	Comments
15[86][a]	Acetic acid	350°C	Ti-$Ce_{0.7}Ti_{0.3}O_2$	Conversion = 100; Acetone selectivity = 98	1)The incorporation of Ti^{4+} into the CeO_2 lattice modified the acid-base properties compared to pure CeO_2 and TiO_2. 2)The catalytic activity decreased with over-doping of Ti.
16[72][b]	Proponoic acid	380°C	20wt.%-Zn-Cr(10:1)/Al_2O_3	Conversion = 99; pentanone Selectivity = 97	1)Alumina was active and hign dispersion of mixed oxide increased the ketonization activity.
17[99][b]	Acetic acid	400°C	$Fe_{0.2}Ce_{0.2}Al_{0.6}O_x$	*	1)Co-feeding high level of phenolics reduced the activity. However, certain degree of activity was regained by increasing the temperature upto 430°C.

a: Quartz fixed-bed; b: Tubular fixed-bed;
*: Many conversion and selectivity exist due to different mixtures of acetic acid with phenolics prepared.

Table 2.8: Atmospheric ketonization of model compounds-IV

S.No.	Feedstock	Reaction temperature	Catalyst	Comments
1[55][a]	Bambusa balcooa	380°C	0.5 wt.% NiO[a] & 5 wt.% CaO[a] w.r.t feedstock	1)Acid content reduced from 18.07 to 6.31%. 2)High Ketone content and reduced anhydrosugar content (deoxygenated to furans) compared to non catalytic product distribution. 3)The viscosity of bio-oil decreased and increased with CaO and NiO loading, respectively relative to non-catalytic bio-oil.
2[100][b]	Wheat straw	550 and 450°C in reactor-1 and 2, respectively.	ZrO_2/H-ZSM-5-ATP* + K-grafted USY zeolite	1)Decreased carboxylic acid with increase in ketones and aldehydes was concluded utilizing cascade configuration of two reactors (ex-situ catalytic up-gradation).
3[101][c]	bio-oil**	400–500°C	Dolomite	1)Complete removal of acids. 2)CO_2 capture was emphasized. 3)Levoglucosan and phenol content decreased. 4)High acetone, 2-butanone and cyclopentanones content compared to raw bio-oil. 5)Deactivation due to coke formation and carbonation of $CaO/Ca(OH)_2$.

* : Catalyst is shaped into sphere using attapulgite; **: Bio oil obtained from flash pyrolysis of pine sawdust.
a : Custom build reactor; b : 2-Fixed-bed reactor; c : Stainless steel U-tube reactor;

Table 2.9: Atmospheric ketonization of real biomass-I

S.No.	Feedstock	Reaction temperature	Catalyst	Comments
4[68][a]	Aq. phase bio-oil *	335°C	MnO_2-HT*	1)Catalytic conversion was 83%.
5[79][a]	Bio oil**	350°C	ZrO_2–FeO_X	1)The decomposition of light and heavy oxygenates in bio oil over the catalyst yielded additional carboxylic acid and ketone. Therefore, final ketones content increased in the product stream. 2)Overloading Zr/Fe ratio increased the coke formation over the catalyst.
6[64][b]	Bamboo Sawdust	600°C	ZrO_2CeO_2/γ-Al_2O_3	1) The catalyst produced the highest ketone, phenol, alkyphenol, monoaromatics (xylene, toulene), monofunctional furans and least heavy phenolic content compared to non-catalytic experiment. 2) Utilizing ZSM-5 in mixing/cascade mode yielded higher monoaromatics.

* : 71.3 wt.% water, 8.2 wt.% Acetic acid; ** : Hydrothermal synthesis method;
** : Bio-oil obtained from fast pyrolysis of Japanese cedar woodchips.
a : Fixed bed reactor; b: Py-GC/MS

Table 2.10: Atmospheric ketonization of real biomass-II

2.9.2 Aldol condensation

The second C-C coupling reaction is aldol condensation. The importance of carboxylic acid groups is beneficial since reactants for aldol condensation can be also supplied continuously by the products of ketonization. Therefore, the high fraction of higher-order ketones molecules can be generated by consecutive aldol condensation after ketonization [51]. Currently, it has scope in production of many speciality chemicals like 2-ethylhexanal, isophorone, mesityl oxide, and crotonaldehyde [102]. This is a reaction between two ketones/aldehydes to yield higher order ketone molecule, as shown in figure 2.14 [51]. Similar to ketonization, it had been carried out in both domains of homogeneous and heterogeneous catalysis (zeolite, metal oxides) and, there exist both cross and self aldol condensation [102, 103].

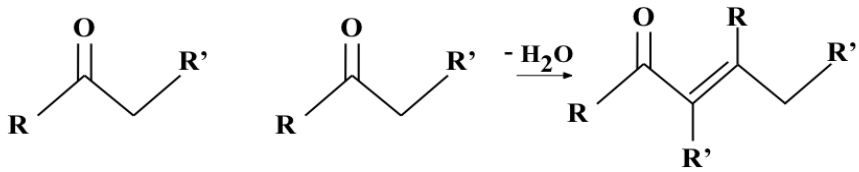

Figure 2.14: Aldol condensation reaction. "R" and "R′" = Different alkyl groups

Previous literature report that aldol condensation reaction had been carried over all three available variants such as acidic, basic and acid-base catalyst [104]. Vapour and aqueous phase aldol condensation reaction had been carried out over alkali and alkaline earth oxides, hydrotalcite and phosphate catalyst [104]. Vapor phase condensation of acetone to methyl isobutyl ketone by Mg-Zr and Mg-Ti based base catalysts had been reported [104]. TiO_2 with other catalyst had been considered one of the active catalyst for aldol condensation [105]. The catalyst had been reported to undergo rapid deactivation based on time of stream of the reaction [102, 105]. Handful literature (based on TiO_2, Cr-ZrO_2) on aldol condensation in direct over vapour phase up-gradation of biomass-derived oxygenates is available [106, 107]. The proposed reaction mechanism for aldol condensation had also shown an requirement for ketonization reaction. Therefore, proposal on latter mechanism will be discussed in brief since the discussion is also shared by the former one [52]. Overall, aldol condensation is mostly referred to as a complementary reaction with ketonization. Refer section 2.10.1 for the mechanistic overview on aldol condensation.

Both the C-C coupling reaction can be coupled in a single reactor or consecutive reactor given ketonization takes place prior to the aldol condensation. This pre-requisite is due to the deactivation of the basic sites by carboxylic acids which is needed for catalyzing aldol condensation. An major concern in coupling both the reaction is the poisoning of aldol condensation catalyst by CO_2, H_2O produced in the process of ketonization and other biomass-derived oxygenates [108]. Similar to ketonization, Water and carbon dioxide molecule had also been reported to have negative impacts on the aldol condensation catalyst [51, 108]. In this master thesis, dedicated catalyst synthesis for aldol condensation is not synthesized. Complimentary aldol condensation with ketonization over single catalytic bed (ex-situ) is approached.

2.9.3 Hydrodeoxygenation

The carbon loss could be minimized by via ketonization and aldol condensation, as discussed in previous section 2.9.1 and 2.9.2. The next stage is to remove the leftover oxygenates from un-reacted carboxylic acid, ketones from the ketonization and aldol condensation respectively, aromatics (weighs 30 wt.% of non-catalytic bio-oil) etc. In this regard, catalytic deoxygenation is chosen as an attractive route. The main objective is to remove oxygen as H_2O instead of CO_2 and CO. Hence, carbon loss is further minimized through hydrodeoxygenation (HDO). Therefore, cascade catalytic configuration of ketonization, aldol condensation and hydrodeoxygenation catalyst could maximize the carbon content in the bio-oil. Additionally, the solvent-less HDO is advantageous over the aqueous phase up-gradation by avoiding solvent separation and aviding unwanted heating of reactant mixture which includes solvent [109].

The HDO is an exothermic reaction which is usually carried out at temperature 127-500°C and high partial pressure of H_2. A simplified HDO reaction was previously shown in figure 2.6, which yield a deoxygenated product and H_2O as a byproduct. Similar to ketonization at atmospheric pressure, atmospheric HDO had attracted many researchers in the past decade. The complexity exists in understating the reaction pathway for HDO due to multiple simultaneous chemical reactions. Therefore, utilization of oxygenated model compounds of bio-oil simplifies the issue and aids in screening the active catalyst for HDO, as observed for ketonization in section 2.9.1 [110]. Trine at al. and Resende et al. had reported a comprehensive review on the HDO catalyst, however, herein, the atmospheric HDO catalyst is given the main focus [13, 33]. Table 2.11, 2.12, 2.13, 2.14, 2.15, 2.16, 2.17, 2.18, 2.19, 2.20, 2.21, 2.22 and 2.23 summarizes the last ten years of atmospheric HDO on biomass-derived oxygenates. The main focus is given to the direct vapour phase up-gradation of bio-oil vapours. Therefore, other studies of HDO of vegetable, algal oil, production of speciality chemical via HDO is not included in this scope of review.

The requirement for an efficient HDO catalyst is hydrogenation and hydrogenolysis/dehydration property. The metal site provides the former whereas the latter is provided by the acid sites. The underlying mechanism is to activate the C-O bond present in the oxygenates by acid sites. Consequent hydrogenation and dehydration of C-O bond by the vicinal metal site perform a successful HDO. Overall, at least dual-site is needed on a catalyst for catalyzing an effective HDO reaction [111, 112]. Zanuttini et al. reported the observation on the optimum balance between the metal and acid function of catalyst (Pt/Al_2O_3) [113]. Earlier studies on HDO were reported on the conventional catalyst utilized in hydrotreating petroleum feedstock. These were metal sulphide (Co-Mo/Ni-Mo) based catalyst. The main requirement is to keep the catalyst in sulphided form. Despite the high activity of the catalyst, product contamination by sulphur was a major concern. It had been reported that sulphur on the catalyst ends up in the stream irrespective of H_2S co-feeding [33]. In contrast, un-sulphided Ni-Mo composite and Ni-Mo/SiO_2 catalyst had been reported to show high HDO activity over anisole (200°C) and p-cresol (400°C) [114, 115].

Majority of the atmospheric HDO studies shows the utilization of noble metals (Pt, Pd, Ru) either as an abundant species or promoter. It was observed from HDO of pinewood,

Pt promoted H-Beta & HBEA increased deoxygenated products and monoaromatic production compared to their corresponding support [116, 117]. Additionally, the synergy between the Mo and Pt species was observed in the HDO of dibenzofuran [118]. A primary concern over the hydrogenating metal was the complete saturation of the aromatic compounds leading to over-consumption of hydrogen. However, Pd-Fe/carbon was observed to suppress the effect of over-saturation [119]. Similar to Pt, Pd and Ru were utilized in atmospheric HDO, suppressing coke formation and polyaromatic compounds. The promotional effect of nobel metal was observed on Pd/Nb_2O_5. The catalyst showed HDO activity only after Pd doping which otherwise was inactive during activity testing [120]. Meanwhile, Ru and Pd were reported to promote dispersion and stabilizing of Ni over Ru-Ni/Al-SBA-15 and active species Fe (reduced valence state) in Pd/Fe_2O_3, respectively [121, 122].

The non-noble metal had drawn mounting attention in atmospheric HDO due to low cost compared to other metals [110]. These include base metals (Ca, Mg), metal oxides (TiO_2, ZrO_2, SiO_2, Al_2O_3, MoO_3, Nb_2O_5, CeO_2), phosphides (Ni_2P), carbides (Mo_2C, W_2C), nitrides and so on, as shown in table 2.11, 2.12, 2.13, 2.14, 2.15, 2.16, 2.17, 2.18, 2.19, 2.20, 2.21, 2.22 and 2.23. Ru/TiO_2 showed high HDO compared to other supports such as C, SiO_2, Al_2O_3 on HDO of guaiacol at 400°C [123]. HDO of cresol, anisole and guaiacol was conducted over Fe/ZrO_2, $FeReO_x$/MCM-41 and Fe/HBeta at 300 and 350 °C. The Fe/ZrO_2, $FeReOx$/MCM-41 were active than the Fe/Hbeta [124]. Interestingly, bi-promoted metal function over acid catalyst had also shown high efficiency as an HDO catalyst for bio-oil compared to mono-metallic counterpart. Compared to noble metals, an interesting aspect was observed over Ni and Cu combination. Ni is attributed to its high hydrogenation property, low cost, and alloying efficiency. On the other hand, copper is by nature an hydrogenating metal. This combination of Cu with Ni was observed to decrease coking, reduction temperature, high-temperature methanation reaction and carbon-carbon bond breakage over Ni [111]. In the meanwhile, oxide material with transition metals also posses the requirement for catalyzing HDO [112]. Additionally, composite oxide of ceria-zirconia were also observed to be active in HDO [125].

According to the literature, there are two other critical requirement of the HDO catalyst. Firstly, benzene ring suppression is an important context in preventing the loss of aromatic compounds. thereby minimizing unwanted hydrogen consumption by ring saturation. In this regard, ceria oxide was inactive towards ring saturated products in HDO of anisole at 698 K [126]. Wu et al. observed that Ni-based catalyst was inactive towards ring saturation in atmospheric HDO, which led to selective aromatic product distribution[127]. No ring saturation was reported over Cu supported on SiO_2 [128]. Similarly, Fe/AC showed negligible ring saturation at 350 and 450°C [119]. Wang et al. had introduced In into Nickel which by nature does not have hydrogenation abilities. However, it was proposed that the charge transfer from In to Ni made it unfavorable for adsorption of electron rich benzene compounds, thereby suppressing aromatic ring saturation [129].

Secondly, the oxophilic nature of catalyst. The selectivity towards HDO products is dependent on higher oxophilicity of the metal (for instance, In is more oxophilic than the Ni) and support material [130]. For example, ZrO_2, TiO_2, Nb_2O_5 are oxophilic compared to SiO_2 [120]. The poor oxophilicity of the support in Pt/SiO_2 led to less than 1% benzene

yield from Guaiacol [131]. Teles et al. compared the extent of hydrogenation and direct deoxygenation of phenol to benzene with Pt, Pd, Rh, Co, Ni, and Ru over neutral silica support. The Ni, Ru and Co were reported to be selective towards benzene formation due to oxophilicity of metal, whereas the latter yielded saturated products [132]. Barrios et al. compared the support (Pd supported over Nb_2O_5, TiO_2 and SiO_2 effect on HDO of phenol. High oxophilicity of Nb_2O_5 led to 40 times higher selectivity towards benzene compared to other catalysts [133]. Similarly, De et al. observed that Pd supported on ZrO_2 was selective towards benzene production compared to Pd/Al_2O_3 and Pd/SiO_2 [134]. Additionally, the support also influence the formation of active centers for catalyzing HDO. For example, the formation of Ni_2P phase for HDO of guaiacol was easier on SiO_2 compared to due to strong association of phosphorous with latter support [135]. However, high acidity of Al_2O_3 support is prone to coke formation [135].

The biomass-derived oxygenates contains mono and multi oxygenated compounds. It is to be noted that the bond dissociation energy (C-O bond) is different for different oxygenates. For example, the phenol-O-phenol bond (diphenyl ether), phenol–O–methyl bond (guaiacol, anisole) is very reactive compared to aromatic-O bond (Phenol, guaiacol) and phenol–OMethyl bond (anisole or guaiacol) [136]. Therefore, phenolic ring saturation followed by C-O bond cleavage is preferred than Direct Dexygenation (DDO) route due to difference in C-O bond dissociation energy. DDO route is discussed in section 2.10.2. Although studies had been conducted on high-pressure selective DDO route over bi-metallic catalyst Pt-Sn, Rh-Pt, Pd-Fe, Ni-Cu, and Fe-Mo, herein, atmospheric HDO is given the main focus. In regards to atmospheric HDO, Pd/ZrO_2, reducible metals oxides (CeO_2-ZrO_2, MoO_3, TiO_2, ZrO_2 and so on), had shown high HDO activity due to oxophilicity of support. The oxygen vacancy selectively cleaves the oxygen atom from the oxygenated compounds via reverse Mars-van-Krevelen mechanism, which will be discussed in section 2.10.2. Recently, Mo_2C had also been proven to show HDO activity at atmospheric pressure [116].

As preciously mentioned, Lewis and Brønsted acidity is a requirement for HDO. The chemisorption of the oxygen atom from the oxygenates is accomplished by the former, whereas the latter provides the necessary hydrogen [33]. In regards to oxygenated compounds, the strength and distribution of the acid sites influences the HDO activity and coke formation [124]. Sirous et al. compared the HDO of guaiacol, anisole and cresol over Fe/HBeta , FeReOx/MCM-41, Fe/ZrO_2 at 350°C. The acid site strength were in the order of Fe/HBeta $>$ FeReOx/MCM-41 $>$ Fe/ZrO_2. On the one hand, the BTX formation from guaiacol was higher over Fe/Hbeta. On the other hand, BTX formation from cresol and anisole was higher over FeReOx/MCM-41, Fe/ZrO_2 compared to Fe/HBeta. This observation showed that higher oxygenated compounds requires large distribution and strength of acid sites compared to mono-oxygenated compounds . However, high acidity led coking over Fe/HBeta. [124]. The selectivity towards HDO of cresol was found to be higher for less Brønsted acid sites catalyst such as Pt/Al_2O_3 and SiO_2 compared to zeolite support [113]. Similar observation were reported by Daoyu et al. during HDO of p-cresol over Ni and Ni/Mo composite. The addition of Mo introduced medium and strong acidic sites compared to the weak acidic nature of Ni catalyst. It can be inferred that containing strong acidic sites does not necessarily be essential for high HDO activity [33]. Therefore opti-

mized distribution and strength of acid sites is also a major factor in HDO activity of the catalyst [114]. In this regard, Coan et al. reported the utilization of phosphonic acids to tune the Brønsted acidity of the support CeO_2, Al_2O_3 and TiO_2, thereby increasing the activity and selectivity towards HDO products. It is to be noted that the nature of phosphonic acid varied the strength of acid sites [137].

Apart from HDO and hydrogenation reaction, few of the reported catalyst in the literature is also active in transalkylation reaction. These are typically catalyzed by Brønsted acid sites [138]. This further reduces carbon loss during removal of the methoxy group, which is alkylated to one of the deoxygenated products instead of CH_4 formation. It was reported that 36-40% of methyl radicles are shifted to benzene ring during HDO of guaiacol and anisole under the optimal distribution of surface acid sites [115]. It is also observed that transition metals take part in partially in hydrogenolysis and transalkylation due to in the complete reduction of metals. For instance, Nie et al. found both the aforementioned reaction to take place on Ni/SiO_2 during the HDO of m-cresol [139]. Pt, Pd, Ru/ AC were active in demethylation whereas base metals such as Fe, Cu were active in demetholxylation of guaiacol [119].

Reaction condition also influence the HDO activity of the catalyst. Firstly, the temperature sensitivity of HDO of guaiacol was investigated by Xu et al. It was observed that increasing the temperature from 300 to 600°C, the gas and coke yield increased and decreased due to massive cracking of guaiacol. Partial deoxygenation to phenol was main product below 400°C. However, the highest degree of deoxygenation (benzene and toluene yield up to 70 %) was achieved when the temperature was rose up to 450°C [140]. A similar observation was reported for HDO of guaiacol where the high temperature at 400°C increased the gas yield due to deep cracking [141]. Other studies on temperature dependency of catalyst performance was studied by Sirous et al. [124]. Decreasing the reaction temperature to 350°C increased the activity of all the catalyst (Fe/ZrO_2, $FeReO_x$/MCM-41, Fe/Hbeta, $FeReO_x/ZrO_2$) towards HDO of cresol. It was inferred that ReOx was effective in HDO of phenolics at low temperature (<250°C) and atmospheric pressure compared to other catalyst [124]. Zhoa et al. also reported the sensitive nature of hydrodeoxygenation over reaction temperature. It was observed that MoO_3 becomes inactive due to the formation of reduced MoO_2 phase at temperatures above 400°C [142]. Xu et al. observed the decrease in ring saturation and increase in the formation of benzene from phenol while increasing the temperature from 300 to 400°C [141].

Secondly, the importance of H_2 as a sweep gas was reported by Prasomsri et al. Switching of H_2 flow in middle of experiment showed negligible HDO activity of acetone, 2-hexanone, anisole. However, switching back the H_2 supply regained HDO activity [143]. Additionally, it was observed that the hydrogen as a sweep gas influences the product distribution. Ausavasukhi et al. reported the selectivity towards BTX increases when switching the carrier gas from He to H_2 over Ga/HBeta [144]. Further, the catalyst deactivation is slowed down in the presence of H_2. Thirdly, in many cases, high H_2 pressure during HDO improves the conversion. However, aromatic ring saturation is observed [145, 146]. Fourthly, the residence time of the pyrolytic vapours plays an important role in any catalytic upgrading process. Xu et al. investigated the HDO of guaiacol over MoOx based catalyst. It was found that short residence time led to incomplete conversion of guaiacol

and relatively long residence time led to over cracking of complete HDO products. An optimal retention time gave the full conversion and maximized the yield of complete deoxygenated product (benzene) over the partial deoxygenated product (phenol) [140]. Other parameters, such as reduction temperature, influence the selectivity towards aromatic ring saturation or DDO pathway. Teles et al. observed the higher reduction temperature during cobalt-based catalyst yielded high saturated products compared to DDO of benzene [132]. Additionally, high reduction temperature during catalyst preparation also led to decreased HDO activity due to sintering [124].

Similar to ketonization applicability with real biomass, HDO of real biomass suffered the same issues. For example, the HDO over MoO_3 were compared with the model compounds and real biomass (lignin, pinewood). It was observed that the conversion and selectivity were $>$50% and 100% respectively, over model compounds. The degree of deoxygenation was 52% in the organic yield of lignin hydropyrolysis at 450°C. Unfortunately, only 4.6 wt.% organic yield was obtained with no oxygenates, which could not give insights on degree of deoxygenation of pine powder [142]. Secondly, it was reported that co-feeding acetone with lignin decreased the conversion of acetone, once the lignin vapours reached the catalyst bed. This shows the sophisticated applicability of real biomass with the superior catalyst reported during the HDO of model compounds [142]. Therefore, conversion and selectivity from the table 2.11, 2.12, 2.13, 2.14, 2.15, 2.16, 2.17, 2.18, 2.19, 2.20, 2.21 and 2.22 should be taken with caution. In contrast, few insights from model compounds were similar to the observation from HDO of real biomass. Table 2.23 summarizes the atmospheric HDO of real biomass. Zhoa et al. tested the HDO of real lignin in a fixed-bed reactor. It was shown that the methoxy group over the phenol is easy to remove than the hydroxyl group [142]. Xu et al. reported similar observations. The phenolic yield was higher compared to benzene [141].

Main catalytic deactivation was due to sintering, coking, oxidized/reduced active phase of the catalyst. This consequently led to a decrease in the surface acid-base properties of the catalyst [147]. Firstly, the adsorption of pyrolysis intermediate over the catalyst surface differs over the metal, acids and oxide. The coking is mainly due to strong adsorption of the reactant (oxygenates)/product (coke precursors) adsorbate. It was observed that double functionalized oxygenates (guaiacol and catechol) adsorb strongly than a monooxygenates (anisole and phenol) [148]. However, the stability of the catalyst can be improved by the hydrogenation function of metal centres. Yung et al. increased the lifetime of HBEA by the hydrogen spillover by Pt metal [116]. Secondly, the HDO activity was observed to decrease with temperature rise from 300 to 500°C over Pd/Nb_2O_5. These were attributed to sintering of Pd metal and coverage NbOx over Pd particles [133]. Thirdly, it was observed that water had an negative impact on HDO activity over MoO_3. However, the deactivation was overcome by increasing the partial pressure of H_2 in the sweep gas [143]. On contrary, the water which was observed to suppress the ketonization catalyst promoted the conversion and stability of the Pt/SiO_2 and HBeta. Nie et al. studied the HDO of Guaiacol. It was observed that the water aids in hydrolyzing the ether bonds present in guaiacol while Pt hydrodeoxygenated the hydroxyl groups of oxygenated compound [131].

S.No	Model compound	Reaction temperature	Catalyst	Conversion & selectivity (%)	Comments
1[149][a]	m-Cresol	300°C	5wt.%Ni-2.5wt.%Re/SiO_2	Conversion = 94; 3-methylcyclohexanone, 3-methylcyclohexanol and toluene	1) Re promoted HDO over hydrogenolysis, thereby decreasing the loss of carbon as CH_4. 2) HDO increased with temperature.
2[150][b]	Dibenzofuran	360°C	3 wt.% Co/MoO_3	Conversion = 40; Biphenyl selectivity =100	1) Co promoted the HDO compared to parent MoO_3.
3[151][b]	Furfural	200°C	Co/SiO_2	Conversion = 10; 2-methylfuran selectivity= 15	1) Increase in pressure and temperature improved the HDO activity and 2-Methylfuran selectivity, resp.
4[152][b]	m-Cresol	350°C	1 wt% Pt/TiO_2	Conversion = 15; toulene selectivity= 30	1) Pt metal clusters proved superior towards HDO compared to isolated Pt atoms over support due to active interaction with adsorbate and dissociation of H_2 molecule.
5[127][b]	Phenol	300°C	Ni/Nb_2O_5	Conversion = 16; Benzene selectivity =97	1) Higher reduction temperatures favours direct deoxygenation pathway.

a: Quartz fixed-bed reactor; b: Fixed-bed reactor

Table 2.11: Atmospheric HDO of model compounds-I

S.No	Model compound	Reaction temperature	Catalyst	Conversion & selectivity (%)	Comments
6[127][a]	Guaiacol	350°C	10-wt.% La - 20wt.%-Ni/HUSY	Conversion =97.96%; aromatics selectivity = 7.7	1) Ni is active sites for HDO and hydrogenation reaction and increases with Ni loading. 2) La promoted better dispersion of Ni and reduce sintering.
7[118][a]	Dibenzofuran	400°C	Pt/7MoO_x/MgO	Conversion = 70%; biphenyl selectivity = 100	1) Overloading Mo decreased the HDO activity due to formation of MoO_3 cyrstallites. 2) MoO_x and Pt were responsible for C-O bond activation and hydrogenation, resp.
8[126][b]	Anisole	425°C	CeO_2	Conversion = 7.7; benzene selectivity < 85	1) Direct deoxygenation observed without aromatic saturation. 2) The selectivity towards benzene increased with hydrogen pressure.
9[124][a]	Cresol	350°C	$FeReO_x/ZrO_2$	UN;BTX selectivity = 61.7	1) ReO_x aided in tuning the acidity and promoted dehydration and HDO resp. 1) ReO_x aided in dispersion of iron oxide on the catalytic support.

a: Tubular fixed-bed; b: Quartz fixed-bed.

Table 2.12: Atmospheric HDO of model compounds-II

S.No	Model compound	Reaction temperature	Catalyst	Conversion & selectivity (%)	Comments
10[133][a]	Phenol	300°C	Pd/Nb_2O_5	UN; Benzene selectivity =80.2	1) Highest selectivity due to oxophilicity of the support.
11[114][b]	p-Cresol	200°C	Ni/Mo composite	Conversion =100; HDO rate (Toulene) = 91.4;	1) Mo incorporation increased porous structure, thereby, increasing surface area and active sites. 2) Increased the distribution and strength of active sites compared to pure Ni which led to high HDO activity.
12[153][b]	Guaiacol	350°C	Ni_2P/SiO_2	Conversion =78; phenol and anisole selectivity = 68 and 15	1) Catalyst deactivation is observed due to coke deposition, sintering and reduction in acid sites due to reduction of metal sites in H_2 atmosphere.
13[153][b]	Anisole	350°C	Ni_2P/SiO_2	Conversion =62; phenol and benzene selectivity = 35 and 65	-
14[115][b]	Anisole	410°C	$Ni\text{-}Mo/SiO_2$	Conversion = 99.35; benzene, toulene selectivity = 66.23, 24.26	-
15[154][a]	Anisole	200°C	Mesopororus Mo_2C	Conversion= 4; benzene, cyclohexane selectivity = 80, 20	-

a: Quartz fixed-bed; b: Tubular fixed-bed; UN = unknown

Table 2.13: Atmospheric HDO of model compounds-III

S.No	Model compound	Reaction temperature	Catalyst	Conversion & selectivity (%)	Comments
16[131][a]	Guaiacol	350°C	Pt/HBeta	Conversion = 100; benzene, toluene, xylene selectivity = 42, 29 and 12	1) Pt loading aided in direct deoxygenation of the phenol intermediate which was not preferred route over HBeta. 2) Pt decreased the coke formation by hydrogenation and deoxygenation reaction compared to HBeta.
17[115][b]	Guaiacol	410°C	Ni-Mo/SiO_2	Conversion = 99.79; benzene, toluene selectivity = 64.33, 27.43	1) Carbon loss was decreased by increased alkylation over the deoxygenated products by producing (toulene, xylene). 2) No aromatic saturation was observed.
18[155][b]	Furfural	240°C	CuAlCo Alloy (nanoporous)	Conversion = 98.02; 2-MF selectivity = 66	1) Deactivation was due to coke formartion rather structural changes. 2) No ring opening products were observed.
19[154][a]	Anisole	200°C	Mesoporous W_2C	Conversion= approx 1.2; benzene selectivity = 96	-

a: Quartz fixed-bed; b= Tubular fixed-bed

Table 2.14: Atmospheric HDO of model compounds-IV

S.No	Model compound	Reaction temperature	Catalyst	Conversion & selectivity (%)	Comments
20[119][a]	Guaiacol	450°C	2wt%-Pd-10wt-%Fe/C	Conversion = 98; benzene selectivity = 75	1) The support is active in demethylation to noticeable extent. 2) No aromatic saturation observed.
21[143][b]	Anisole	500°C	MoO_3	Conversion = 65; benzene, toluene selectivity = 38.7, 12.7	-
22[135][a]	Guaiacol	300°C	Ni_2P/SiO_2	Conversion = 99.5; benzene, toluene selectivity = 71,9, 1.9	1) Ring saturation was to be negligible. 2) more acidic support led to increase in Ni_2P crystallite size.
23[156][a]	Guaiacol	400°C	Ru/TiO_2	Conversion = 100; BTX selectivity = 50	1) Transmethylation is dominant reaction compared to other support. 2) No deoxygenated products observed.

a: Quartz fixed-bed; b: Tubular fixed-bed

Table 2.15: Atmospheric HDO of model compounds-V

S.No	Model compound	Reaction temperature	Catalyst	Conversion & selectivity (%)	Comments
24[136][a]	Phenol	320°C	MoO_3	Conversion =28.7; benzene, toulene selectivity = 26.90, 28.7	1) No ring saturation observed. 2) Promotes transalkylation.
25[136][a]	m-Cresol	320°C	MoO_3	Conversion = 48.9; benzene, toulene selectivity = 0, 48.6	-
26[136][a]	Anisole	320°C	MoO_3	Conversion = 78.7; benzene, toulene selectivity = 44, 15.6	-
27[136][a]	Guaiacol	350°C	MoO_3	Conversion = 97.5; benzene, toulene selectivity = 32.8, 9.4	-
28[136][a]	Diphenyl ether	320°C	MoO_3	Conversion = 82.6; benzene selectivity = 71.8	-
29[157][a]	guaiacol	300°C	Ni_2P/SiO_2	Conversion = 80; benzene, phenol selectivity = 60, 30%	-
30[128][a]	Furfural	230°C	10 wt.%-Pd/SiO_2	Conversion = 69; furan, tetrahydrofuran selectivity = 60, 20	-

a: Fixed-bed reactor

Table 2.16: Atmospheric HDO of model compounds-VI

S.No	Model compound	Reaction temperature	Catalyst	Conversion & selectivity (%)	Comments
31[148][a]	Guaiacol	400°C	Pt-Sn/CNF/ Inconel monolith	Conversion = 95; benzene, phenol selectivity = 5, 70	1) CNF increased the dispersion. 2) Pt-Sn alloy improved the HDO activity compared to its parent counterpart.
32[144][a]	m-Cresol	400°C	Ga/HBeta	Conversion =71.64; benzene, toluene selectivity = 6.12, 21.67	1) Ga addition reduced the Brønsted acidity, thereby reduction in heavy products. 2) BTX selectivity increased with temperature and gallium loading resp.
33[146][b]	m-Cresol	400°C	Pt/SiO_2	Conversion = 54.9; toluene selectivity = 77.9	1) Negligible dehydration was observed over SiO_2, however, the catalyst was superior over Pt/Al_2O_3. This is attribute due to weak acidity (near neutral surface), partially dehydrating the hydrogenated cresol molecule by Pt. 2) Aromatic ring saturation observed
34[158][a]	Anisole	400°C	Pt/HBeta	Conversion = 100; benzene, toluene selectivity = 50, 25	1) No aromatic saturation. 2) Pt aids in splitting H_2 and synergism accelerates the HDO and transfer of methyl group.

a: Quartz fixed-bed; b: Tubular fixed-bed

Table 2.17: Atmospheric HDO of model compounds-VII

S.No	Model compound	Reaction temperature	Catalyst	Conversion & selectivity (%)	Comments
35[159][a]	Anisole	400°C	Ni_2P/SiO_2	Conversion = 70.8; benzene and phenol selectivity = 54.6 and 45.4	-
36[117][b]	Anisole	400°C	1.3 wt.%-Pt/HBEA	Conversion = 90; benzene, toulene, xylene yield = 4, 4, 1	1) Production of BTX was only due to doping on Pt on HBEA.
37[141][b]	Guaiacol	300°C	Fe/Ni/HBeta	Conversion = 100; benzene and phenol yield 1, 37	1) No prominant aromatic ring saturation was observed. 2) Transmethylation was observed to prevent carbon loss.
38[132][b]	Phenol	300°C	Ru/SiO_2; Ni/SiO_2	Conversion =12.4 & 14.7; Benzene yield = 5.8 & 4.8	1) Ru gave the highest degree of HDO on the expense of producing 62.3% selectivity towards CH_4 whereas 7.2% selectivity was observed from Ni based catalyst.
39[125][b]	m-Cresol	375°C	$Ce_{0.6}0Zr_{0.18}O_2$	Conversion =67; phenol, cresole, benzene selectivity = 88, 10, less than 2	1) Major product were partial deoxygenated compounds over mixed support. 2) Zr doping increased the oxygen vacancy over the catalyst.

a: Tubular fixed-bed; b: Quartz fixed-bed

Table 2.18: Atmospheric HDO of model compounds-VIII

S.No	Model compound	Reaction temperature	Catalyst	Conversion & selectivity (%)	Comments
40[160][a]	Guaiacol	425°C	Ni_2P/SiO_2	Conversion = 75; benzene, phenol selectivity = 25, 47	1) No benzene formation occurred compared to other support (ASA*, ZSM-5**, FCC***) 2) The acidic supports were selective to form catechol and phenols
41[113][a]	m-Cresol	300°C	Pt/Al_2O_3	Conversion = 70; toulene selectivity = 90	1) Higher metal to acid sites is selective towards HDO, or else cracking of heavy products formed on the catalyst is observed.
42[161][a]	Guaiacol	300°C	Ni_2P/SiO_2	Conversion = 99.8; benzene and phenol selectivity = 22.8, 23.9	1) Increasing P content decreased the Ni content, thereby decreasing HDO activity. 2) Deactivation observed due to coking and phosphide leaching.
43[145][b]	Guaiacol	300°C	Pt/C	Conversion = 87; toulene, catechol selectivity =44, 26	-
44[122][b]	m-Cresol	300°C	$5wt.\%Pd/Fe_2O_3$	Conversion = 90; benzene, xylene, toluene selectivity = 50%	1) Fe is suggested to promote HDO and Pd for hydrogen dissociation, stabilization of Fe (reducing the oxidized Fe) and facilitating product desorption.

*: Si–Al-1 = ASA; **: Zeolite Socony Mobil–5 ***: Fluid catalytic cracking catalyst
a: Quartz fixed-bed; b: Tubular fixed-bed

Table 2.19: Atmospheric HDO of model compounds-IX

S.No	Model compound	Reaction temperature	Catalyst	Conversion & selectivity (%)	Comments
45[162][a]	Guaiacol	350°C	Fe/Ni/HY zeolite	Conversion =100; benzene, toulene, xylene and phenol yield = 1, 6, 7, and 54	1) The Hydrogenolysis of ether bond is easier than OH groups over phenols. 2) The micropore volume, high acidity were responsible for high activity compared to other catalyst. 3) The transmethylation for reducing carbon loss was effective in HBeta pore structure compared to ZSM-5 and silica.
46[138][a]	Anisole	320°C	15wt%-MoO_3/ZrO_2	Conversion =62; benzene, toluene, and higher alkylated aromatic products =41	1) Deoxygenated product increased with Mo loading (1-15 wt.% loading). However, the overloading(15-36 wt.%) decreased the activity due to formation of MoO_3 crystallites. 2) Oligomerization of MoOx species makes the difference in linear increase in activity until monolayer formation. 3) HDO and alkylation reaction increased upto monolayer coverage of Mo species.

a: Tubular fixed-bed

Table 2.20: Atmospheric HDO of model compounds-X

S.No	Model compound	Reaction temperature	Catalyst	Conversion & selectivity (%)	Comments
47[163][a]	m-Cresol	300°C	Pd/ZrO_2*	Conversion = 60; toluene selectivity =50	1) Dealkylation and transalylation were not present. 2) Aromatic ring saturation observed. 3) The support increased the HDO activity and toluene selectivity compared to other catalyst
48[139][a]	m-Cresol	300°C	5wt.% Ni–5wt.% Fe/SiO_2	Conversion = 13.7; toluene selectivity = 52.6	1) Fe impregnation over the Ni/SiO_2 shifted the product selectivity from aromatic saturated product (3-methylcyclohexanone) to toluene. 2) Increase in Fe loading, increased the HDO activity and reduces ring hydrogenation (pure Fe exhibit low toluene production).
49[164][a]	Phenol	280°C	Ag/TiO_2	Conversion=74.75; benzene selectivity = 75.5	1) Direct deoxygenation was preferred route compared to ring hydrogenaion at high temperatures due to thermodynamic limitation of hydrogenation reaction. 2) Increase in H_2 flow rate increased selectivity towards ring saturation.

*: Pd precursor of $Pd(NO_3)_2$
a: Quartz fixed-bed

Table 2.21: Atmospheric HDO of model compounds-XI

S.No	Model compound	Reaction temperature	Catalyst	Conversion & selectivity (%)	Comments
50[147][a]	Phenol	300°C	Pd/tetragonal-ZrO_2	Conversion =85%; benzene, cyclohexanone selectivity = 80, 1	1) The HDO was attributed to metallic/bimettalic and metal support interaction. 2) The high HDO activity was due to high Lewis acidity (oxophilic sites) compared to monoclininc-ZrO_2. 3)Deactivation due to coke deposition, sintering of Pd metal and decrease in lewis acidity of the support.
51[165][a]	Acetone	300°C	Mo_2C	-	1) Majority of acetone undergoes hydrogenation (97% yield) rather than HDO forming Isopropanol and propene/propane respectively. 2) HDO and hydrogenation reaction was independent of H_2 partial pressure. 3) Negligible HDO of acetone was observed.

a: Quartz fixed-bed

Table 2.22: Atmospheric HDO of model compounds-XII

S.No	Feedstock	Reaction temperature	Catalyst	Comments
1[166][a]	Wheat straw	400°C	$PtTiO_2$, MoO_3/TiO_2, Mo/Al_2O_3	1) Pt/TiO_2 showed lowest coke yield, oxygen content, total acid number (TAN) in bio oil and decreased combustion temperature for coke removal. This is attributed to high hydrogenation activity and HDO activity of the catalyst.
2[167][b]	Pine wood	pyrolysis & catalytic bed temp = 450 & 500°C,	(1:1)Ni-Ce/ HZSM-5	1) Ni loading increased the Poly Aromtic Hydrocarbons (PAHs) formation and led to faster deactivation. 2) Addition of Ce increased the basicity, thereby,improving HDO and decreasing coke formation by reduced PAHs formation
3[116][c]	Pine wood	500°C	Pt/HBeta	1) Pt reduced the coke formation by hydrogenating the intermediate radicals. 2) De-oxygenated products were higher compared to HBeta. 3) Selectivity to mono-aromatics increased compared to 3 ring aromatic hydrocarbon.
4[142][d]	Wheat straw	450°C	MoO_3	1) The MoO_3 becomes inactive due to reduction at experimental temperature (forming MoO_2). 2) The phenolic content increased compared to methoxy phenol in upgraded bio oil.
5[142][d]	Pine wood	450°C	MoO_3	2) Less than 5 wt.% organic liquid was obtained with no oxygenated products. The degree of deoxygenation was not defined.

a: bench scale fast pyrolysis unit; b: Py-GC/MS; c: Quartz reactor; d: Ex-situ fixed bed upgradation

Table 2.23: Atmospheric HDO of real biomass-I

In this master thesis, 1 wt.% Ru-MoFeP/Al_2O_3 was synthesized as an HDO catalyst. This was exclusively prepared due to its high activity observed by a former PhD student at catalysis group, NTNU [104]. Model compounds such as acetic acid, acetol, furfural, guaiacol, eugenol and phenol representing the bio-oil were used as a feedstock. The up-graded bio-oil was analyzed after 12-hour run, and mass balance was determined. The organic phase and the oxygenates were reported to be 77% of the total feedstock fed in within 12 hours and 30% in the final bio-oil, respectively. The multifunctional catalyst gave 100% conversion of acetic acid, acetol, furfural, guaiacol, eugenol and 86% conversion for phenol. Herein, the conversion of phenol increased from 55 to 77 and 86% for MoFeP, MoFeP/Al_2O_3 and Ru-MoFeP/Al_2O_3, respectively. It was reported that charge separation between the MoFe and P species increased the lewis acid sites. This enhancement of lewis acidity was reported to decrease the activation energy required for the direct cleavage of the $C_{aromatic}$-O bond. This was in agreement with NH_3-TPD analysis, the lewis acid followed the order: Ru-MoFeP/Al_2O_3 > MoFeP/Al_2O_3 > MoFeP. The highest conversion of phenol over Ru-MoFeP/Al_2O_3 compared to MoFeP could be explained by the additional lewis acidity provided by the Ru and Al_2O_3. Overall, the enhancement in lewis acidity coupled with hydrogen spillover by the Ru was concluded the factors behind the high performance of 1 wt.% Ru-MoFeP/Al_2O_3. However, the HDO catalyst was validated at Weight Hourly Space Velocity (WHSV) of 0.94 h^{-1} 400°C, 20 total bar pressure (14.7 bar H_2) experimental condition. Therefore, the multifunctional HDO catalyst must be validated with real biomass feedstock at atmospheric pressure condition [104].

In the next stage, the tandem catalytic system was tested with C-C coupling (Au/TiO_2, Ru/TiO_2, Pd/TiO_2) and HDO catalyst in the H_2-Bio-oil mini pilot plant. The reaction condition and WHSV were similar to aforementioned HDO experiment. The gas phase decreased with increase in aqueous phase of bio-oil. Meanwhile CO_2/CO ratio increased over the dual bed catalyst. The up-stream catalyst was reported to be responsible high CO_2/CO ratio and aqueous phase formation due ketonization and aldol condensation reaction. Similar to HDO catalyst, 100% conversion of feedstock was observed expect for phenol. Herein, HDO catalyst coupled with Ru/TiO_2 showed the highest phenol conversion compared to Au and Pd/TiO_2 whereas Au/TiO_2 showed highest C-C coupling activity. The degree of deoxygenation in the dual bed catalytic system was observed to follow the order: Ru-TiO_2-Ru-MoFeP/Al_2O_3 > Ru-MoFeP/Al_2O_3 > Pd-TiO_2-Ru-MoFeP/Al_2O_3 > Au-TiO_2-Ru-MoFeP/Al_2O_3. The organic phase of the bio-oil increased and decrease in smaller oxygenates in the gas phase was observed. The carbon balance was over 95% for all the reported catalyst [104]. The tandem catalyst system in promising, however, similar to HDO catalyst, the catalyst must be tested with real biomass as feedstock to check its viability at large scale commercialization [104].

Overall, the tandem catalyst configuration of C-C coupling and HDO catalyst is an attractive route to decrease the concentration of oxygenates in the bio-oil while increasing the carbon recovery by coupling the smaller oxygenated molecule, which otherwise escape as gaseous product.

2.10 Catalytic reaction pathway

2.10.1 Carbon-Carbon coupling mechanism

Recently, the ketonization and aldol condensation had been reviewed due to its promising application in biomass conversion to fuels [52]. Therefore, it is important to know the mechanism of reaction in order to develop an efficient catalyst with optimal high activity, selectivity and stability. This section will review the current theories and proposals of ketonization and aldol condensation over heterogeneous catalyst.

As previously discussed in earlier section 2.9.1, ketonization occurs either via bulk ketonization or surface ketonization. For bulk ketonization, it is important to identify the potent metal oxides which are able to form bulk carboxylate salt which yields ketone upon thermal decomposition. On the other hand, surface ketonization requires the understanding the role of α-hydrogen and other intermediates such as ketene, β-ketoacids, adsorbed carboxylates, acyl carbonium ions, and acid anhydrides [52]. Pham et al. and Kulik et al. had recently reviewed previous literature on ketonization mechanism [53, 52]. In short, it is agreed that two intermediates are required in bulk ketonization mechanism to serve as a source for alkyl and acyl group fragments. These fragments lead to formation of a ketone product [52]. Herein, surface ketonization will be reviewed in detail which has been debated until now. The figure 2.15 shows all the reported debated mechanism on ketonization [53].

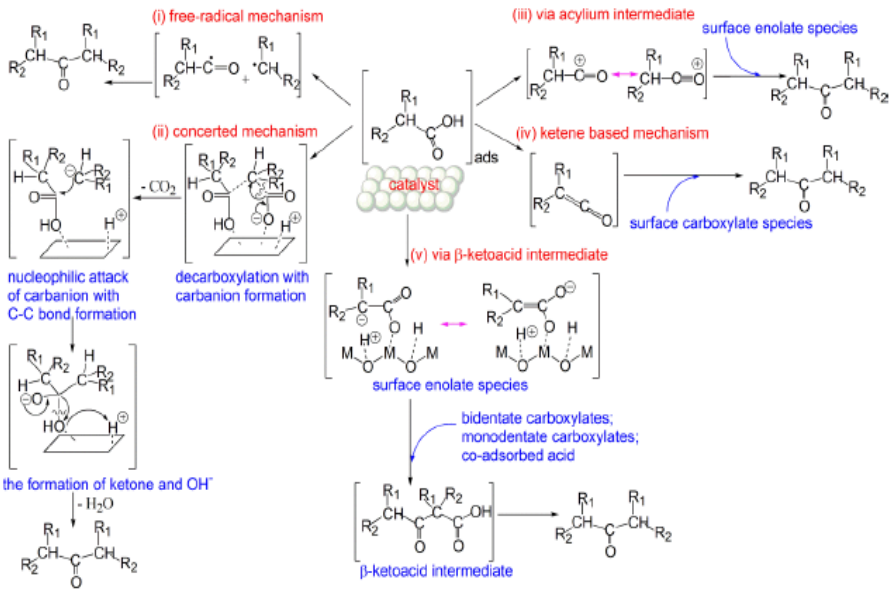

Figure 2.15: Debated ketonization mechanism [53]

Role of α-hydrogen

In the case of surface ketonization, α-hydrogen had always been one of the key requirement. α-hydrogen is the hydrogen atoms bonded to the α-carbon relative to the carbonyl group in the carboxylic acid molecule. Previous studies reported that hydrogen dissociation of the α-carbon is found to be higher than other alkyl groups present in the carboxylate molecule. This was supported by the pK_a value of dissociation of hydrogen from α-carbon (1920) compared to other alkyl group (4050) [52]. Hydrogen/Deuterium exchange studies also proved the existence of α-hydrogen in ketonization reaction. Contradicting to abstraction of α-hydrogen by the Brønsted basic sites of the metal oxide, alternative mechanism involving the abstraction of α-hydrogen via ketoenol tautomerization pathway had also been reported [168].

The presence of α-hydrogen had shown importance in both in self and cross ketonization. In self ketonization, proponoic acid (2 α-hydrogen) had shown to proceed at higher rate (10 times faster) compared to 2-Methylpropanoic acid (1 α-hydrogen). As expected, 2,2-dimethylpropanoic with no α-hydrogen had shown no conversion in self ketonization [52]. Similar conclusion were arrived in the case of cross ketonization [52]. Other studies includes self ketonization utilizing valeric and pivalic acids over ZrO_2. As expected self ketonization of valeric acid (2 α-hydrogen) and small amount of cross ketonization with pivalic acid (0 α-hydrogen) was observed [52]. Similar to α-hydrogen, equal importance is also given to the number of substituents at the β-carbon other than hydrogen. Previous studies report decreased ketonization activity in both self and cross ketonization with the increase in methyl group substituents at the β-carbon [52]. Kulik et al. showed the consequence of steric effect of substituents on the activation energy required for ketonization. The steric effect hinders the free rotation of the molecule in intermediate stage of reaction pathway for necessary conformation for ketonization reaction[53]. Overall, the importance of α-hydrogen seem to be crucial for ketonization. Yet, exact reaction pathway for the α-hydrogen abstraction is still debatable [52].

Ketene intermediate

This mechanism is based on the presence of atleast one α-hydrogen. The carboxylic acid molecule is adsorbed as a carboxylate species over the surface (unsaturated metal cations in oxide surface) by the abstraction of α-hydrogen by the Brønsted basic sites (oxides on the catalyst) of the catalytic surface. Next, an ketene molecule is formed by dehydration of carboxylate species. Finally, the ketene molecules is suspected to attack the alkyl group of adjacent carboxylate molecule. Yet, the exact mechanism of this coupling is not yet been elucidated [52]. A schematic reaction mechanism is shown in figure 2.16. The presence of ketene molecules was confirmed by FTIR studies by Munuera et al. [52]. It is suspected that driving force for the overall reaction will be the availability of unsaturated metal cations on the oxide surface [52].

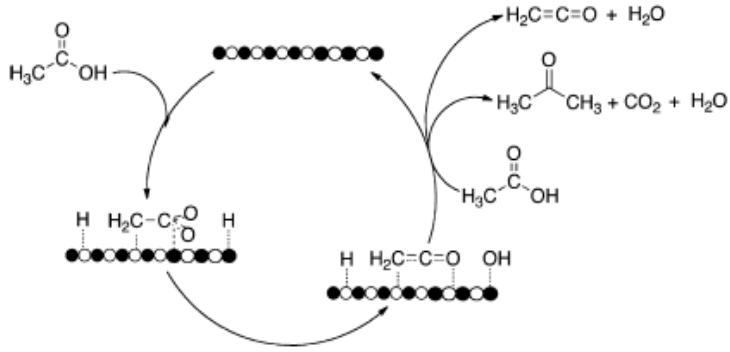

Figure 2.16: Ketonization of acetic acid by ketene based mechanism [52]

Contradicting results had been reported to disregard ketene based mechanism. Ponec et al. conducted ketonization between ^{13}C (^{13}C=O) labeled acetic acid and unlabeled pivalic acid (containing no α-hydrogen). It was observed that the carbonyl group of the formed cross-ketonization product (pinacoline) was from the pivalic acid. This contradicted the ketene based mechanism since it was proposed that carbonyl group of the cross-ketonization product (ketone) originates from the the carboxylate containing the α-hydrogen [169]. This study reported that ketene might be regarded as side product and not a crucial intermediate in ketonization reaction [52]. In regards to importance of ketene in ketnonization, temperature programmed studies involving decomposition of acetic acid over rutile TiO_2 had shed some insights. It was concluded that 2 pathways existed in ketone formation. The ketene formation was observed in (011) faceted surface whereas bimolecular ketonization was observed over 114 faceted surface of TiO_2 (Ti^{5+}). This was summarised by Pham et al. that ketene formation is not a crucial intermediate and rather a parallel reaction [52].

β-Ketoacid Intermediate

This mechanism is also based on the requirement of α-hydrogen for ketonization and 2 adjacent surface adsorbed carboxylate molecule. This mechanism had given interest due to the insights given on how evolution of CO_2 occurs during coupling reaction in ketonization. The β-Ketoacid is a compound which has a ketone group at the β- carbon from the carbonyl group of the carboxylic acid molecule [52]. The β-Ketoacid Intermediate has the readily decomposing nature at milder condition to yield CO_2 as a by product in ketonization which make this mechanism proposal more convincing [52].

Figure 2.17 shows the representation of β-Ketoacid based intermediate formation over $CeO_2-Mn_2O_3$ catalyst. The first step is the formation of 2 visinal carboxylate molecule on the unsaturated metal centers. This is accomplished by the abstraction of the α-hydrogen by the Brønsted basic sites. Herein, the abstraction of α-hydrogen complies with the aforementioned proposed mechanism. Second step is the attack of nucleophilic carbon (the place from where the α-hydrogen was abstracted) on the carbon (carbonyl group of the

adjacent carboxylate molecule). This leads to the formation of β-Ketoacid Intermediate and one water molecule. Finally, the formed intermediate decompose to ketone and CO_2 molecule [52].

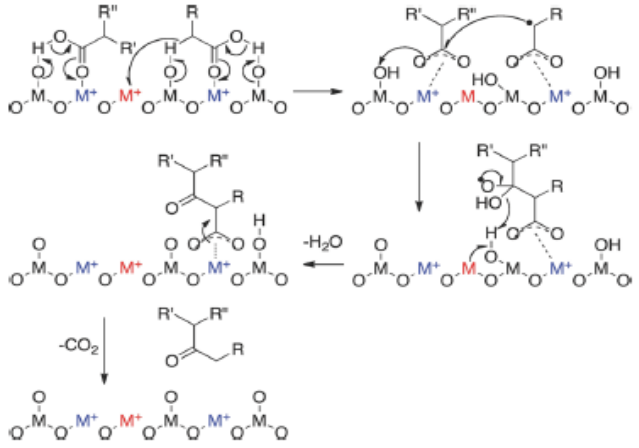

Figure 2.17: Proposed β-ketoacid based mechanism in gas phase over CeO_2-Mn_2O_3 catalyst [52]

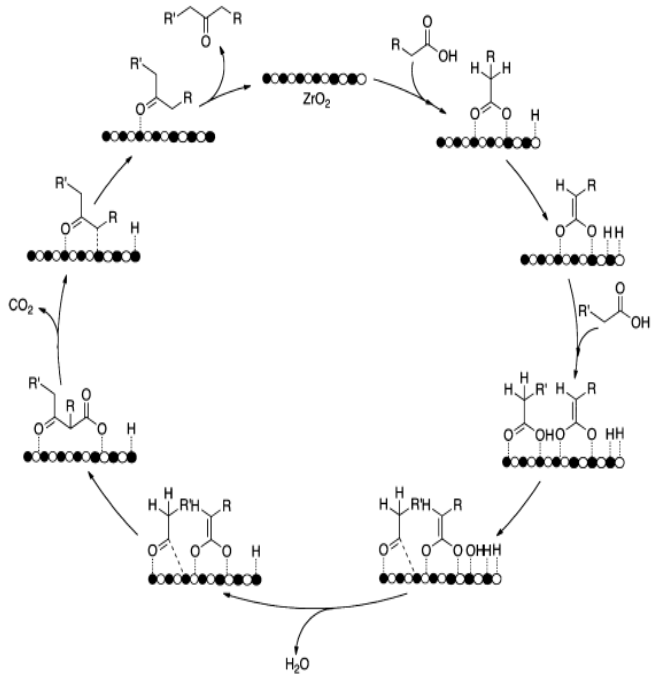

Figure 2.18: Proposed β-ketoacid based mechanism in gas phase over ZrO_2 catalyst [52]

In contradiction to the above proposed mechanism, Renz. et al. and Ignatchenko et al. suggested alternative pathway for the formation of β-Ketoacid Intermediate [52]. The intermediate was proposed to form via coupling of enolate (formed via abstraction of α-hydrogen from the carboxylate species) and acylium species (formed via removal of hydroxyl group from the incoming carboxylic acid molecule onto the surface) [52]. Figure 2.18 shows the proposed mechanism. However, it was reported the difficulty faced in differentiating between the carboxylate and acyl species over reducible oxide surface since acyl species can be readily converted to carboxylate species by the nucleophilic attack from lattice oxygen [52].

As mentioned earlier, the aldol condensation shares similar mechanistic pathway as ketonization reaction. It is suggested that the 2 aldehyde molecule adsorbs weakly on to the catalytic surface (via carbonyl oxygen) unlike carboxylate species. This step is followed by enolate formation by abstraction of α-hydrogen by the Brønsted basic sites (oxides species) similar to ketonization. Subsequently, a nucleophilic attack by the enolate species on the adjacent electrophilic acyl carbon of adjacent aldehyde which leads to formation of C-C bonds [52]. Therefore, dedicated discussion on aldol condensation is not included in this report.

2.10.2 Hydrodeoxygenation mechanism

The literature on HDO can be dated back to the past three decades. Recently, Trine et al. and Resende et al. had summarized an extensive work on HDO catalyst and mechanism [33, 13]. In this section, the catalytic mechanism over the sulphides, oxide and transition metal will be discussed.

Oxides

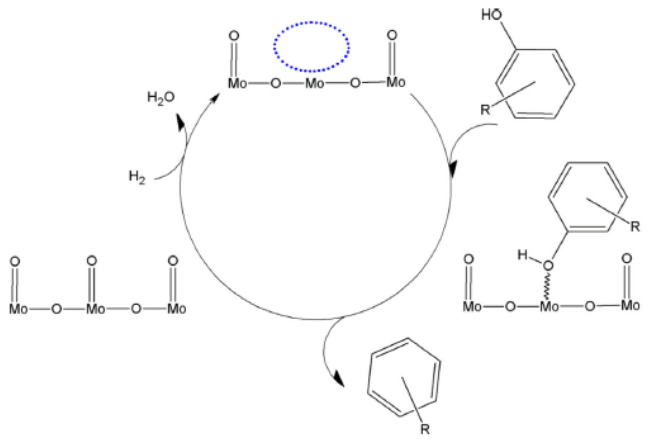

Figure 2.19: HDO reaction mechanism on reducible oxide [33].

Mo, Ni, Re, Nb based oxide had shown HDO activity, as discussed in section 2.9.3. The oxygen defect/vacancy plays a vital role in the deoxygenation step. The reverse Mars-van Krevelen mechanism is widely accepted over reducible metal oxide. An overview of the mechanism over the catalyst is shown in figure 2.19. The initial oxygen vacancy is created by the reduction of oxide surface (liberating as H_2O) in the H_2 atmosphere. Later, these vacancies are filled by the oxygen atom of the oxygenated compound. Finally, The C-O bond is cleaved after the electron transfer from active metal species of the oxide catalyst to the oxygen atom present on the oxygenates [33].

Sulphides

The proposed HDO mechanism over MoS_2 catalyst is shown in figure 2.20. It can be seen that the initial reduction of catalyst in H_2 atmosphere leads to the formation of H_2S, thereby creating an oxygen vacancy. This sulphur vacancy aids in interacting the oxygen atom of oxygenated compounds with the molybdenum metal (lewis acid). Consequently, the C-O bond of oxygenates is weakened by the formation of a carbocation on the α-carbon. This is accomplished by the proton transfer from the adjacent sulphur molecule to the carbon of the carbonyl group. In the last stage, the desorption of the deoxygenated product and water regenerates the sulphur vacancy [33].

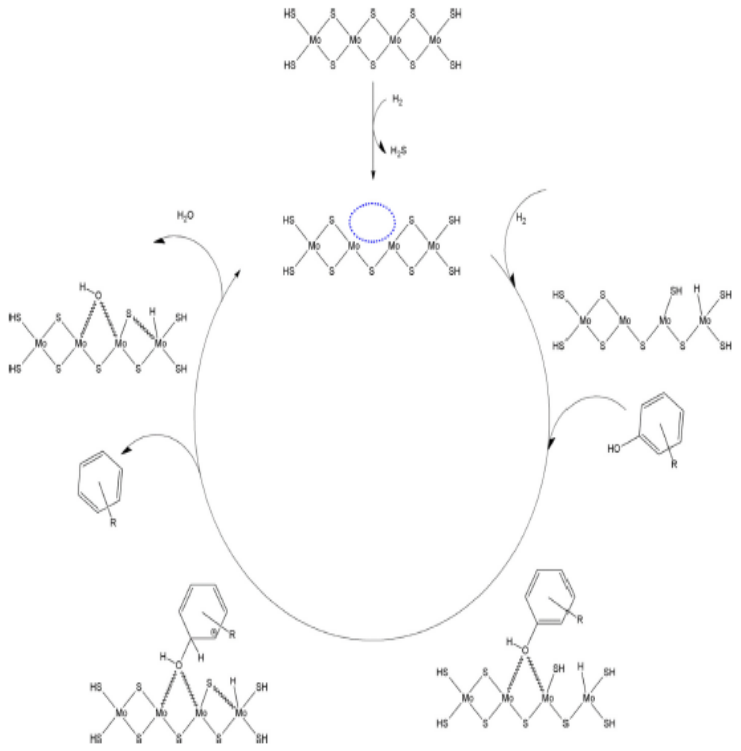

Figure 2.20: HDO reaction mechanism on sulphided catalyst (MoS_2) [33].

Reduced transition metals

Ni, Pt, Pd, Ru and Re based catalyst were also reported to be active in atmospheric HDO. Unlike oxide-based catalyst, these metals also contain hydrogenation ability. Due to this additional feature, the surface mechanism is different compared to the oxide-based catalyst. There are three different pathways for deoxygenation. Firstly, Mechanism A, which is otherwise known as direct deoxygenation route, as previously mentioned in section 2.10.2. Herein, the direct C-O bond cleavage of phenolic over the catalytic surface yield benzene. However, this pathway is hindered by the high bond dissociation energy of $\approx$ 468 KJ/mol [33].

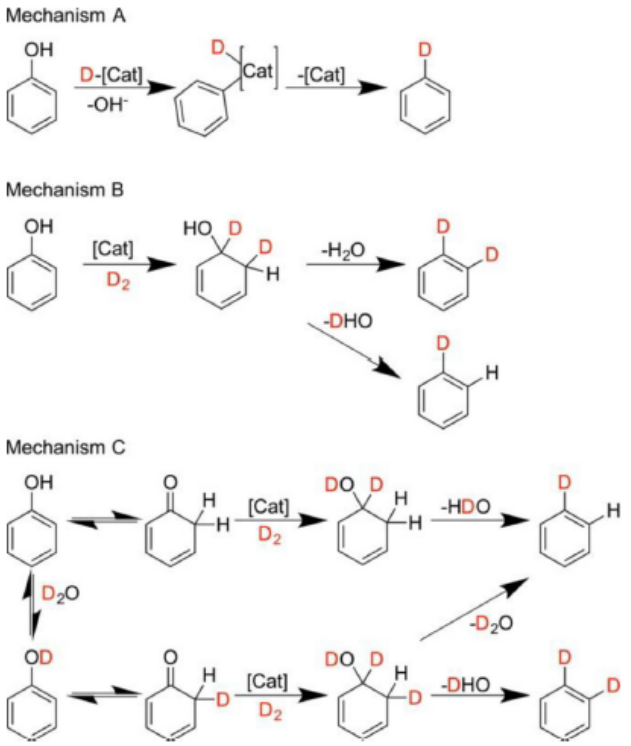

Figure 2.21: HDO reaction mechanism on reduced transition metal supported catalyst. D_2, D represents external hydrogen either present as a radical on the catalyst or in gas phase [33]

Alternative mechanistic routes were proposed based on experimental observation and the drawback of high bond dissociation energy observed in mechanism-A. Mechanism-B, and C relies on the hydrogenation function of the catalyst. In the former mechanism, the C-O bond in the phenol is weakened by hydrogenation at the ortho-position. Consequent dehydration step catalyzed by the acid sites produces benzene molecule. The latter mechanism is based on the tautomerization of the oxygenated molecule to its corresponding isomer. As shown in figure 2.21, Initial step is the transformation of phenol from enol to keto form. Later, the oxophilicity of the support facilitates the interaction between the

intermediate keto form of phenol to the catalytic surface. Similar to mechanism B, the reduced transition metal hydrogenates the C-O bond and ortho position of keto form of phenol at the metal-support interface. Finally, acid catalyzes the dehydration step and oxygen is removed as H_2O molecule [33].

2.11 Catalyst synthesis

2.11.1 Incipient wetness impregnation

The incipient wetness impregnation is also known as capillary impregnation or dry impregnation method. The basic principle is to determine the total pore volume of support material in which desired metals is to be loaded. The determined quantity of solvent from the previous step is used to dissolve the required amount of loading-metal salt precursors. The metal precursor solution is slowly dropped on to the support material. The metal species present in the solution will be pulled into the pores by the capillary forces. Later, the catalyst is dried to evaporate the solvent from the pores. This method is widely adopted in the industry due to its cheap, faster synthesis with good dispersion of the loading metal on the support. However, major downside is the low solubility of the metal precursor in the used solvent at higher loading [170].

2.11.2 Wetness impregnation

The wetness impregnation is utilizing more volume of the metal precursor solution compared to the total pore volume of the support material. The principle here is to drive the loading metal species into the pores of the support by the concentration gradient generated between the solution present inside and outside the porous grain structure of the support material. This migration is reported to be much longer than the capillary impregnation [171]. The final step is the drying of excess solvent at room temperature/heating oven.

2.11.3 Depositional precipitation

The depositional method is mainly utilized for high loading with good dispersion of metal species over the support material compared with above-mentioned catalyst synthesis procedures. The main principle is the conversion of highly soluble metal salts to another substance with low solubility, thereby selective precipitation over the support material rather in the solution is achieved. This transition is achieved by controlling the pH of the solution. In this regard, urea is used to control the pH effectively than sodium hydroxide. All the metals precursor, support material and required amount of urea are added, and the temperature is raised. The slow decomposition of the urea helps to control the pH, thereby maintaining a homogeneous pH throughout the solution during constant stirring. This prevents the unnecessary deposition of desired metal species and achieves good dispersion at high loading [172]. Finally, the catalyst is filtered, washed and dried.

Other advantages of depositional precipitation include deposition of weak interacting metal species over the support material (for example, deposition of inorganic Fe(III) salts over SiO_2 or Al_2O_3) [172]. The poisoning effect from chloride-containing noble metal precursor in a chemical reaction is minimized during the depositional precipitation method.

However, this synthesis method for the preparing catalyst is time consuming compared to the impregnation method [171].

2.11.4 Physical mixture

This catalyst synthesis method involves physically mixing two different catalyst material. The catalyst prepared by this method is used to compare the synergy between different metal species loaded on the support material prepared by the aforementioned catalyst synthesis procedure.

2.11.5 Calcination

The calcination is used to activate the catalyst at high temperatures in the presence of oxygen/airflow. The impurities from the metal salt precursor (anions, nitrates, chlorides) and additives from the catalyst synthesis is decomposed and removed. The calcination parameter such as temperature, heating rate and time influences the structure, surface area and final property of the calcined catalyst. The high calcination temperature can lead to sintering of loaded metal, thereby, decreasing the active metal species over the catalyst. Additionally, the catalyst is stabilized by performing calcination at a higher temperature compared to the experimental reaction condition. This prevents the catalyst from unnecessary surface reconstruction, mechanical instability apart from the influence of the reaction condition during the experiment [173].

2.11.6 Reduction

The reduction is a crucial step when the required oxidation state of the metal species is higher in the calcined catalyst than required for the desired experiment. Therefore, in many cases, the calcined catalyst is reduced in a reactive atmosphere such as hydrogen. Similar to calcination, the temperature, heating rate and calcination is crucial for the final performance of the catalyst [173].

2.12 Characterization

2.12.1 Surface area and the pore system - N_2 adsorption

The exposure of the catalytic surface on the incoming reactant molecules is an influential factor in determining the activity of the catalyst. Therefore, the higher surface area can minimize the amount of catalyst used in a chemical reaction. However, the high surface area does not necessarily correspond to high catalytic activity, if the pore structure is not uniformly distributed over the catalytic surface. Hence, catalytic activity is interdependent with the pore size and pore volume together with the surface area, which affects the molecular transportation and reaction pathway. The surface area of a solid catalyst is found by the physisorption of an inert gas such as nitrogen and argon. The number of inert gas molecules adsorbed over the solid material depends on the equilibrium pressure p, the temperature and the nature of gas-solid interaction. An adsorption isotherm of a solid material at constant temperature can be plotted using the equation (2.1), where n is

quantity of gas adsorbed, p is saturation pressure of the gas, p^o is equilibrium pressure and T temperature, respectively [174].

$$n = f(\frac{p}{p^o})_T \tag{2.1}$$

The IUPAC had defined the adsorption together with hysteresis loops, as shown in figure 2.22. The hysteresis loop arises due to adsorption-desorption behaviour from the pore and its connectivity with the pore network in the solid system. The Type I isotherm are commonly found in zeolites and activated carbons which is microporous in nature. Herein, the quantity of gas physisorbed is exclusively dependent on the accessible micropore volume rather on the internal surface area. The high uptake at low $\frac{p}{p^o}$ is due to the strong gas-solid interaction, which leads to micropore filling and multilayer adsorption is limited to exposed external surface area. This is generally associated with hysteresis loop 4 (H4) due to narrow silt-like nanopores.

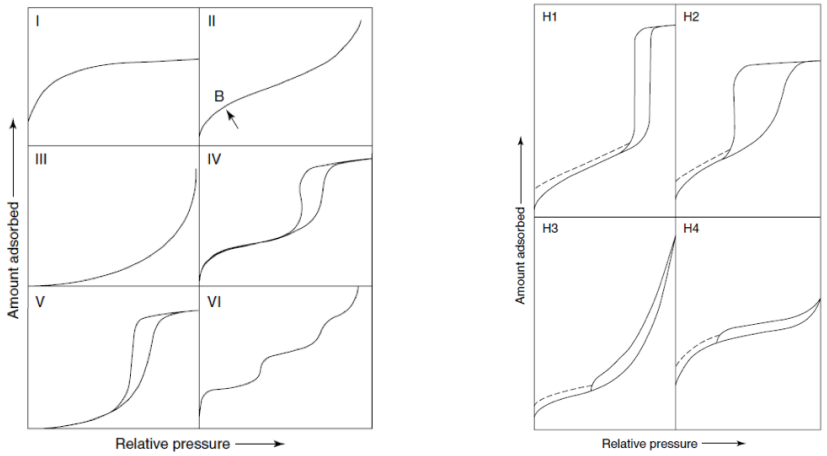

Figure 2.22: Physisorption isotherms (left side and the hysteresis loops (right side) proposed by IUPAC [171]

The macroporous or non-porous adsorbents exhibit Type II isotherm. This is a consequence of unrestricted monolayer-multilayer adsorption even at high relative partial pressure. Point B shares information on the complexity in the monolayer coverage. The distinct B shows the formation of the monolayer, whereas a gradual B shows no insights on the establishment of a monolayer, as observed from Type III isotherm. The Type III isotherms is a result of weak gas-solid interaction, and cluster formation of adsorbed molecules is favoured.

The Type IV isotherm majorly differs from previous isotherms on non-reversible nature of the adsorption and desorption pathways. The mesoporosity of the oxide gel gener-

ates Type IV isotherm. Herein, the capillary condensation is followed after the monolayer-multilayer adsorption. The hysteresis loop 1 and 2 are commonly associated with these type of materials. The former is related to a narrow range of uniform pores, whereas the latter is due to the complexity of pore networks.

The Type V isotherm follows the same weak interaction observed in Type III isotherm, whereas the molecules form clusters, and nanopore filling is observed at high relative pressure. Examples include activated carbon. The Type VI isotherms are observed when the solids exhibit surface uniformity, thereby layer-by-layer adsorptions is preferred. The quantity of the adsorbed layer is represented by the step height. However, the nature of the gas temperature decides the sharpness of the step.

The Brunauer-Emmett-Teller method (BET) is a commonly used method to estimate the surface area of a different catalyst either supported or unsupported. However, materials with low surface area (< 2 m^2/g) are not recommended to rely on BET estimated surface area. The BET surface area is found by the following two steps: Firstly, the BET plot is obtained from the physisorption isotherm. Secondly, deduction of the monolayer capacity of the adsorbate and calculating the BET surface area using the cross-sectional area of the adsorbed nitrogen molecule (nitrogen occupies 0.162 nm^2 at 77 K). Equation (2.2) shows the BET equation, where P is the applied pressure, P_o is saturation pressure of inert gas, V_a is total volume adsorbed at various P values, V_o is the first monolayer volume, χ is a constant related to the heat of adsorption. It is assumed that, at $\frac{P}{P_o}$ = 1, the multiplayer corresponds to infinite thickness. The linear dependency of $\frac{P}{Va(P_o-P)}$ and $\frac{P}{P_o}$ could be seen from figure 2.23. The preferred range for building BET plot is between 0.05-3 relative pressure for its decent linearity. The final value denotes the complete monolayer formation on the adsorbate.

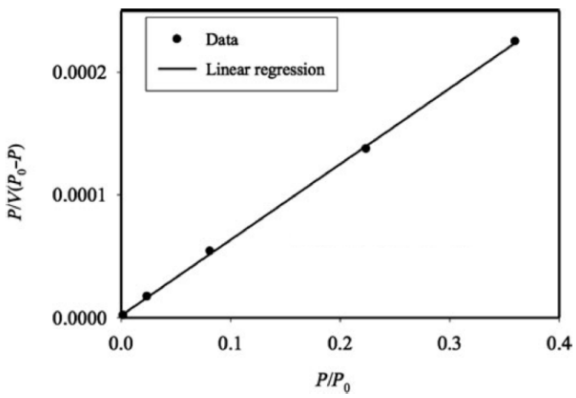

Figure 2.23: Linear BET plot [174]

$$\frac{P}{Va(P_o - P)} = \frac{1}{\chi V_o} + \frac{\chi - 1}{\chi V_o}\frac{P}{P_o} = \eta + \alpha\frac{P}{P_o} \tag{2.2}$$

The gas molecules condense at high pressure due to the multilayer formation inside the pore. This phenomenon is known as capillary condensation, which is reported to occur at lower pressure compared to the saturation pressure of the adsorbate gas molecules. The pore volume and pore size distribution can be deduced by utilizing the Barrett-Joyner-Halenda (BJH) method, which is based on the modified Kelvin equation. One has to remember that this method assumes that multilayer is unwinded slowly at a step-wise reduction of $\frac{p_o}{p}$. The modified equation is represented in equation (2.3), where r_p, γ, v_1 and R is the radius of the cylindrical pore, the surface tension of the condensate, molar volume of the condensate and gas constant, respectively. The summation of the Kelvin radius and thickness of the multilayer film is used to calculate the radius of the pores present in the catalyst.

$$r_p = -\frac{2\gamma v_1}{RT} ln \frac{P}{P_o} \tag{2.3}$$

2.12.2 X-Ray diffraction

X-ray Diffraction (XRD) is a powerful technique to characterize the crystallinity of the sample and crystallite size. Cathode ray tube generates the required X-rays and a filter which is placed before the sample produces monochromatic radiation. The detector records the diffracted waves. The intensity of the peaks in diffractogram corresponds to the abundance of the particular crystal phase, and the peak width is inversely proportional to the crystallite size.

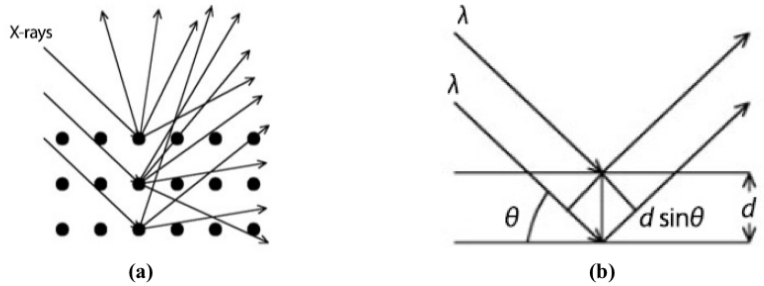

Figure 2.24: X-rays characterization: (a) Incident X-rays on the crystal plane, (b) Brag diffraction [174]

The X-ray utilized is in the range of inter-atomic distance of the crystal lattice (0.1 -100 Å). The X-ray approaching the crystal lattice either gets deflected or remain on the same path, as shown in figure 2.24 (a). The diffracted wave gets interfered constructively and is governed by Bragg's law, as shown in figure 2.24 (b). The Bragg's law states that when the angle of incidence (θ) of X-ray is equal to the angle of scattering (θ), constructive

interference occurs when the distance between two crystal planes (d) is equal to a whole number (n) of wavelength (λ), as shown in equation (2.4).

$$n\lambda = 2d\sin\theta \quad where \;\; n = 1, 2, 3.. \tag{2.4}$$

2.12.3 Temperature programmed desorption technique

The strength and distribution of acidic and basic sites on the catalytic surface also distinguish the performance of each catalyst in a chemical reaction. In this regards, the Temperature-Programmed-Desorption (TPD) technique is a straightforward technique, which analyze the aforementioned properties of the catalysts. Herein, the solid samples are commonly probed with a small gas molecule such as NH_3 and CO_2 due to its feasible diffusion through the different pore structure. The NH_3 is used for acidic measurement, whereas the CO_2 is utilized in basicity measurement. The TPD instrumentation is illustrated in figure 2.25. The pre-treatment of the sample is performed under vacuum prior probing with desired gas. Later, the probe gas is passed over the solid catalyst in excess, and weakly physisorbed molecules are removed by purging. Finally, the probe gas, which is in direct contact with the catalyst surface, is desorbed by a controlled heating rate. The desorbed species is monitored by flame ionization detector, thermal conductivity detector, mass spectrometer and conductometric titration.

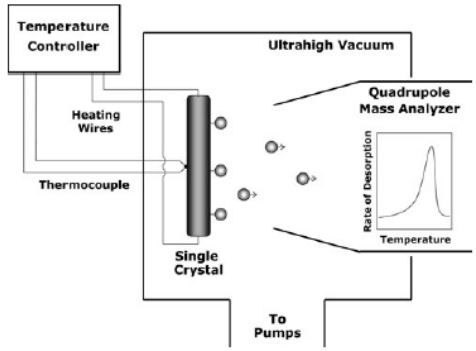

Figure 2.25: Temperature programmed desorption method [174]

The surface of the catalyst consisting of different hydroxyl (OH) groups corresponding to different strength of acidity, as shown in figure 2.26 (a). The simple and bridge hydroxyl are weak and moderate acidic sites, whereas the third type of hydroxyl configuration is strongly acidic. Similar to NH_3-TPD, the CO_2-TPD utilizes different forms of oxygen present on the catalyst as shown in figure 2.26 (b). The simple oxygen and ionic oxide represent weak and moderate basic sites, whereas the strong basicity is given by the anionic lattice oxygen present in the catalyst material.

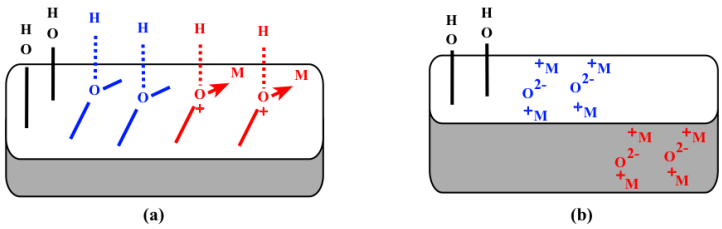

Figure 2.26: Surface acidity and basicity of catalyst (a) Acidic sites [black = simple hydroxyl, blue = bridging hydroxyl, red = hydroxyl bonded to bonded and coordinated to metal center] (b) Basic sites [black = simple hydroxyl, blue =ionic oxide on the surface, red =ionic oxide in the bulk material]

The TPD desorption profile gives two critical characteristics of the catalyst surface while utilizing NH_3 or CO_2. Firstly, the area under the curve is proportional to the quantity of gas adsorbed on the catalyst. Secondly, the position of peak describes the activation energy needed for desorbing the probed molecules. A higher activation will shift the location of the peak towards higher temperature in the TPD profile.

2.12.4 Scanning electron microscope

The morphology, chemical composition of the catalyst can be analyzed by electron microscopy. Herein, the electron has a wavelength in the range of 1 Å, which provides the image at atomic resolution. The primary electron beam interacts with the sample in many different ways, as shown in figure 2.27.

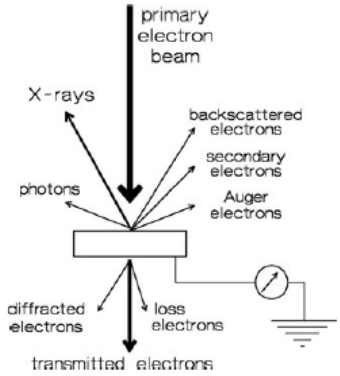

Figure 2.27: Different signals originating from the sample irradiated with primary electron beam [174]

The electron beams can get transmitted, diffracted or eject secondary electrons from the sample surface and so on [174]. The secondary electrons originate from the surface of the catalyst and characterized by low energy (about 550 eV) whereas the back-scattered

electron is generated from deep inside the solid catalyst which provides information on the chemical composition of the catalyst. The image contrast of the SEM images arises from the different orientation of the catalyst surface with respect to detector. The parts facing the detector are brighter compared to other parts of the catalyst surface.

There exist many different ways to calculate the mean particle size. These include volume average, surface average, geometric average and number average. The most common practice is to use the number average size method. However, depending on the nature of the particle size distribution, other methods are preferred as well. For example, the mean particle size based on the number average size gives a smaller value compared to average surface or average volume. The number average size is shown in equation 2.5, where d_i and n_i represent the diameter and number of particles, respectively.

$$\frac{\sum_{n=i}^{\infty} n_i d_i}{\sum_{n=i}^{\infty} n i} \tag{2.5}$$

2.13 GC-FID/TCD

The gas chromatography instrument comprises of mobile phase (inert gas) and stationary phase (coated inner walls of the capillary column). The injection can be a gas or liquid sample. In regards to liquid, the sample is volatilized. The carrier gas carries this gaseous sample/volatilized liquid sample through the GC column. The individual chemical components present in the gaseous mixture separate and reach detector depending on the boiling point and interaction with the stationary phase of the capillary column.

The commonly used detectors in the gas analysis are Thermal Conductive Detector (TCD) and Flame Ionization Detector (FID). The former utilizes the different specific heat capacity of the chemical components, thereby the different cooling rate of TCD (electrically heated) wires is observed. The concentration of the chemical species is proportional to the reduction in the electric signal transmitted through the TCD wires. The chemical gases like CO, N_2, H_2, CO_2, CH_4 is analyzed by TCD detector. The principle behind the latter detector is the formation of ions by breaking down the chemical structure of the organic compound. This is accomplished by the flame generated by hydrogen. The generated ions are collected at the electrodes, and the generated signal corresponds to the concentration of ions. Chemical species such as CH_4, alkanes and alkenes of C2-C6 hydrocarbons are detected with FID detector. It is to be noted that FID cannot detect H_2O, CO, CO_2.

The bio-oil analysis in GC utilizes, mass Spectrometer and flame ionization detector. The working principle of MS is based on fragmentation intensity produced during the ionization of organic compounds. The major difference between the MS and FID detector is that the latter utilizes the current produced by ions from the breakdown of the organic compound by H_2 flame. In short, the MS works on measuring the mass/charge ratio of the ionized chemical compounds.

Chapter 3

Materials and methods

This chapter describes preparation of catalyst, chemicals precursors, and procedures followed in all the characterization instruments reported in this work.

3.1 Preparation of catalyst

The TiO_2 powder (P-25), copper (II) nitrate hemi(pentahydrate) ($Cu(NO_3)_2 \cdot 2.5\,H_2O$), Gdld (III) chloride trihydrate ($HAuCl_4{\cdot}3H_2O$), 5 wt.% Ru/ activated carbon, ammonium phosphate dibasic ($(NH_4)_2HPO_4$), iron nitrate nonanhydrate ($FeNO_3{\cdot}9H_2O$), ammonium molybdate tetrahydrate ($(NH_4)_6Mo_7O_{24} \cdot 4\,H_2O$), ruthenium chloride ($RuCl_3$), citric acid ($C_6H_8O_7$), and γ-alumina powder (γ-Al_2O_3) with $\geq$ 99 purity was used as received from Sigma Aldrich without any chemical treatment for catalyst preparation.

3.1.1 Incipient wetness impregnation

In this work, TiO_2 is used as a support material. The pore volume of TiO_2 was identified by slowly dripping deionized water into 1 g of the support. The volume of water is noted until the support is completely wet without any phase separation between the support and water. The water necessary to prepare the various catalyst is listed in table B.1 (Appendix). The calculated quantity of water was used to prepare the solution by dissolving required chemical precursor of Cu at room temperature with continuous stirring. Similarly, gold and ruthenium metal precursor solution were prepared. Finally, the solution was added dropwise on to the support material. The catalyst was dried overnight inside fume wood. Later, the dried catalyst was calcined at 400°C in 40 ml/min air for 4 hours. The calcined catalyst was further reduced at 350°C in 10 ml/min H_2 flow for 3 hours. Total of 6 catalysts, each 7 grams was prepared which includes 0.5, 1, 3, 7 wt.% of Cu, 1 wt.% Au, and 1 wt.% Ru loaded over TiO_2 support.

3.1.2 Wet impregnation

A sequential wetness impregnation was used to prepare 16 grams MoFeP/Al_2O_3. The metal precursor (1:1:1 molar ration of Mo:Fe:P) Fe (14.13 g), Mo (6.22 g) and P (4.5198 g) were taken to represent 27 wt.% of active metal loading over the alumina support. The chemical precursor was dissolved stepwise in 1 M citric solution of 30 ml with continuous stirring. The citric acid prevents active metals from precipitation. The alumina powder was added slowly after a homogeneous solution was visible. The catalyst was dried overnight in the fume hood at room temperature and dried in the oven at 100°C for 7 hours. The catalyst is subjected to calcination at 400°C (10 °C/min heating rate) for 6 hours in 40 ml/min O_2 flow. 1 wt.% of Ru was promoted over the calcined MoFeP/Al_2O_3 using incipient wetness impregnation method. The 1 wt.% Ru-MoFeP/Al_2O_3 catalyst was dried at room temperature in fume hood and calcined at 500°C (10 °C/min heating rate) for 4 hours at 40 ml/min O_2 flow. The promoted catalyst was reduced at 400°C (10 °C/min heating rate) for 4 hours at 10 ml/min H_2 flow.

3.1.3 Depositional precipitation

The depositional precipitation is a controlled precipitation method for loading the active metal species inside the pores of the catalyst. 7 grams of 1 wt.% Au/ TiO_2 catalyst was prepared. Herein, urea solution of 0.3 M was prepared by mixing 6 grams of urea in 350 ml of deionized water. The TiO_2 and gold precursor were dissolved, and the suspension was heated in an oil bath at 75°C for 4 hours which led to slow decomposition of urea. The slow increase in pH slowly deposited the gold species on to the TiO_2 support. The solid catalyst was recovered by using filter paper, and the catalyst was washed three times with deionized water to remove traces of chlorine residue [175]. The catalyst was dried overnight in a fume hood at room temperature. The catalyst was calcined at 400°C (10 °C/min heating rate) for 4 hours in O_2 flow of 40 ml/min. The catalyst was further reduced at 350°C (10 °C/min heating rate) in H_2 flow of 10 ml/min for 4 hours. The catalyst was placed in a glass vial and covered with aluminium foil to avoid oxidation of gold species due to the ambient atmosphere.

3.1.4 Physical mixture

A physical mixture of Ru/C and TiO_2 were prepared in which Ru loading accounted 1 wt.% of the total catalyst. 7 grams of catalyst was prepared by mixing 1.4 grams of 5wt.% Ru/C and 5.6 grams of untreated TiO_2. The catalyst was not calcined or reduced in oxygen, hydrogen flow, respectively.

3.2 Characterization

3.2.1 Scanning electron microscope

The surface morphology, elemental composition and homogeneity of the chemical species were studied by scanning electron microscope. Hitachi S5500 scanning Transmission

Electron Microscope (S(T)EM) was equipped with Bruker XFlash energy-dispersive-X-ray (EDX) detector for SEM imaging. The S(T)EM was operated at acceleration voltage pf 30kV to capture all the surface morphology of the catalyst.

3.2.2 X-ray diffraction

X-ray Diffraction (XRD) was performed using D8-Focus instrument. The XRD patterns were developed using CuK radiation. The 2θ value varied from 5° to 75° with a step size of 0.2°. All the XRD diffractorams were analyzed using DIFFRAC.EVA software.

3.2.3 Surface area and the pore system- N_2 adsorption

Micromeritics TriStar II 3020 was used to perform N_2 adsorption-desorption at 77 K. The sample was degassed at 150°C under vacuum overnight in Micromeritics VacPrep 061. Brunuer-Emmett-Teller (BET) method was used to estimate the specific surface area of the samples. The chosen relative pressure for calculation of BET surface was in the range of 0.05-0.3. The Barrett-Joyner-Halenda (BJH) method was utilized to calculate the pore size distribution and the pore volume.

3.2.4 Temperature programmed desorption technique

NH_3-temperature programmed desorption was performed using Micromeritics Auto Chem II 2920. 5% NH_3 in helium gas was used as a probe molecule. The required quantity of sample is loaded into the adsorption vessel and consecutively evacuated under helium flow at 150°C for 2 hours. The sample is saturated with 5 % NH_3 after cooling down to 100°C. The physisorbed NH_3 is flushed using helium for 1 hour. The desorption of the chemisorbed NH_3 occurs by increasing the temperature from 100 to 700°C at a heating rate of 10 °C/min under helium flow. The quantity of chemisorbed ammonia is corrected via a calibration curve made for varying volumes of ammonia in helium. The total acidity was calculated using Chem Master software.

CO_2-temperature programmed desorption was also conducted in Micromeritics Auto Chem II 2920. 10% CO_2 in helium was used as a probe molecule. The required sample is loaded into the adsorption vessel and degassed at 150°C for 2 hours in helium flow. 10% CO_2 in helium flow saturated the surface of the sample for 30 min. The physisorbed CO_2 is flushed using helium gas for 30 min. The temperature is increased from 40 to 550°C at 10 °C/min under helium flow to desorbed the chemisorbed CO_2 molecule. The quantity of CO_2 molecule is corrected using the calibration table with the varying volume of CO_2 in helium. The total basicity was calculated using Chem Master software.

3.2.5 Two-stage fixed-bed reactor

The non-catalytic hydropyrolysis and non-catalytic hydropyrolysis followed by ex-situ catalytic up-gradation was conducted in two consecutive fixed-bed reactor placed in series configuration. The non-catalytic hydropyrolysis was conducted in 1^{st} reactor at 540-600°C (15 °C/min heating rate) and 1 bar. The ex-situ up-gradation of non-catalytic hydropyrolysis derived biomass oxygenates was accomplished in 2^{nd} fixed-bed reactor at

350°C (15°C/min heating rate) and 1 bar. The catalyst is placed at isothermal region of the 2^{nd} (middle zone). Herein, nitrogen and hydrogen gas was flown in to the 2^{nd} reactor through the 1^{st} reactor. Total flow rate of 30 ml/min and 100 ml/min was tested, Of which N_2 represents 20% of the total flow rate. The biomass to catalyst ratio was fixed at 2. The Weight Hourly Space Velocity (WHSV) during ex-situ catalytic up-gradation was 0.96 h^{-1}, which is calculated based on equation (3.1). The bio-oil and gaseous products is condensed and collected in a glass condenser and gas bag, respectively.

$$WHSV = \frac{Total\ mass\ flow\ feed\ rate}{Total\ catalyst\ weight}(h^{-1}) \tag{3.1}$$

3.2.6 Gas analysis: Gas Chromatography/Thermal Conductivity Detector (TCD)/ Flame Ionization Detector (FID)

The gas chromatographer (Agilent 7820A) was used to calibrate the gaseous compounds which are equipped with a FID and TCD detector. An Agilent HP-PLOT Al_2O_3 KCl Column (50 m × 0.530 mm × 0.15 µm) was used GC instrument. A gas cylinder containing known mole percentage of CO_2, CO, N_2, H_2, CH_4, ethane, ethene, propane, propene, butane, butene, pentane and pentene is passed through the GC column for calibration. The mole percentage of each species is listed in table C.1 (Appendix). The helium gas was used as a carrier gas in GC column with a flow rate of 35 ml/min and a split ratio of 25:1. The GC oven temperature is kept at 45°C for 6 minutes. The temperature is raised up to 190°C at 75 °C/min heating rate and held for 2 minutes. The oven temperature is brought back to 45°C. The FID and TCD detector temperature is set to 250 and 230°C. The flow of hydrogen, air and makeup helium gas was used in the FID heater which is set to 350, 35 and 25 ml/min. Similarly, helium flow of 45 and 2 ml/min was used as a reference and makeup gas in the TCD heater. Table 3.1, 3.2 shows the response factor obtained from the one-point calibration from the aforementioned gas components in the cylinder.

Gas compound (TCD detector)	**Response factor**
Nitrogen	1.71×10^{-3}
Hydrogen	2.60×10^{-2}
Carbon dioxide	1.54×10^{-3}
Carbon monoxide	1.83×10^{-3}

Table 3.1: Response factor of gases detected from TCD detector

The nitrogen gas was used as an internal standard for gaseous product quantification from TCD detector. The molar flow of gas detected from the experiment is quantified using the equation (3.2), where F_i, F_{N_2}, f_i, f_{N_2}, A_i, A_{N_2} represents the molar flow of compound i, molar flow of nitrogen, response factor of compound i, response factor of nitrogen and TCD peak area of compound i, and TCD peak area of N_2. Mass of the gas compound was calculated using (3.3) where m_i, M_i and F_i represents the molecular mass, mass and molar flow of compound i.

$$F_i(mol/h) = \frac{f_i}{f_{\mathrm{N_2}}} \cdot \frac{A_i}{A_{\mathrm{N_2}}}(mole/h) \cdot F_{\mathrm{N_2}(mol/h)} \tag{3.2}$$

$$m_i = F_i \cdot M_i \tag{3.3}$$

The gaseous products detected in the FID detector is quantified using methane as an internal standard. The methane was observed to be detected in both TCD and FID detectors. Therefore, the mass of methane gas was calculated from the previous calculation using nitrogen as an internal standard. Later, methane gas was used as a reference gas in quantification of products detected from FID detector using equation (3.4), where F_i, $\mathrm{F}_{\mathrm{CH_4}}$, f_i, $\mathrm{f}_{\mathrm{CH_4}}$, A_i, $\mathrm{A}_{\mathrm{CH_4}}$ represents the molar flow of compound i, molar flow of methane, response factor of compound i, response factor of methane and FID peak area of compound i and methane, respectively. The mass of gas compound is similarly calculated from the equation (3.3).

$$F_i(mol/h) = \frac{f_i}{f_{\mathrm{CH_4}}} \cdot \frac{A_i}{A_{\mathrm{CH_4}}}(mole/h) \tag{3.4}$$

Gas compound (FID detector)	**Response factor**
Methane	1.15×10^{-3}
Ethane	6.03×10^{-4}
Ethene	6.04×10^{-4}
Propane	3.84×10^{-4}
Propene	3.93×10^{-4}
Butane	2.92×10^{-4}
Pentane	2.36×10^{-4}
Hexane	7.66×10^{-3}

Table 3.2: Response factor of gases detected from FID detector

3.2.7 Liquid analysis: Gas Chromatography/ Flame Ionization Detector (FID)/Mass Spectrometry detector

A GC/FID (Agilent 7820A) and a GC/MS (GC-Agilent 7820A, MS-5977E) were used for analysis of bio-oil obtained in the two-stage fixed bed reactor, respectively. The primary requirement in both GC instrument is the same capillary column and instrument analysis procedure to maintain a similar peak distribution throughout the GC chromatogram. An Agilent JW HP-5 GC Column (30 m × 0.320 mm ×0.25 µm) was used in both GC instrument. The GC heating program starts with initial temperature of 40°C for hold time of 2 minutes. Later, the heating rate of 4°C is set to reach 270°C and stays for 2 minutes. The

helium was used as a carrier gas with flow rate of 1 and 2 ml/min in GC-MS and GC-FID, respectively. Additionally, the sample depth for sample suction using microsyringe was set to -1 due to low quantity of bio-oil in the GC vials C.1 (Appendix). The chemical components were identified by the scientific library NIST11.L in GC-MS whereas quantification was accomplished by the GC-FID.

The sensitivity of the FID detector inside the GC instruments varies with different chemical compounds. Therefore, an external standards was used to quantify different bio-oil components. Herein, 0.5 ml of cyclohexane is mixed with 0.1, 0.25, 0.5 and 1 ml of standard chemicals and subsequently analyed in the GC-FID. A linear graph is plotted between relative peak area of standard chemical to its corresponding concentration in the mixture, as shown in figure C.2 (Appendix). Limited number of response factor of chemical compounds were calculated due to availability of standard chemicals which represents the bio-oil. The response factor of acetone, toulene, propanol, ethyl acetate, tetrahydrofuran, phenol and furfural is shown in table C.2 (Appendix).

In literature, the common practise to quantify chemical components of bio-oil is by external standard calibration. For example, Chandler et al. used a total of 48 response factor associated with corresponding bio-oil components in GC analysis. Additionally, the compounds with a similar chemical structure are assumed to have the same response factor [37]. However, herein, this strategy could not be performed due to the limited availability of standard chemical commonly found in bio-oil. yet, the response factor for toluene, propanol, ethyl acetate, tetrahydrofuran, phenol, furfural, and acetone was calibrated utilizing cyclohexane as an external standard as previously mentioned. Unfortunately, an assumption of response factor for the bio-components based on the standard chemicals listed in table C.2 (Appendix) led to the poor mass balance of the total biomass input. Therefore, FID peak area is used to quantify the bio-oil components in this work.

Chapter 4

Results & Discussion

4.1 Characterization

4.1.1 Scanning electron microscope

Scanning Electron Microscope (SEM) and Energy-Dispersive X-ray (EDX) mapping confirmed the morphology, distribution and the presence of Cu, Ru, Au, Mo, Fe and P loading. The white colour of the TiO_2 particles changed from light to dark navy blue depending upon the copper loading [176]. In contrast, the Ru loading turned TiO_2 from white to grey color, whereas Au loading gave violet appearance to TiO_2 particles. The final colour of the ruthenium promoted MoFeP/Al_2O_3 was dark black.

The SEM images were obtained at the same magnification to direct comparison between the fabricated catalyst. Figure 4.1 (a-i) shows the SEM images of the catalyst prepared for carbon-carbon coupling and hydrodeoxygenation reaction. The aggregation of spherical TiO_2 particles is observed in all titania-based catalyst including, the bare TiO_2 support [177]. The bare support particle, as shown in 4.1 (a) were $\approx$ 22 nm. The SEM images of copper loading at 0.5, 1 and 3 wt% on TiO_2, shown in figure 4.1 (b), (c) and (d) were similar to unmodified P-25-TiO_2. The copper nanoparticle could only be visible at high copper loading of 7 wt%, as shown in figure 4.1 (e). Similar observation were reported at high loading of copper (13%) over TiO_2 [178]. This might be due to overloading of copper metal species on the surface of TiO_2. Moreover, the particle size distribution of copper metal varied from 50 to 100 nm. Similar to the low loading of copper on titanium oxide, no visible ruthenium or gold nanoparticles were observed, as shown in figure 4.1 (f) and (g). Figure 4.1 (h) and 2 (i) show the SEM images of the physical mixture of commercial Ru/C + TiO2 and 1 wt% Ru-MoFeP/Al_2O_3. The former is observed to contain both spherical TiO_2 spherical nanoparticles and plate-like structure for Ru/C, as indicated in figure 4.1 (h). On the other hand, the later consisted of random structural morphology of Mo, Fe and phosphate species. However, the alumina spheres, which is acting as a support material, is still clearly visible.

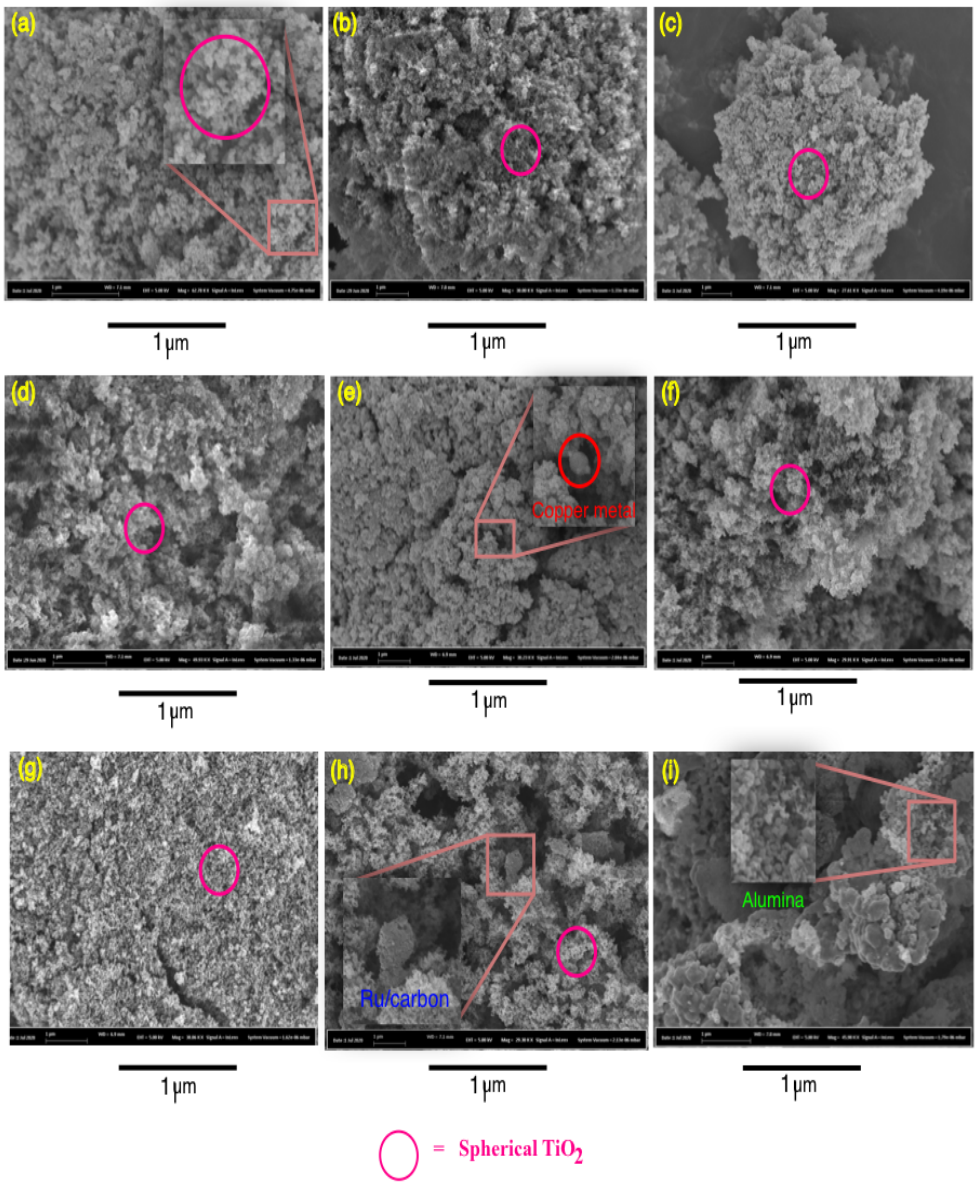

Figure 4.1: SEM images: (a) Untreated TiO_2, (b) 0.5 wt% Cu/TiO_2, (c) 1 wt% Cu/TiO_2, (d) 3 wt% Cu/TiO_2, (e) 7 wt% Cu/TiO_2, (f) 1 wt% Ru/TiO_2, (e) 1 wt% Au/TiO_2, and (f) 1 wt% $Ru/MoFeP/Al_2O_3$

The EDX and elemental mapping were utilized to confirm the presence and the distribution of Cu, Ru, Au, Mo, Fe and P on the support surface of TiO_2 and γ-Al_2O_3, as shown in figure 4.2 (a-h). Figure 4.2 (a-d) shows the presence of copper on TiO_2. The abundance of copper could be clearly visible at loading $\geq$ 3 wt%. Similar to the low load-

ing of copper, 1wt.% of gold and ruthenium on TiO_2 shows a small peak in figure 4.2 (e) and (f) respectively. However, the presence of chlorine was found in 1 wt.% Ru/TiO_2. This is due to the chlorine residue from the precursor salt ($Rucl_3$) of the ruthenium metal during catalyst synthesis. In the case of a physical mixture of Ru/C + TiO_2 and 1 wt% Ru promoted MoFeP/ Al_2O_3, all the peaks were clearly distinct and visible except Ru in the latter due to its relatively low loading compared to other elements of the catalyst.

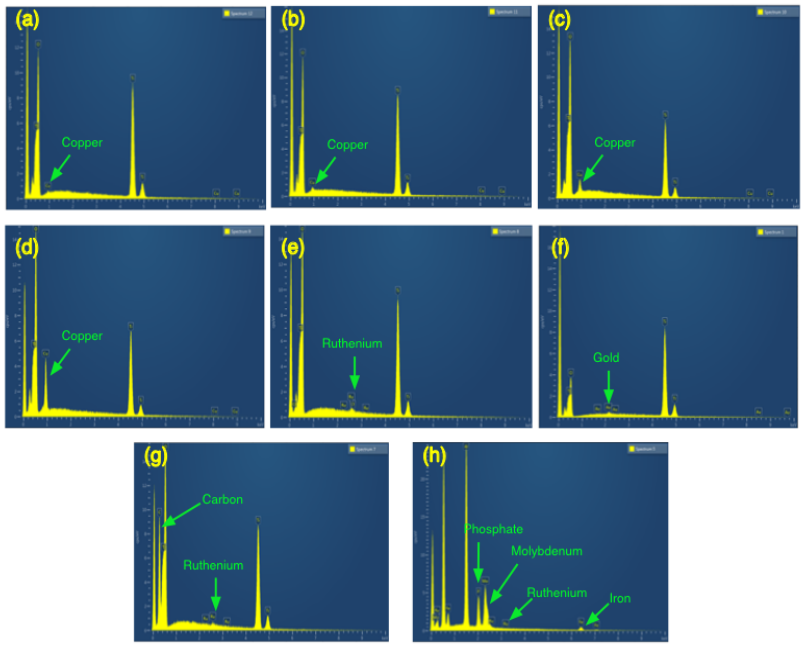

Figure 4.2: Presence of chemical element via EDX: (a) 0.5 wt% Cu/TiO_2, (b) 1 wt% Cu/TiO_2, (c) 3 wt% Cu/TiO_2, (d) 7 wt% Cu/TiO_2, (e) 1 wt% Ru/TiO_2, (f) 1 wt% Au/TiO_2, and (g) 1 wt% $Ru/MoFeP/Al_2O_3$

The elemental mapping of the fabricated catalyst provides insights into the distribution of the loaded metal over the support material. Figure 4.3 (a-f) shows the distribution of different loading of Cu, Au and Ru on TiO_2. It is evident that the aforementioned metals are homogeneously distributed over the catalytic surface in spite of low dopant concentration over TiO_2. The high loading (7 wt.%) of copper over TiO_2 could be easily observed from the high contrast image obtained in 4.3 (d) compared to 4.3 (a), (b), and (c). In the case of HDO catalyst 1 wt% Ru-$MoFeP/Al_2O_3$, the distribution showed observable variance among different elements of the catalyst. Figure 4.4 (a-e) shows the elemental mapping of Fe, Mo, Ru, P, and Al. Despite the low loading of Ru (1wt%), a satisfactory uniform distribution over the catalytic surface is observed. However, the homogeneity is less evident in the case of P and Fe compared to Mo. The latter is spread uniformly similar to ruthenium whereas the former is deposited more on the peripheral region of the alumina support material.

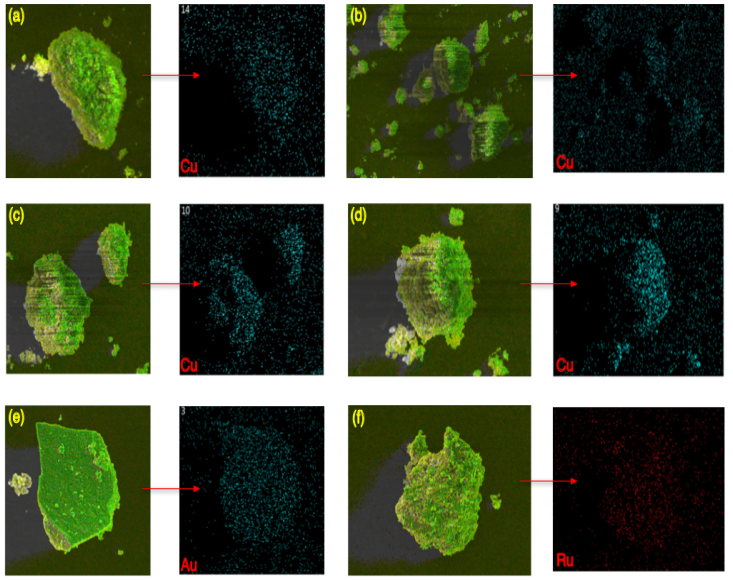

Figure 4.3: EDX images: (a) 0.5 wt% Cu/TiO_2, (b) 1 wt% Cu/TiO_2, (c) 3 wt% Cu/TiO_2, (d) 7 wt% Cu/TiO_2, (e) 1 wt% Au/TiO_2, and (f) 1 wt% Ru/TiO_2

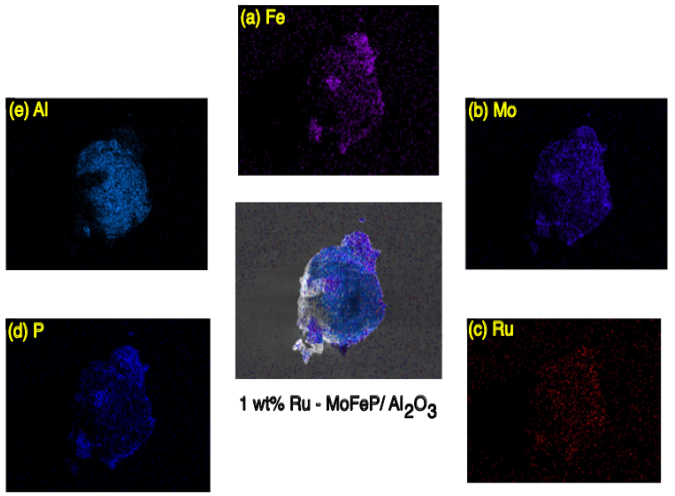

Figure 4.4: EDX images of 1 wt.% Ru-MoFeP/Al_2O_3

4.1.2 X-ray diffraction

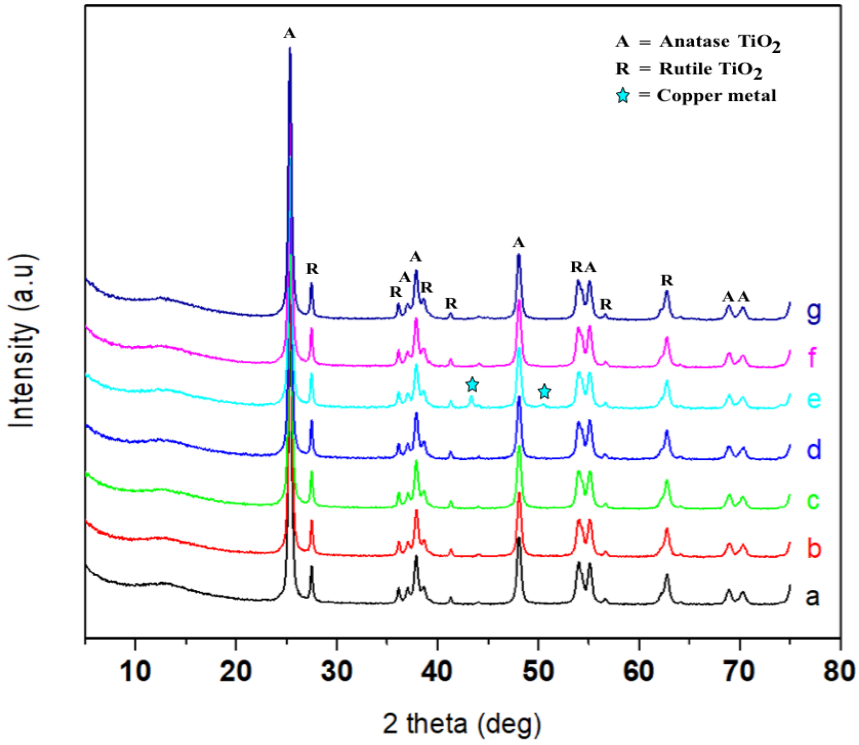

Figure 4.5: XRD diffractogram: (a) Untreated TiO_2 (b) 0.5 wt% Cu/TiO_2, (c) 1 wt% Cu/TiO_2, (d) 3 wt% Cu/TiO_2, (e) 7 wt% Cu/TiO_2, (f) 1 wt% Au/TiO_2, (g) 1 wt% Ru/TiO_2

XRD diffractogram of different fabricated metal loaded TiO_2 are depicted in figure 4.5. The diffractogram pattern of TiO_2 shows a mixture of rutile and anatase crystallite phases. The anatase and rutile TiO_2 peaks were visible at $2\theta \approx 25°$, 37°, 48°, 55°, 68°, 70°and 27°, 36°, 41°, 44°, 54°, 56°, 62°respectively. XRD diffractogram of metal loaded TiO_2 did not show any new crystalline peaks associated during catalytic preparation, calcination and reduction. It is evident from 4.5 (a), (b), (c), (d) and (g) that copper loading from 0.5-3 wt.% and 1wt.% Ru over TiO_2 shared the similar peaks associated with the bare TiO_2, which consist of 79% anatase and 21% of rutile phase. This suggest that copper and ruthenium species is uniformly dispersed over TiO_2 support, as supported by SEM images. However, high copper loading at $2\theta \approx 43°$showed an metallic copper peak which was also confirmed from the SEM images. It is evident that copper was observed to be in metallic state due to the reduction step in catalytic preparation. Similarly, the low of loading of copper based catalyst is suggested to be in metallic state rather than oxidized. Chiang et al. reported similar observation on copper loading on TiO_2. However, the author did not observed any peak associated with copper upto 10 wt.%. This is due to the difference in catalytic preparation method. Herein, incipient wetness impregnation method was approached whereas

the author used photo-deposition which led to uniform distribution of copper even at high loading [176]. In the case of gold loaded TiO_2, the diffractogram was similar to the low loading of copper metals. However, the peak associated with the metallic gold was observed to be overlapped with the anatase TiO_2 at $2\theta \approx 37°$and 63°. Unfortunately, gold clusters were not visible in SEM images.

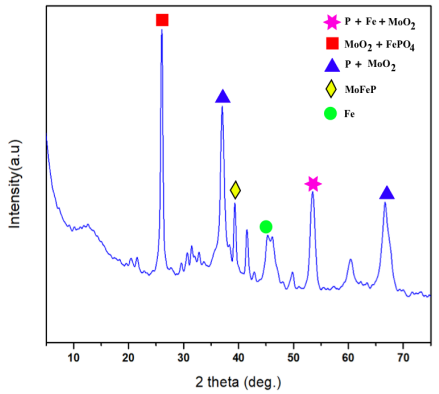

Figure 4.6: XRD diffractogram of 1 wt% Ru-MoFeP/Al_2O_3

Figure 4.6 shows the XRD pattern of the HDO catalyst; 1 wt% Ru-MoFeP/Al_2O_3. The overlapping between the various metallic species was observed. The pure metallic phosphorous and iron was observed whereas, the molybdenum was majorly present in oxide form (MoO_2). The peaks at $2\theta \approx 25°$ shows the overlapped crystallite phase of MoO_2 and Fe_2PO_4. The overlapped peaks at $2\theta \approx 37°$ and 66° shows the presence of metallic phosphorous and molybdenum oxide whereas, $2\theta \approx 53°$ represents P, Fe and MoO_2 phase. Pure metallic phosphorus was also observed at $2\theta \approx 45°$. The formation of MoFeP at $2\theta \approx 45°$ was evident from the XRD analysis. The overlapped region between Mo, Fe and P species in the SEM images support the formation of MoFeP phase over alumina. Similar to 1 wt% Ru/TiO_2, no visible peaks could be associated with Ru. Based on the results obtained from XRD, SEM and EDX studies, the presence of metallic Fe, MoO_2 and MoFeP phase is suggested to be homogeneously distributed over the catalyst except for phosphorus species.

4.1.3 Brunauer Emmett Teller method

The nitrogen adsorption-desorption isotherms of different metal loading on TiO_2, and HDO catalyst is shown in figure 4.7 and 4.8. All the metal loaded on TiO_2 support follows Type V isotherm with H3 hysteresis loop, as previously discussed in section 2.12.1. This shows the weak adsorbent-adsorbate interaction at relatively low partial pressure (p_0/p). Therefore, the monolayer formation could not be identified directly from the adsorption isotherm. At high p_o/p, the pore filling is observed with the creation of molecular clusters on favourable sites, which is observed from the hysteresis loop formation. The physical mixture of Ru/C and TiO_2 also posses similar adsorption isotherm behaviour of TiO_2

catalyst. The alumina-based catalyst posses similar Type V isotherm compared to TiO_2 catalyst. However, the complex pore structure led to H3 hysteresis loop compared to TiO_2-based catalyst.

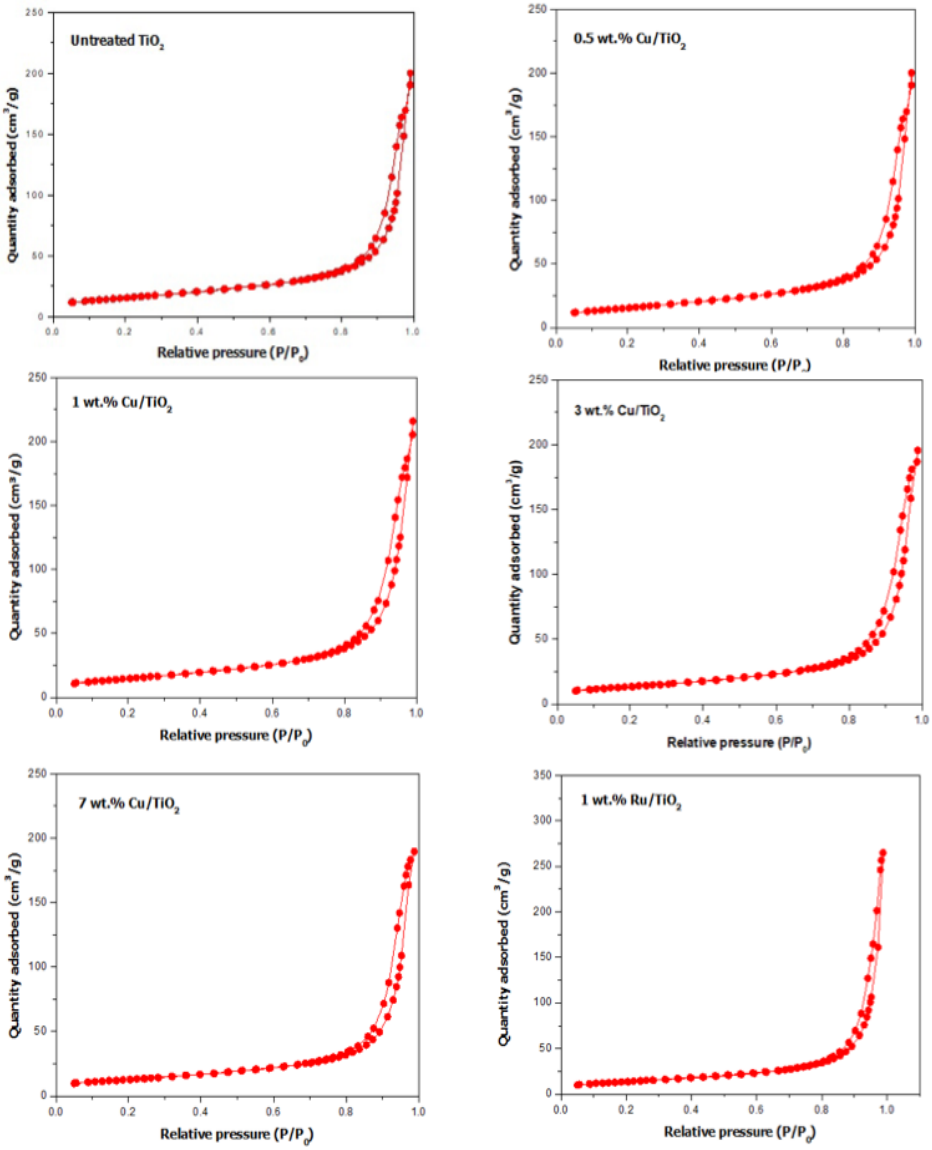

Figure 4.7: BET plots-I

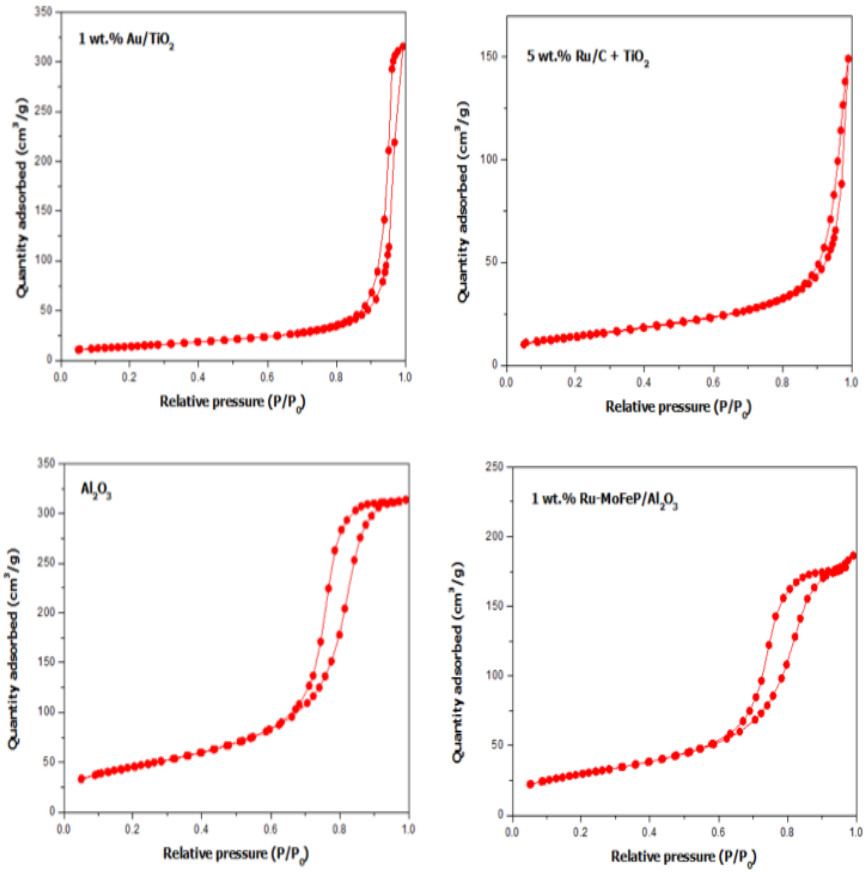

Figure 4.8: BET plots-II

The BET surface area, average pore diameter and pore volume obtained from the adsorption and desorption isotherm is listed in table 4.1. The BET surface area, average pore volume and pore diameter of the physical mixture of commercial Ru/C and TiO_2 is 739.37 m^2/g, 0.620 cm^3/g and 6 nm, respectively. The high surface area is attributed to the carbon support since pure TiO_2 is only $\approx$ 50 m^2/g. In the case of bare TiO_2, which is spherical non-porous in nature was observed to possess BET surface area, average pore volume and pore diameter of 56.95 m^2/g, 0.302 cm^3/g and 19.05 nm. However, these value changed when Cu, Au and Ru were dispersed over TiO_2 during catalyst preparation. The increment in the copper loading decreased the BET surface area from 56.95 to 45.73 m^2/g until 7wt.% copper loading. However, the loss in BET surface area was more prominent for 1wt.% Ru (49.60) and Au (50.30 m^2/g) compared to 1wt.% Cu (53.66 m^2/g) loading on TiO_2. With regards to 1 wt% Ru-MoFeP/Al_2O_3, the loading of Mo, Fe, P and Ru had clearly decreased the BET surface area of alumina from 164.63 to 105.99 m^2/g. This can be attributed to the pore filling by the dopants inside the intrinsic pore structure of titania and alumina support.

The BJH method wass utilized to obtain the data on the total pore volume and mean diameter of the catalyst. The mean pore diameter is observed to increase with the increase in copper loading (0.5 to 7wt.%) from 19.05 to 21.06 nm. Similarly, Ru (27.26 m^2/g) and Au (29.96 m^2/g) dopants increased the pore diameter compared to all copper-based catalyst. This effect might be due to the filling of dopants over the smaller pores present on the TiO_2 support, which resulted in averaging of larger pore diameter of TiO_2 catalyst. In contrast, the deposition of Ru, Mo, Fe, P over alumina led to a decrease in pore size from 7.92 to 7.83 nm. There are two possible scenarios to explain this behaviour. Firstly, the aggregation of smaller crystallites of alumina to form smaller pores. Secondly, the dopants might have deposited inside the porous structure of alumina [179].

An unusual trend is observed over total pore volume w.r.t to different metal loading. Initially, there is an increase in the pore volume of 0.310 cm^3/g and 0.334 cm^3/g for 0.5 wt.% and 1 wt.% Cu loading compared to bare TiO_2, respectively. Interestingly, the total pore volume decreases at 3 and 7 wt.% copper loading relative to the base support. Similar to low copper loading, increase in total pore volume is observed for Ru (0.410 cm^3/g) and Au (0.488 cm^3/g) loaded catalyst compare to all copper-based catalyst. The loading of multi metallic species over alumina showed the same behaviour observed at high copper loading over TiO_2. The total pore volume dropped from 0.487 to 0.290 cm^3/g. This might be due to pore filling effect of the dopants inside the pores of titania and alumina, as previously mentioned [179].

Catalyst	**Metal loading (wt.%)**	**BET surface area (m^2/g)**	**Pore volume (cm^3/g)**	**Pore diameter (nm)**
Cu/TiO_2	0.5	55.81	0.310	19.30
Cu/TiO_2	1	53.66	0.334	20.13
Cu/TiO_2	3	48.49	0.303	20.20
Cu/TiO_2	7	45.73	0.294	21.06
Ru/TiO_2	1	49.60	0.410	27.26
Au/TiO_2	1	50.30	0.488	29.96
Ru/C	1	739.37	0.620	6.00
Ru/C + TiO_2	b	739.37	0.620	6.00
Al_2O_3	a	164.63	0.487	7.92
Ru-MoFeP/Al_2O_3	1,27	105.99	0.290	7.83

Table 4.1: BET and BJH analysis of synthesized catalyst

4.1.4 Temperature programmed desorption

The strength and distribution of acid-base properties play a key role in C-C coupling and HDO reaction. The total acidity and basicity of the catalyst is listed in table 4.2. The various loading of copper over TiO_2 changed the distribution of weak and strong acid sites, as shown in figure 4.9. There was an uneven trend observed in the copper-based catalyst. The total acidity decreased in the order: 3 wt.% Cu/TiO_2 > 0.5 wt.% Cu/TiO_2 > 7 wt.%

$Cu/TiO_2 > 1$ wt.% Cu/TiO_2. Interestingly, higher copper loading at 3 wt.% and 7 wt.% led to clear distinction between weak and medium+strong acid sites at temperature $\approx 200°C$, 350°C, respectively. These changes shows insights on the unsaturated copper metal centers (Lewis acidity) and oxides (Brønsted acidity) distributed over the TiO_2. Among the titania supported catalyst, 1 wt.% Ru/TiO_2 showed the highest acidity and 1 wt.% Au/TiO_2 showed the lowest acidity. The HDO catalyst, ruthenium promoted $MoFeP/Al_2O_3$ posses total acidity of 0.365 mmol/g, which was higher than the C-C coupling catalyst. The weak acid sites was prevalent on HDO catalyst at temperature $\approx 200°C$.

Similar to an unusual trend for the acidity of copper-based catalyst, the total basicity decreased in the order: $>$ 7 wt.% $Cu/TiO_2 >$ 3 wt.% $Cu/TiO_2 >$ 0.5 wt.% Cu/TiO_2 $>$ 1 wt.% Cu/TiO_2. Similar to distribution of acid peaks of copper based catalyst, the higher copper loading led to visible separation between the weak and medium+strong basic sites peaks at 75°C and 250°C, as shown in figure 4.10. In contrast to high acidity, 1 wt.% Ru/TiO_2 showed the lowest total basicity compared to gold and copper based catalyst, as observed from table 4.2. There is no significant peak separation in ruthenium and gold based catalyst compared to 1 wt.% Cu/TiO_2. Interestingly, there was clear difference between the weak, medium and strong acidic peak distribution at 140°C, 250°C and 350°C, respectively in HDO catalyst compared to other catalyst. The total basicity of 0.353 mmol/g was highest for 1 wt.% Ru-$MoFeP/Al_2O_3$.

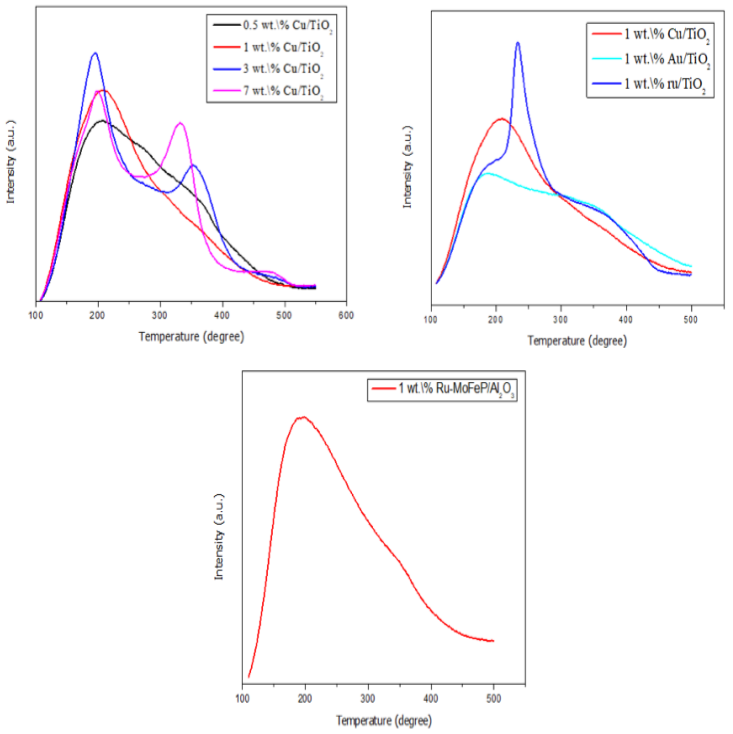

Figure 4.9: NH_3-Temperature programmed desorption plots

Catalyst	Loading (wt.\%)	Total acidity (mmol/g)	Total basicity (mmol/g)	Acid/base ratio
Cu/TiO_2	0.5	0.273	0.238	1.14
Cu/TiO_2	1	0.262	0.211	1.24
Cu/TiO_2	3	0.278	0.269	1.03
Cu/TiO_2	7	0.268	0.275	1.15
Au/TiO_2	1	0.239	0.218	1.10
Ru/TiO_2	1	0.280	0.192	1.46
$Ru\text{-}MoFeP/Al_2O_3$	1,20	0.365	0.353	1.03

Table 4.2: NH_3 and CO_2-TPD analysis of the C-C coupling and HDO catalyst

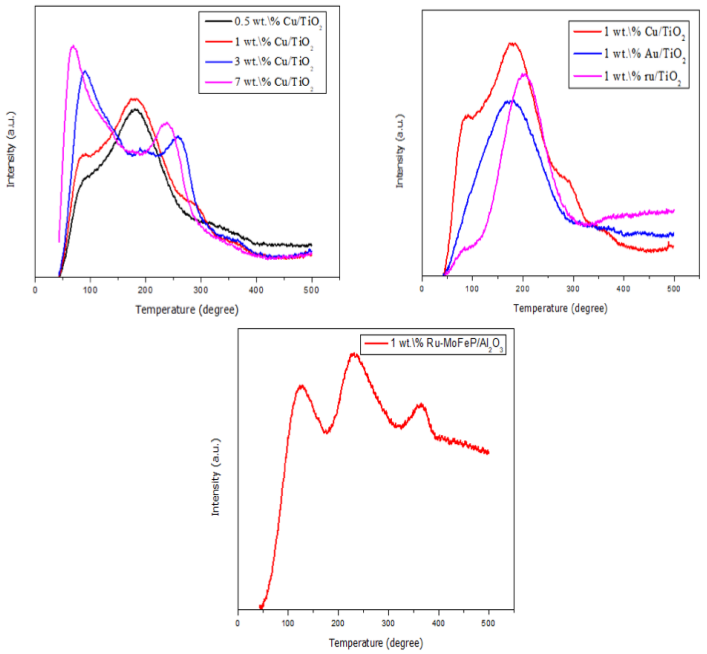

Figure 4.10: CO_2-Temperature programmed desorption plots

4.2 Development of a setup for catalyst screening

The importance of hydropyrolysis and reactor configuration for efficient bio-oil production had been discussed in section 2.6 and 2.7. It was concluded that the fluidized bed followed by fixed-bed reactor configuration is practical for the production of biofuel. Established IH^2 and H_2-bio-oil technology were a stepping example of the above-mentioned reactor configuration. Further, it was previously mentioned in section 2.5 that the fixed-bed reactor is efficient in catalytic screening. Inspired by the H_2-bio-oil technology, two fixed-bed reactor in series was built was for fast catalytic screening unit required to screen the active

catalyst. The non-catalytic hydropyrolysis is accomplished in reactor-1, whereas ex-situ catalytic up-gradation in reactor-2. This section will discuss the development and the technical difficulty faced during the development of the setup.

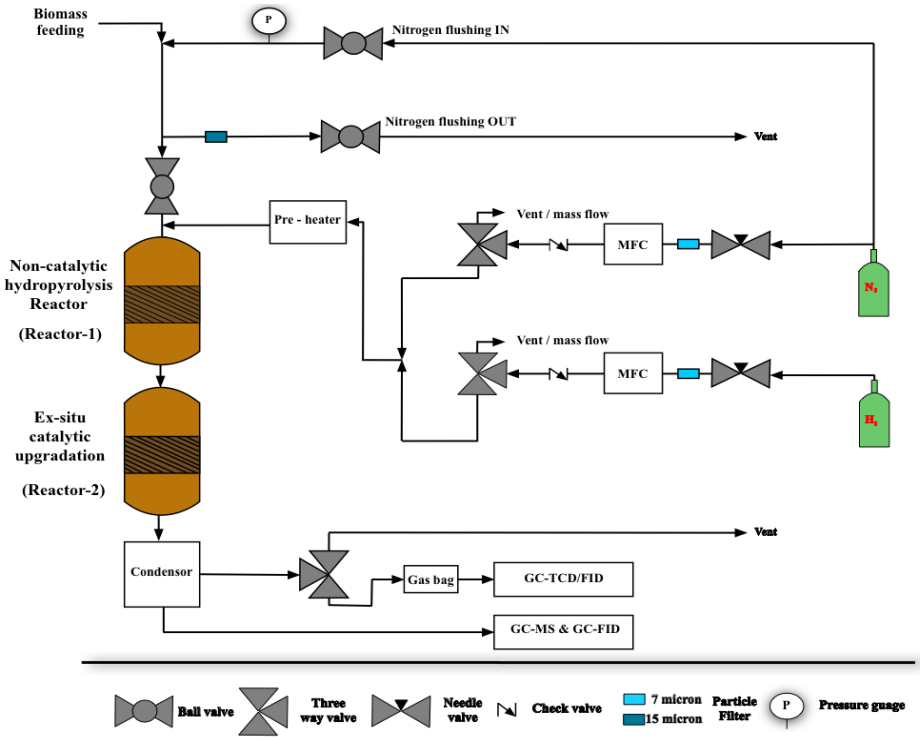

Figure 4.11: Ex-situ upgradation of non-catalytic hydropyrolysis of biomass flowsheet

A process flowsheet for reactor configuration with gas lines is shown in figure 4.11. The carrier gas H_2/N_2 is fed from the top of the reactor-1. An inert atmosphere is created by nitrogen flushing after loading biomass in the biomass loading compartment, which will be discussed in section 4.2.1. Non-catalytic hydropyrolysis and ex-situ up-gradation is carried out in reactor-1 and reactor-2, as shown in figure 4.11, respectively. The heating ovens are shown in figure 4.12. The liquid product can be recovered by the condenser aided with cooling bath/ice placed in a vacuum flask, which will be discussed in section 4.2.5 and 4.2.6. The non-condensable gaseous product passed through the condenser and captured in a gasbag, as shown in figure 4.13. The mass flow controller for H_2, N_2 and air were calibrated utilizing soap bubble meter and validated using digital flow-meter shown in figure D.1 (Appendix). The mass flow controller calibration for N_2 and H_2 gas is shown in figure D.2 (Appendix). The liquid and gaseous product is analyzed by GC-MS/GC-FID and GC-TCD/FID as previously mentioned in section 3.2.6 and 3.2.7, respectively. The Swagelok tubes and fittings used during the development of setup is shown in figure E.1, E.2, E.3, E.4 and E.5 (Appendix).

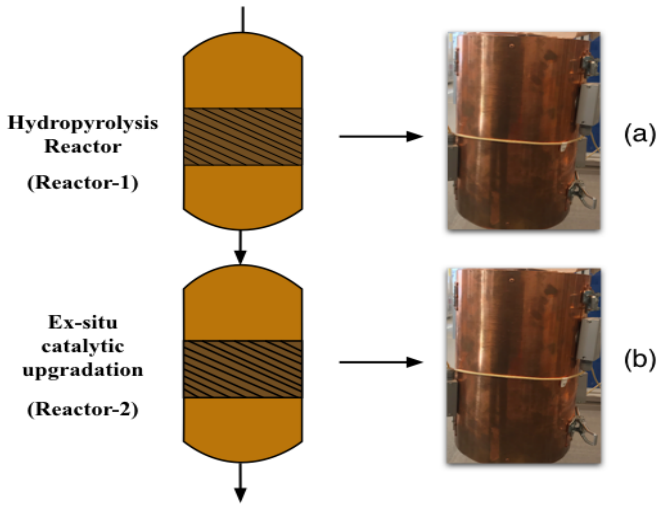

Figure 4.12: Heating oven for: (a) Hydropyrolysis reactor, and (b) Ex-situ catalytic up-gradation reactor

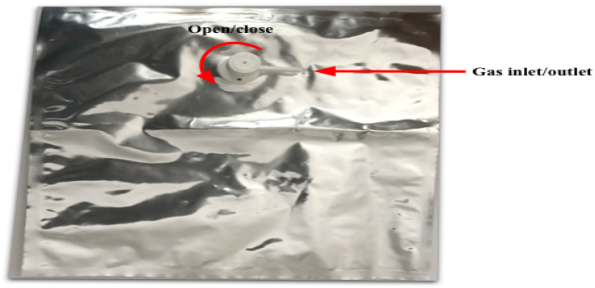

Figure 4.13: Gas bag for collection of gaseous products from the experiments

The top zone and the corresponding intersection between the reactor-1 and reactor-2 are shown in figure 4.14. It can be seen that alumina brick with required shape is placed over the top of both the reactors for the purpose of insulation. In regards to the Swagelok union which combines the reactor-1 and reactor-2 is wrapped with heating coil and fibre-glass cloth, respectively. This is established for preventing condensation of hydropyrolysis gaseous product from reactor-1. The temperature of the intersection (Swagelock union) can be controlled by adjusting the voltage supply (0-230V), shown as a blue box in figure 4.14. It can be seen that the thermocouple for reactor-1, reactor-2 and intersection between two reactors is inserted through the right side. In all the cases, the thermocouples are placed on the external wall of the reactors.

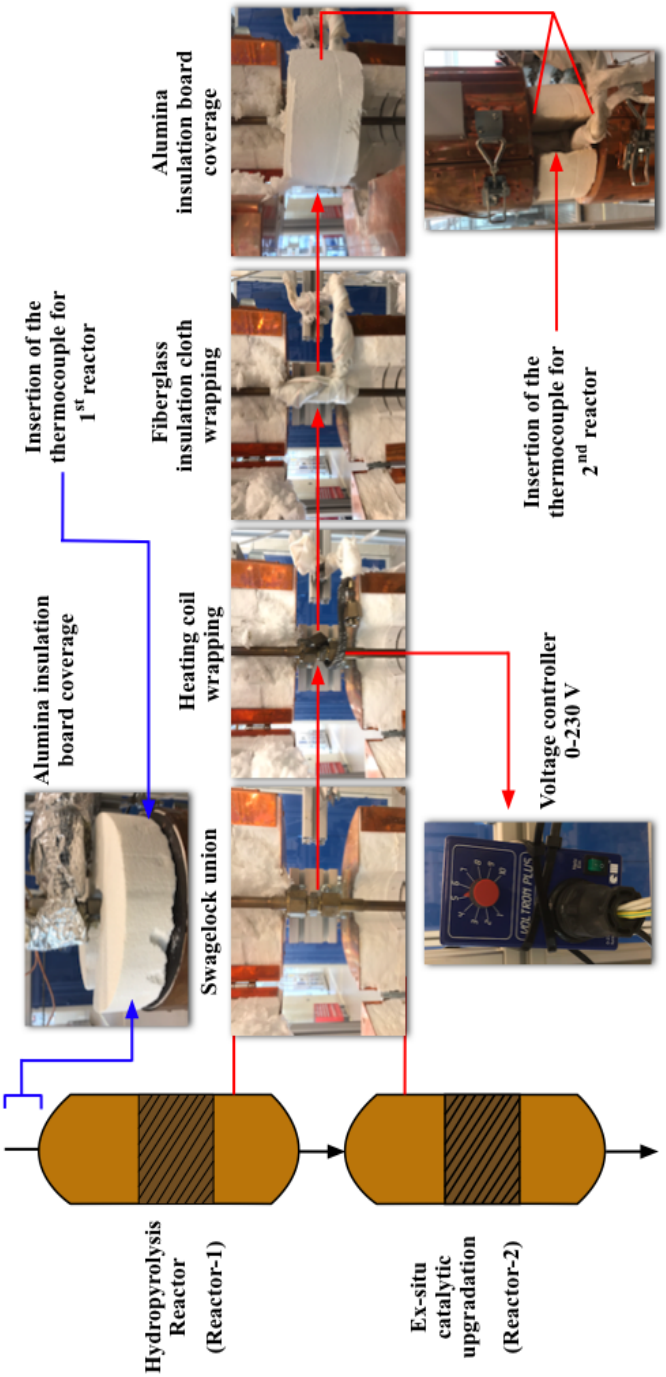

Figure 4.14: Top zone and interconnection region between 1^{st} and 2^{nd} reactor

4.2.1 Biomass feeding compartment

The pinewood powder in the range of 250-500 microns was used as a feedstock for the non-catalytic hydropyrolysis experiments, as shown in figure 4.15. Version-II of the biomass feeding zone is shown in figure 4.16 (b) which consisted of 7 cm long stainless steel (inner diameter = 0.7 cm) tubing with two 2-way ball valves at each end. The upper ball-valve functioned to prevent hydrogen gas leaks, whereas the bottom ball-valve is used to held the biomass and manually opened when the desired set-point temperature in both reactors is achieved.

Herein, the first issue faced was due to the stickiness of the pine powder. Majority of the biomass sticks into walls of the loading chamber and does not fall down towards the 1^{st} reactor when the ball valve-2 is manually opened. It is due to the electrostatic charge developed between biomass-biomass particle, and biomass-metal wall interaction which had always been an issue in powder handling. It is reported that small biomass particles tend to cohere to the walls of the fluidized bed and pneumatic transport lines [180]. Additionally, it was observed that the static charge increases with biomass drying. Multiple trials were undertaken for calibrating the loss of biomass exiting the biomass loading zone into the reactor-1. Unfortunately, less than 10% of the feedstock enters into the reactor-1. The second concern was the low loading of pinewood powder into the biomass compartment, which will be discussed in the later in this section. Therefore, the first version of biomass loading compartment was discarded and Version-I was built, as shown in figure 4.16 (a). Similar to the previous version, a ball valve was used to hold the biomass and manually opened after the desired set-point in reactor-1 is reached. In contrast, Swagelock fitting 1/2" cap replaced the manual ball valve-1 of the first version for simplicity and cost factors. It is to be noted that the length of the biomass loading compartment could not be increased more than 24 cm due to height restriction inside the rig where the hydropyrolysis setup is built. In order to confirm the leak-proof of the Swagelok fitting cap, hydrogen gas was flown in the feeding compartment, and a hydrogen gas detector was utilized to verify its leak-proof characteristic.

Figure 4.15: Pine wood powder (250-500 µm)

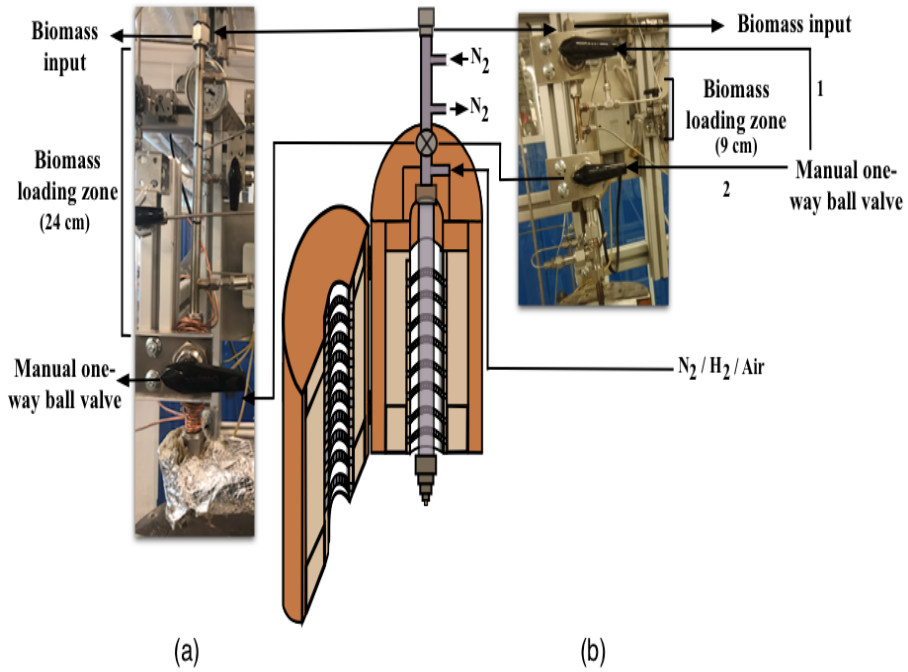

Figure 4.16: Biomass loading zone over top of the reactor-1: (a) Version-I, (b) Version-II

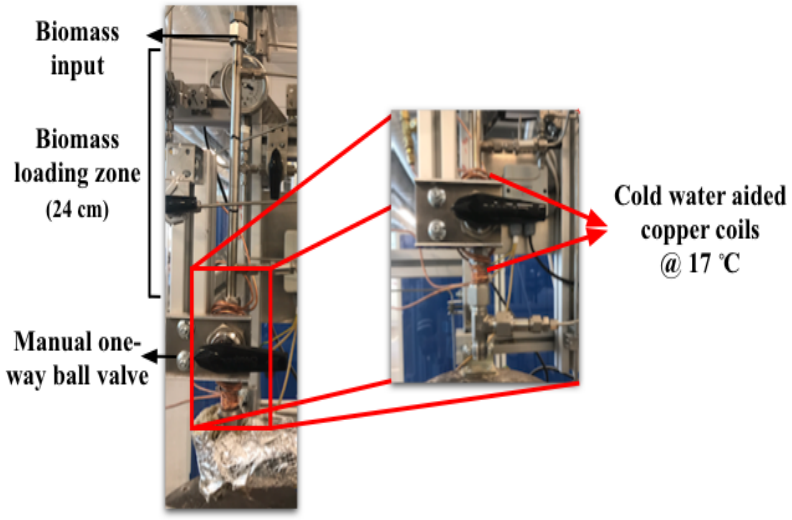

Figure 4.17: Cold copper coils for cooling Swagelock ball valve from the heat radiated by the reactor-1

The heat radiated from the reactor-1 (operating at 600°C), once destroyed the Teflon liner inside the Swagelock ball valve. Consequently, the opening/closing function of ball malfunctioned. Therefore, the modified biomass feeding compartments was further assisted with copper coils which surrounded the Swagelock ball valve, as depicted in figure 4.17. It was observed that cold water at 17°C was sufficient for effective closing and opening of the ball valve during the experiment. However, the surrounding region of the ball valve is still warmer relative to ambient temperature.

4.2.2 Biomass feeding device

Many investigations were conducted in order to overcome the biomass feeding issue. An overview on the major issue with biomass feeding device is shown in table 4.3. Initially, a cylindrical pellet was made out of a mixture of biomass and polyethene (acting as a binder), as shown in the figure 4.18. The required amount of mixture is taken and poured into a closed cylindrical aluminium foil and kept inside the oven at 150°C for 1 minute. Later, the tubular foil is cooled down in fumehood until it reaches room temperature.

S.no	Loading type	Major Issue	Utilized
1	Mixture of biomass + polyethelene	1)High PE loading needed for good binding, which led to decrease in total biomass loading. 2)PE melts on to the ball valve due to heat transfer from reactor-1.	No
2	Square-shaped SS mesh	1)Difficulty in folding the mesh into cube shape, which can fit inside reactor-1 (ID = 1 cm).	No
3	Triangular prism SS mesh	1)Difficulty in folding the mesh (50 mesh size) into triangular prism shape.	No
4	Cylindrical SS mesh	1)Frequent spillage from mesh holes during biomass loading. 2)Optimal dimension required to pass through the ball valve.	No
5	Modified cylindrical SS mesh	1)Optimal dimension required to pass through the ball valve.	Yes
6	Metal cup with no capping	1)Low total biomass loading (50 mg per metal cup). 2)Clogged inside the ball valve.	No
7	Metal cup with capping	1)Low total biomass loading (50 mg per metal cup). 2)Clogged inside the ball valve.	No

Table 4.3: Major issue with different biomass feeding device.

Based on experimental trails, at least 50 wt.% of polyethene is needed to bind the pine powder into a designated shape (cylindrical) with reasonable stiffness. Figure 4.18 summarizes the comparison between the addition of 60 wt.% more and less polyethene into the pellet making mixture on the final pellet shape. It was observed from the figure 4.18 (a), that less polyethene addition led to weak binding between the wood powder and polyethene. It is a result of less polyethene available in the final mixture to contact all the pine powder to retain the cylindrical shape of the aluminium foil. However, more than 60 wt.% polyethene addition led to reasonable binding strength between the pine powders and cylindrical shape was achievable, as shown in figure 4.18 (b). The binding strength and brittleness of the cylindrical pellet increased with polyethene addition.

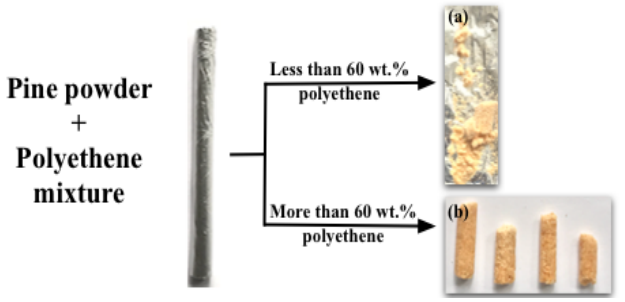

Figure 4.18: Cylindrical pellet via (pine powder + polyethene) mixture

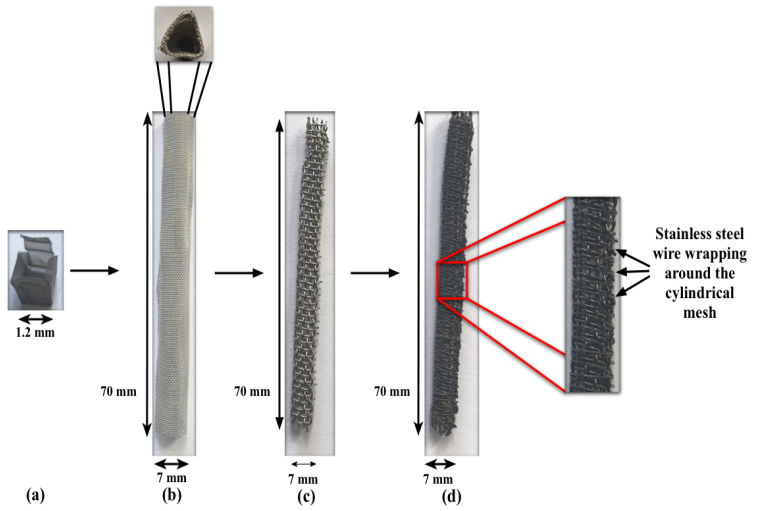

Figure 4.19: Biomass loading chambers-I

The above built cylindrical pellet was used to check its applicability in the biomass feeding zone. The results were not reliable due to the following reasons: 1) Up to 60:40 weight ratio of polyethene and pine powder, the pellet drops and breaks on top of the closed ball valve. The non-bonded biomass inside the pellet sticks to the walls of the loading compartment as previously mentioned. This led to an unreliable amount of biomass entering into the reactor-1, 2) At higher polyethene loading, the maximum biomass loading inside the loading compartment decreased to $\leq$ 300 mg, and 3) The heat radiated from the reactor-1 heats the ball valve despite cold water copper coils surrounding the ball valve. This resulted in melting of the pellet on top of the closed ball valve. Overall, polyethene as a binder for biomass feeding was unsuccessful.

Different variants of physical biomass loading camber was built from Stainless Steel (SS) mesh (25 and 50 mesh size) to check its applicability in the biomass feeding zone, as shown in figure 4.19. Firstly, stainless steel was folded into a square-shaped chamber to load the biomass inside, as shown in figure 4.19 (a). The minimum length of the square could be folded no less than 1.2 cm. Unfortunately, the largest inner diameter of the reactor-1 was available at 1 cm, which will be discussed later in this section. Due to size restriction, the square mesh could not be tested in the biomass feeding zone. Secondly, triangular prism mesh (length = 70 mm; width = 7 mm) were tried dropping into the biomass feeding zone, as shown in figure 4.19 (b). The triangular mesh dropped successfully into the reactor-1 when the ball valve was opened. However, utilizing a closely (25 mesh size) packed mesh seemed impractical due to low flow rate (30-100 ml/min) of sweep gas (N_2/H_2), heat and mass transfer restriction inside and outside the mesh during hydropyrolysis. Additionally, it was difficult to fold a larger mesh (50 mesh size) into a triangular prism with a width less than 1 cm. Therefore, the triangular mesh was not utilized to conduct hydropyrolysis experiments. Thirdly, cylindrical mesh (50 mesh size) with similar length and width was inspired from the previous version of a triangular prism mesh, as shown in figure 4.19 (c). This version of the biomass loading chamber was successful similar to the previous version in dropping safely into the reactor-1 from biomass feeding zone. However, there was one major problem faced while filling the cylindrical mesh with biomass. The biomass kept falling outside during filling, weighing and loading of biomass into the reactor. This issue was overcome by modifying the cylindrical mesh, as shown in figure 4.19 (d). A stainless steel wire of diameter 2 mm was utilized in wrapping the open-mesh boxes of cylindrical mesh. This prevented the biomass from falling outside during aforementioned issues. This version of cylindrical mesh was used to load biomass in all the hydropyrolysis experiment conducted in this master thesis.

Two major issues were faced while designing a cylindrical mesh. Firstly, the width must be less than the inner diameter of the reactor (10 mm), and empty distance of $\geq$ 2 mm around the cylindrical mesh is needed for its safe travel through the internal section of ball valve without getting clogged. Secondly, the length of the cylindrical mesh was crucial. An optimum length and width of 70 and 7 mm were found by dropping cylindrical mesh with varying dimensions. Every time the ball valve was closed and opened after loading three consecutive cylindrical mesh over the top of another inside the biomass feeding zone (Version-I). The three modified cylindrical mesh loads upto 600 mg and occupies $\approx$ 90 % length of the biomass feeding compartment as previously shown in figure 4.16 (a).

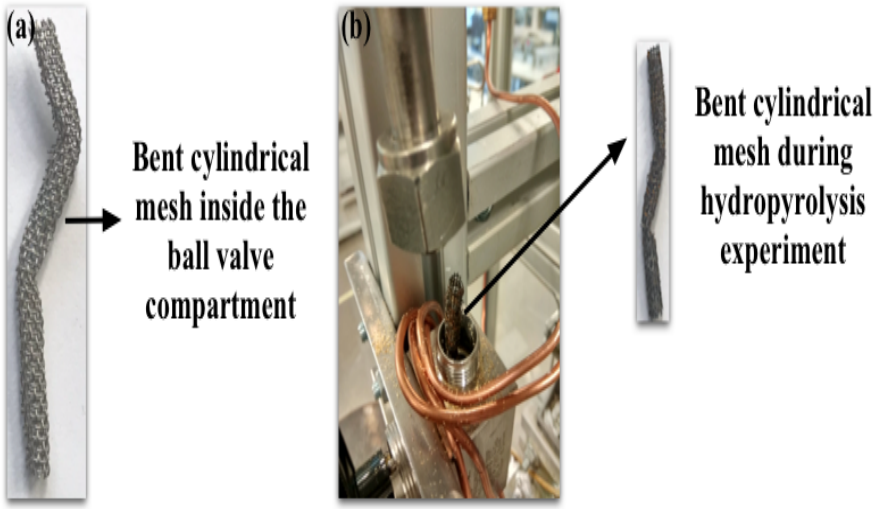

Figure 4.20: Bent cylindrical mesh (a) During designing biomass feeding chamber, and (b) Hydropyrolysis experiment

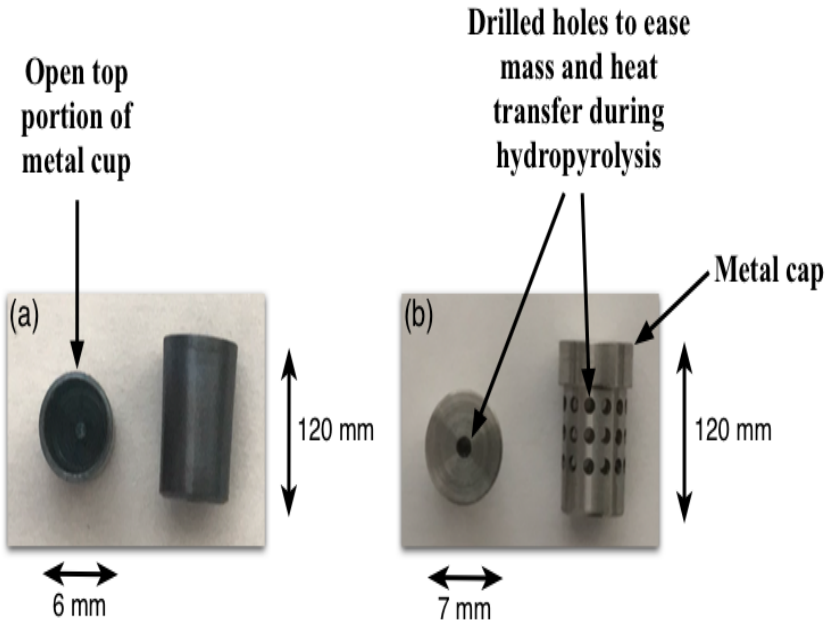

Figure 4.21: Biomass loading chambers-II

Figure 4.20 shows the unsuccessful version of the cylindrical mesh during designing and hydropyrolysis experiment. Figure 4.20 (a) shows the bent cylindrical mesh due to the lengthy cylindrical mesh (more than 70 mm). However, the cylindrical mesh with optimum dimension was also observed to get stuck during the hydropyrolysis experiment. It can be visualized from figure 4.20 (b) that first cylindrical mesh got stuck inside the ball valve, which held the second and third cylindrical mesh over the top of one another. On average, it was observed to take place once in every ten experiments.

In the meanwhile, other biomass loading chambers such as cylindrical metal cups with open and closed top were also designed, as shown in figure 4.21. The initial version of the metal cup was loaded with biomass and covered with quartz wool, as shown in figure 4.21 (a). However, $\leq$ 50 mg was only able to be filled in this version of the metal cup. Figure 4.21 (b) shows a modified version of metal cups with the metal cap. The metal cap was designed to prevent the biomass from falling outside while dropping into the biomass feeding zone. The holes were drilled for fluent mass and heat transfer from metal cups during biomass hydropyrolysis. However, the loading quantity of biomass remained same as the previous version. The metal cups could not be further tested and developed due to less biomass loading per cup (6 cups were available), blockage during the ball valve opening while unloading the metal cups into the reactor-1 and time constraints.

The biomass loaded cylindrical mesh had been tested in the biomass feeding zone of the hydropyrolysis setup. In every trial, three cylindrical meshes are loaded and placed consecutively over top of the other in the biomass feeding zone. To accommodate 3 cylindrical mesh (length = 21 cm) for reasonable biomass loading was one of the reasons for increasing the height of the biomass loading compartment from 10 to 24 cm in figure 4.16 (a). The biomass loaded cylindrical mesh was dropped from the top of the feeding section with the ball valve in a closed position. It was observed that some of the biomass particles comes out of the cylindrical mesh during the drop-down and spill over the ball valve (closed position). The nitrogen gas (100 ml/min) utilized to sweep the feeding zone for 20 min after each loading. This was accomplished to take into account the loss of biomass carried by the sweeping gas (N_2) in the feeding chamber during real hydropyrolysis experiment. The cylindrical mesh was collected in an airbag after manually opening the ball valve. The weight of the airbag before and after collection of the biomass loaded cylindrical mesh was tabulated, as shown in table F.1.

The biomass input into the reactor is very crucial for mass balance in the hydropyrolysis experiment. Therefore, the testing had been executed at a different time interval during the day and total biomass loaded every time was varied in order to rely on the quantity of biomass entering into the reactor-1. The table F.1 (Appendix) shows the loss in biomass either being carried away by the sweeping gas or biomass powder sticking on the feeding chamber wall, which fell during the drop down onto the ball valve. It was observed that $<$ 1% of the total biomass was lost during biomass feeding. Additionally, the particle filter (15 microns) placed next to the N_2 gas flushing outlet was opened to check for the traces of biomass particle (250-500 micron). There was no traces of biomass particle. Therefore, the cylindrical mesh shown in figure 4.19 (d) was considered reliable for loading biomass and conducting the hydropyrolysis experiment.

4.2.3 Reactor sizing

The SS tubing was utilized as a reactor for hydropyrolysis and ex-situ catalytic up-gradation. In this regard, three factors led to the optimization of the length and inner diameter of the reactors. Firstly, as mentioned in section 2.3, the fast pyrolysis/hydropyrolysis vapours must be quenched quickly to avoid additional secondary cracking of pyrolyzed biomass vapours in the gas phase. Secondly, the temperature no less than 300-350°C must be maintained in the intermediate gas line (zone/tubing which is not exposed to hydropyrolysis/ex-situ reactor temperature condition) until the gas vapours reach the condenser. Otherwise, unavoidable condensation and loss of collectable product will be observed. Therefore, the unnecessary length of the reactor tubing must be reduced to prevent avoidable exposure to the ambient atmosphere. Figure 4.22 (a) and (b) shows all three version of the reactor and interconnection (Swagelock union) between the two reactors. The earlier model R-1 reactor was 45 cm in length, whereas the other reactors R-2, R-3 had a height of 39 and 32 cm, as shown in figure 4.22. For each reactor, the ambient temperature exposed space between the condenser inlet and the bottom of the heating oven was different, as shown in figure 4.23. The Spacing was 0, 15 and 70 mm for reactor R-1, 2, and 3, respectively. On the one hand, both R-2 and R-3 reactor with spiral/round bottom flask (RBF) condenser could be utilized as an ex-situ catalytic up-gradation reactor, as shown in 4.23 (a) and (b). The R-2 and R-3 reactor with RBF condenser is not shown in figure 4.23. The atmospheric exposed region between condenser inlet and heating oven bottom was lower in the former and higher in the latter. Therefore, the R-2 reactor was fixed as a 2^{nd} stage reactor for all experiments conducted in this master thesis. On the other hand, the R-1 reactor faced different issues with w.r.t to spiral and RBF condenser. The former faced a problem with the inability to close the heating oven, as shown in figure 4.23 (c). The latter suffered a hydrogen leak in which the Teflon tube melted due to high temperature ($\leq$300°C), as shown in figure 4.23 (d). The different type of condenser is briefly explained in section 4.2.5.

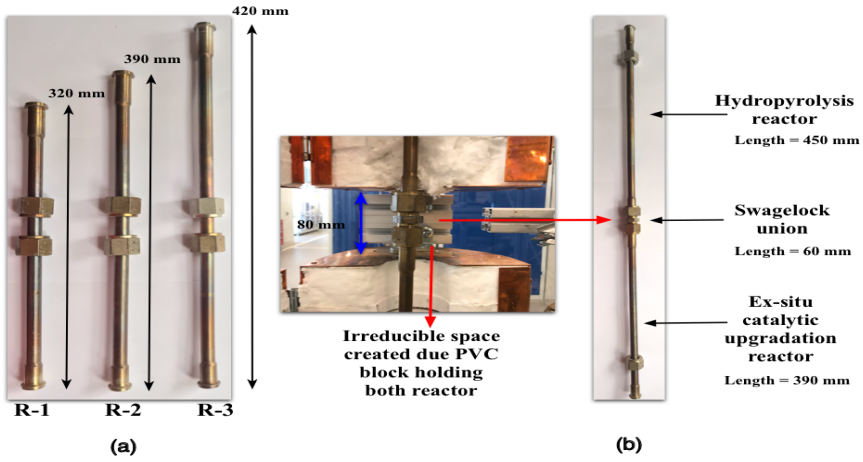

Figure 4.22: Reactor-optimization: (a) Different lengths of the reactor, and (b) Optimized reactor length

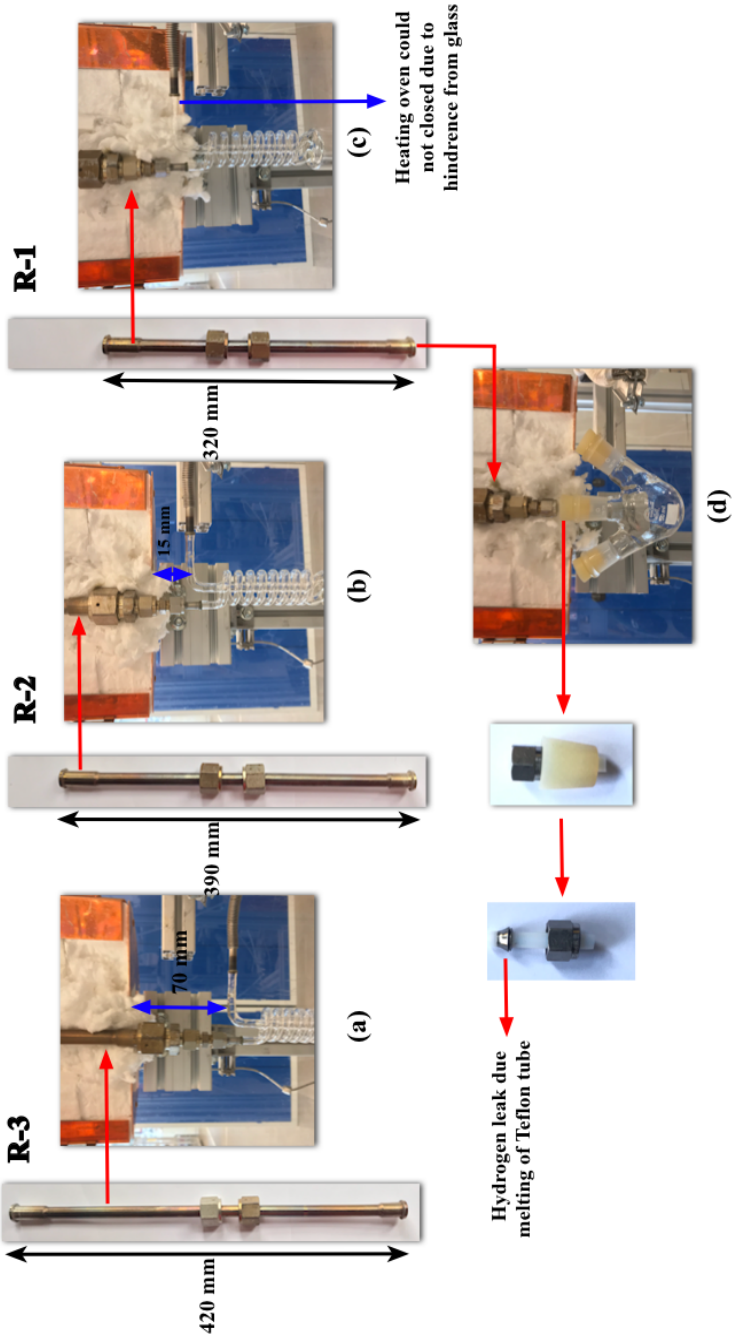

Figure 4.23: Spacing between condenser inlet and bottom of the heating oven of 2^{nd} reactor

One has to note that, simultaneous utilization of both reactors in hydropyrolysis combined ex-situ up-gradation requires the reactor with 45 cm length due to default spacing (8 cm) generated by polyvinyl chloride block holding two heating ovens, as shown in figure 4.22 (b). Surprisingly, the length of the Swagelok union was 60 mm which occupied 3/4 space between the two heating ovens when connected with R-2 reactor. Therefore, due to the aforementioned factors, the R-3 (length = 45 cm) and R-2 (length = 39 cm) reactors were exclusively utilized for non-catalytic hydropyrolysis and ex-situ catalytic up-gradation respectively, in this master thesis.

Finally, the inner diameter of the reactor was an influential factor for the safe travel of cylindrical mesh into the reactor-1. Figure 4.24 shows an intersection (welded joint) between two different SS tubing of 10 and 7 mm. Unfortunately, this hump was responsible for the cylindrical meshes to get clogged at this spot. Therefore, new SS tubing with bigger diameter (10 mm) was utilized to weld at this intersection, as shown in figure 4.24 (b). Herein, in this master thesis, all the experiments were conducted with 10 mm internal diameter, as shown in figure 4.24 (b).

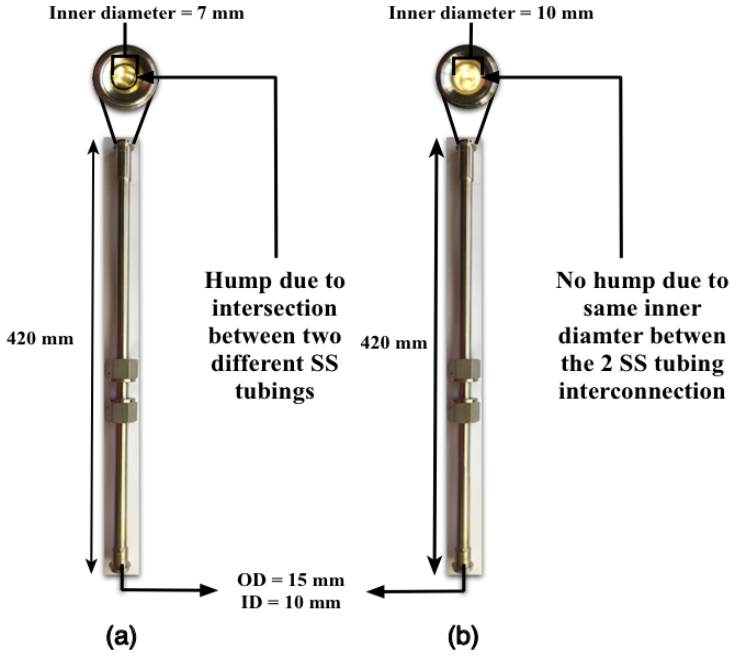

Figure 4.24: Optimized version of internal diameter of reactor tubing

4.2.4 Temperature study

The utilization of the three cylindrical mesh for loading biomass led to the usage of the majority of internal space of the reactor-1 (42 cm). In this regard, the fixed bed reactors for both hydropyrolysis (reactor-1) and ex-situ (reactor-2) upgrading reactor was calibrated for temperature variation. In order to obtain an optimum placement of thermocouple, the temperature variation in the reactor was recorded at different zones. The two objectives of this study were to achieve an optimum temperature between 500 to 600°C and 350 °C throughout reactor-1 and reactor-2 (catalyst placed at mid-zone), respectively. The temperature variation data had been validated by recording the temperature three times after successive cooling down to room temperature after every run. Both the reactors were completely insulated with quartz wool and insulation brick during each run to minimize heat loss to the atmosphere, as previously shown in figure 4.14. The external heating coil was used to maintain the intermediate section between the reactors at 350°C (300°C was shown to avoid condensation of hydropyrolysis products which will be discussed in section 4.3). Each study was recorded for either one hour or until the temperature was stabilized.

Reactor-1

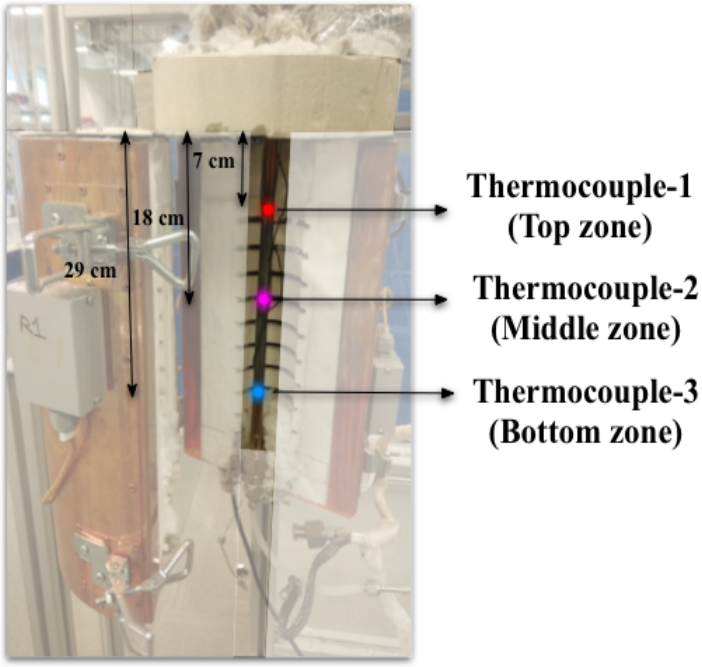

Figure 4.25: Thermocouple placement during temperature variation study

The initial test was performed on reactor -1. The reactor-1 had compact inner diameter (1 cm) and biomass loaded mesh feeding system (Version-I) over the top. Firstly, the set-point controlling thermocouple was placed internally in the middle zone of the reactor, not shown in figure 4.25. Additionally, three more thermocouples were used to measure the outside temperature of the top, mid and bottom zone of the reactor, respectively, as shown in figure 4.25. The thermocouple controlling the set-point temperature of the reactor-1 was set at 600°C. A short overview of the temperature variation data over different placement of set-point thermocouple is discussed. It is to be noted that the set-point controlled thermocouple was not tested on top-zone of the reactor since its impossible to achieve the desired temperature at mid and bottom-zone.

The observation in the first 15 minutes after reaching set-point show that there exists a temperature difference of 10-15°C between the inner and outer wall of the stainless tube reactor located at mid zone of the reactor-1. This proves that there always exists a temperature difference of $\approx$ 10°C in-spite of maintaining the oven temperature constant over time, On the other hand, the outside temperature of the top zone was reasonably at 565°C. Unfortunately, the bottom zone was at $\approx$ 300°C, as shown in figure 4.26. This can be explained by hot air from bottom zone moving upwards and simultaneously heating the top zone (conduction and convection), and lack of heat input to the bottom zone since set-point of the reactor-1 was already achieved. The insufficient volatilization temperature (at least 500°C needed) for biomass at the bottom zone led to a search for a new place for the set-point controlled thermocouple.

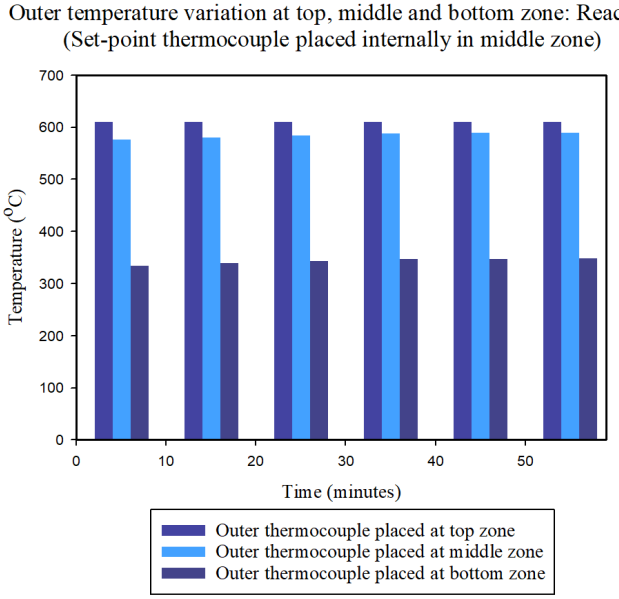

Figure 4.26: Reactor-1: temperature variation study - 1

Next, the set-point controlled thermocouple was placed internally inside reactor-1 at the bottom zone to study the temperature variation (not shown in figure 4.25). Similar to the previous study, three other thermocouples were placed externally at top, mid and bottom one of reactor-1, as shown in figure 4.25. The temperature was recorded for 120 minutes after the set-point temperature was reached.

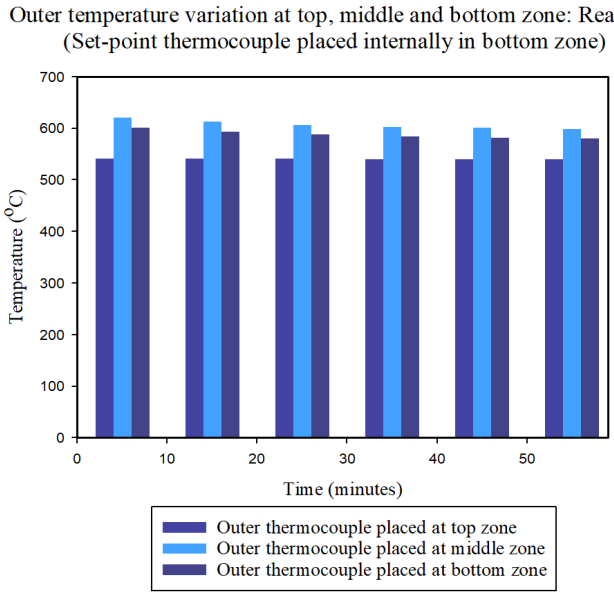

Figure 4.27: Reactor-1: temperature variation study - II

It is evident from the figure 4.27 that, placing the thermocouple at the bottom zone had given an advantage over all the three-zone of the reactor-1. After 1 hour of observation, the internal temperature throughout the reactor-1 (top-mid-bottom zone) was able to be maintained between 540 - 600°C. Thus, the location for the set-point thermocouple was fixed at bottom zone for all the experiments conducted in this report. Additional care was taken during every experiments to place the thermocouple exactly at the desired location.

Reactor-2

The study on temperature variation for reactor-2 was straightforward, unlike reactor-1. The two objectives were to maintain the isothermal region of 350°C for catalytic activity at the mid-section and to record the temperature variation at the top, bottom and mid zone of the reactor-2.

From observation, the temperature of the internal and external of any zone was easily achieved wherever the set-point controlled thermocouple was placed. As expected, the internal and external temperature of mid-zone was $\approx$ 350°C when the set-point controlled thermocouple was placed at mid zone. Therefore, the internal temperature variation over

the top zone and bottom zone was studied when the set-point thermocouple was fixed externally at mid-zone. Further, isothermal region is needed for the catalyst placed at mid-zone.

An 60 min observation was conducted until the desired set-point temperature was reached at the mid-zone, as shown in figure 4.28. Internal temperature reading of 358, 350 and 240°C at top, mid and bottom zone, respectively was observed. Therefore, the mid-zone was selected as an optimum location for set-point controlled thermocouple at reactor-2. Similar to reactor-1, additional care was taken during each experiment to place the thermocouple precisely at the desired location. It is to be noted that the bottom zone temperature could not be raised more than 300°C while maintaining 350°C at mid-zone. Further, other restriction included the utilization of the glass condenser, which will be discussed in the section 4.2.5.

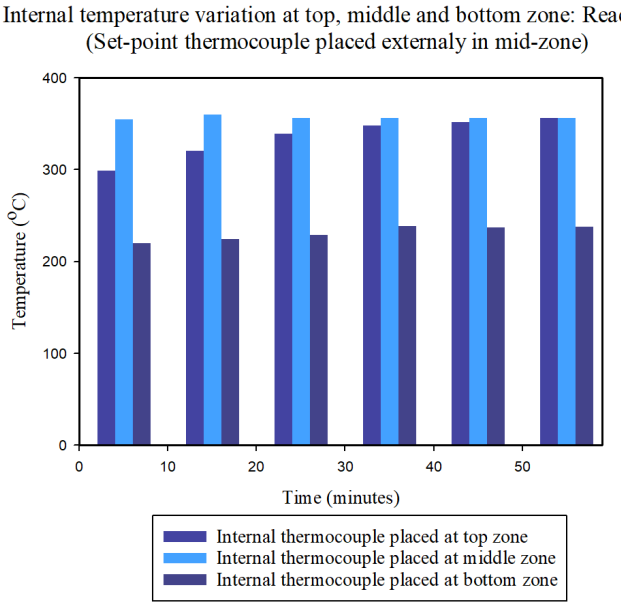

Figure 4.28: Reactor-2: temperature variation study - 1

4.2.5 Condenser design

A condenser is an essential part of the hydropyrolysis setup. A condenser is utilized to condense the non-catalytic hydropyrolysis/ex-situ upgraded bio-oil vapours from reactor-1 and 2, respectively. Unfortunately, there is limited information available in the literature about the design of condenser in thermochemical conversion technique, as previously mentioned in section 2.7.3. Therefore, developing a dedicated condenser which has both long residence time for gaseous vapours and trouble-free product collection, the condenser had been modified multiple times, as shown in figure 4.29 and an overview of the major issue is listed in table 4.4

The earliest condenser design was a spiral condenser (C-1), as shown in figure 4.29 (a). This condenser had been successful in collection of pyrolysis products (from lignin) conducted in an inert nitrogen atmosphere. It is to be noted that previous master student utilized solvent (2-3 ml mixture of ethyl acetate and cyclohexane) to maximize the recovery of BTX and its derivatives from pyrolysis of lignin. There were two drawbacks of C-1 condenser: Firstly, hydrogen leak was observed due to lack of proper sealing joints on the inlet and outlet of the condenser. Instead, a silicon rubber tube was used as an intermediate connection, as shown in figure G.1 (Appendix). Secondly, the residence time for inlet gas vapours to contact the organic solvents was negligible, as shown in figure 4.30 (a). These factors led to the modification of the condenser with the proper gas proof fitting connection. Additionally, internal glass tubing was placed which takes the gas vapours to the bottom of the condenser, as shown in figure 4.30 (b). This led to increase in the gas residence time, contact time inside the condenser and with the organic solvents, respectively. This condenser is named as C-2.

Condenser type	**Major issue**	**Inside final setup**
C-1	1.No metal connection for leak proof hydrogen flow. 2.Low residence time for gas products and liquid products to contact organic solvent.	No
C-2	1. Post liquid collection was difficult. 2. Weak metal-glass interconnection at inlet. 3. Condenser handling inside vacuum flask. 4. Capturing low boiling products (BTX). 5. Product dilution in GC analysis.	No
C-3	1. Post liquid collection was difficult. 2. Weak metal-glass interconnection at inlet. 3. Condenser handling inside vacuum flask. 4. Product dilution in GC analysis.	No
C-4	1. Weak metal-glass interconnection at inlet. 2. Condenser handling inside vacuum flask. 3. Product dilution in GC analysis.	No
C-5	1. Weak metal-glass interconnection at inlet. 2. Product dilution in GC analysis.	Yes
C-6	1. Poor product recovery during catalyst usage in ex-situ up-gradation reactor.	Yes

Table 4.4: Major issue with different type of condenser

The modified spiral condenser (C-2) had proven to work successfully without any hydrogen leaks. However, other issues were discovered. Firstly, the interconnection between the glass and metal was not able to withstand a temperature of $\leq$ 150 °C. For example, the C-2 condenser broke when R-2 reactor was utilized. This was due to heat transfer through the R-2 reactor to the intersection of metal-glass joint of C-2 condenser. This led to damage of the glass-metal connection of the condenser, as shown in figure 4.31 (a). Secondly, due to low biomass feeding (200 - 600 mg with both biomass feeding compartment

shown in figure 4.16), less than 50 wt.% of bio-oil was obtained (equivalent to 100 - 300 mg of biomass input loading) which will be discussed later in section 4.3. Therefore, the post-experiment bio-oil collection was an issue due to the large contact surface in-between the inlet and outlet of C-2 condenser. Most of the bio-oil sticks to the condenser surface and does not pass through the outlet, as shown in figure 4.30 (b). The organic solvent (methanol, isopropanol) was utilized to flush the bio-oil out of the C-2 condenser as it is also reported to homogenize the bio-oil for GC analysis. Additionally, it increases the stability and decreases the viscosity and density of the bio-oil[110]. Unfortunately, at least 2-4 ml of organic solvent is required to recover the bio-oil completely from the spirals of the condenser.

The organic solvent for capturing BTX and flushing of bio-oil summed up to 4-7 ml. This led to a dilution of the bio-oil components in GC-MS and GC-FID analysis. In this regard, C-3 condenser was developed. Herein, a cylindrical glass tubing of length 5.5 cm and an internal diameter of 1 cm was attached to the bottom of the C-2 condenser. Similar to C-2 condenser, inner tubing is passed to the bottom of C-3 condenser, as observed from figure 4.32 (a). An additional advantage was the bubbling of gaseous vapours (condensable and non-condensable fraction) through the organic solvents was achieved, thereby increasing the residence time inside the condenser. Additionally, less organic solvents could be utilized to capture the gaseous product compared to C-2 condenser.

The unnecessary deposition on the condenser surface could be avoided during product recovery through a quick outlet at the bottom of C-4 condenser, which otherwise passes through the conventional outlet, as shown in figure 4.32 (b). Additionally, the height was increased between the outlet and the 1^{st} spiral of C-4 condenser. This was crucial due to frequent breakage of the spiral condenser during handling when dipped inside the vacuum flask. Later, this C-5 condenser was tested without solvent to check its feasibility. Similar to C-2, C-3 and C-4 condenser, the bio-oil sticks to the walls of the C-5 condenser, as shown in figure 4.33. The flushing solvent of 3-4 ml was still a concern for product dilution in GC analysis. Despite varying the flow rate from 40 to 150 ml/min. The recovery of liquid products was still challenging with hydrogen leak proof hydropyrolysis setup.

The overall problem was narrowed to three issues: Firstly, from C-2 to C-5 condenser, low biomass feeding led to low liquid products (weight basis) which were not able to travel through all the spiral in the condenser without utilizing organic solvents for flushing. Secondly, $\leq$ 5% of the liquid product stick to the intermediate connection between the R-2 reactor and spiral condenser, which will be discussed in section 4.3. Thirdly, utilizing solvents to capture and additional usage of solvents to wash the liquid product from the spiral led to a high dilution of the liquid product in the GC analysis.

To simplify the design and to overcome the above mentioned issues, 50 ml Round Bottom Flask (RBF) with three outlets was tested in a non-catalytic hydropyrolysis experiment, as shown in figure 4.34. Unlike, C-2 to C-5 condenser, the RBF was always plugged with silicon rubber on the left side. Next, the Teflon tube is inserted into the hole of the silicon rubber. This is accomplished by drilling a small hole in the middle zone of silicon rubber with hole size less than the outer diameter (6 mm) of the Teflon tube.

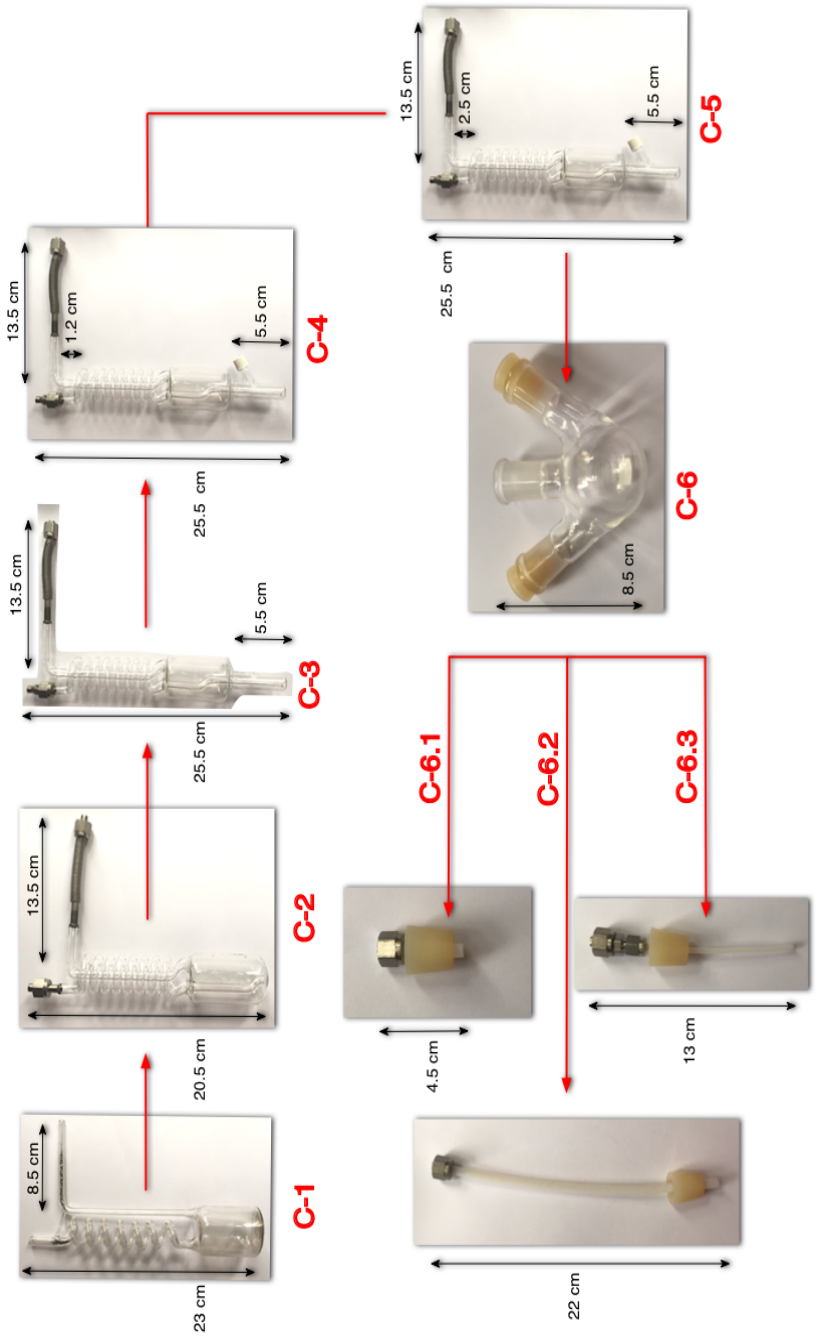

Figure 4.29: Different designs of condenser for bio-oil collection

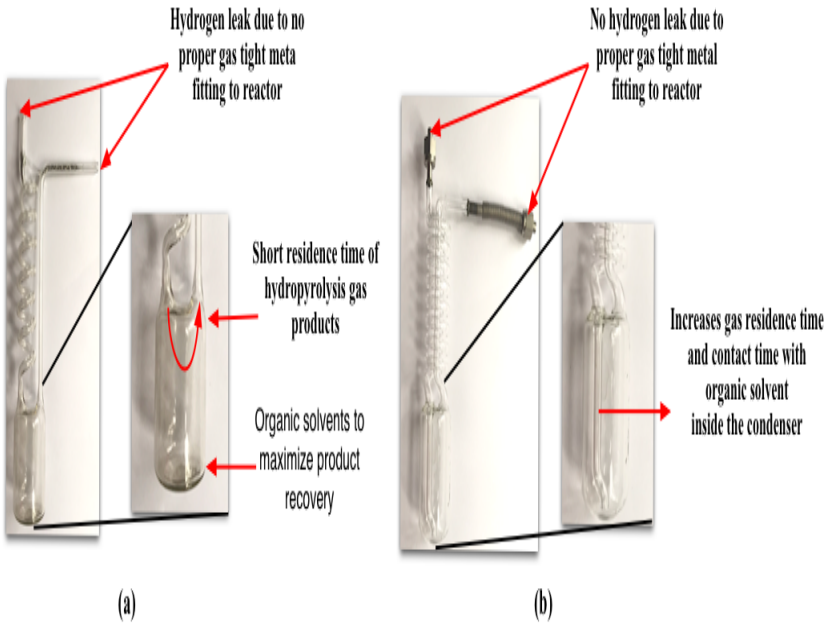

Figure 4.30: C-1/C-2 condenser: (a) Short residence time of hydropyrolysis gas vapours inside C-1 condenser, and (b) Additional tubing to increase residence time hydropyrolysis gaseous products and organic solvent contact zone

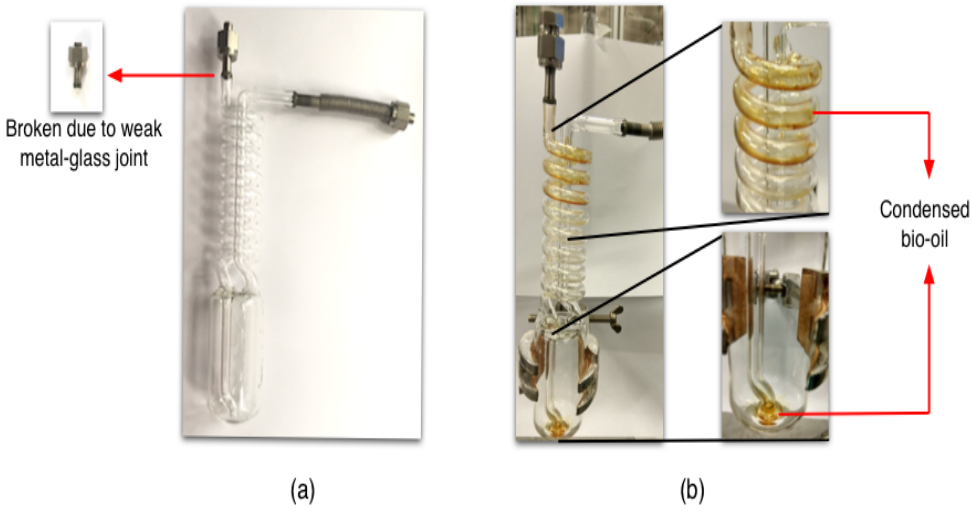

Figure 4.31: C-2 condenser: (a) Broken intersection between glass and metal, and (b) Condensation of bio-oil throughout the condenser surface

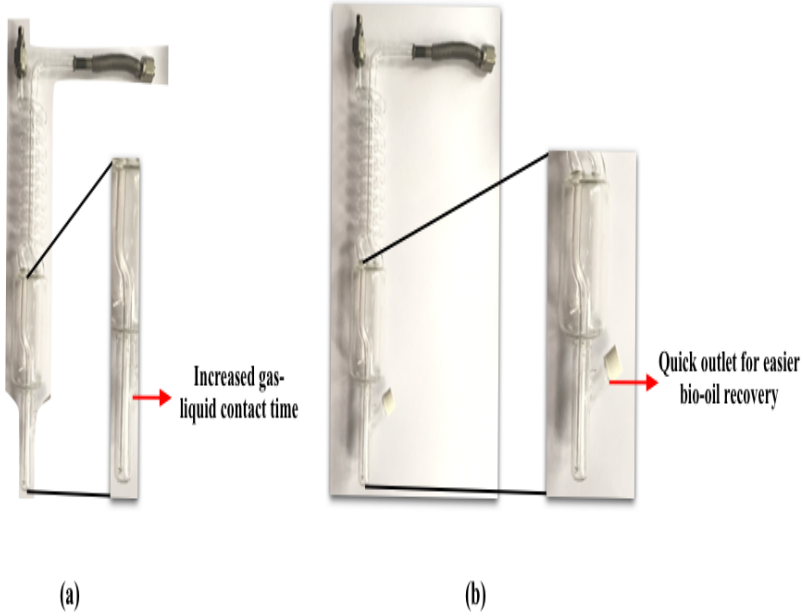

Figure 4.32: C-3/C-4 condenser: (a) Smaller cylindrical glass tube for bubbling gaseous products in C-3 condenser, and (b) Quick outlet in C-4 condenser

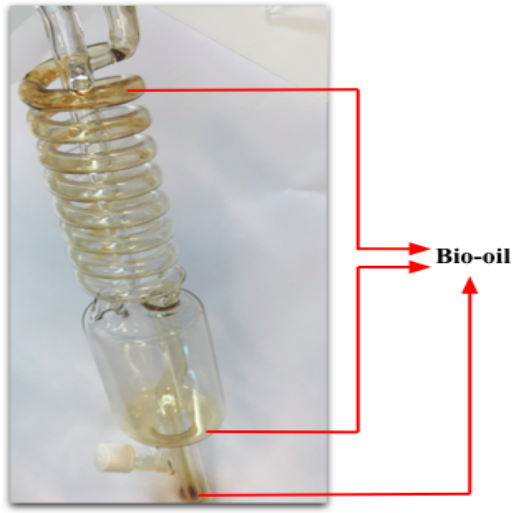

Figure 4.33: Bio-oil deposition in C-4 condenser

Figure 4.34: RBF condenser

This prevented the sweeping gas (H_2, N_2 and gaseous products from hydropyrolysis experiments) to release into the surrounding atmosphere. Hydrogen gas detector was used to further validate the leak-proof characteristic of the RBF condenser.

Similarly, Teflon tube is inserted in silicon rubber for the right and center mouth of RBF, thereby connecting to the three-way ball valve (gas collection/venting), and reactor as mentioned in section 4.2. The figure 4.34 shows all the connection to RBF condenser. The gas products are collected in a gasbag or vented out. It is worth mentioning that the required bio-oil for GC analysis with good peak elution could be obtained with relatively less solvent addition to RBF compared to other condensers.

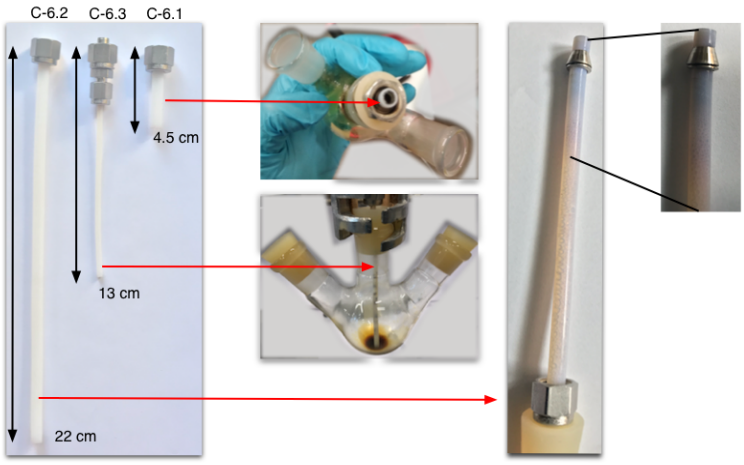

Figure 4.35: Condensation of liquid product on inner walls of Teflon tube

Figure 4.29 shows three alternatives which connect the RBF with the reactor-1/reactor-2. The C-6.1 and C-6.2 condenser had Teflon tube of the inner diameter of 0.4 cm and length of 4.5 and 13 cm, respectively. It can be observed from figure 4.35 that bio-oil is condensed on the walls of the Teflon tube. This is due to the hydrophobic nature of the bio-oil. The bio-oil condensation in a non-catalytic hydropyrolysis experiment was $\approx$ 53%, which will be discussed in section 4.3. With regards to increasing the bio-oil recovery, the Teflon tube of 13 cm (C-6.2) was utilized to increase the gas residence time compared to C-6.1. However, the bio-oil yield was similar to the C-6.1.

The main drawback of the C-6.1 and C-6.2 condenser was the product collection. The bio-oil adheres to the wall, thereby requiring more flushing solvent. This issue was overcome by C-6.3 type condenser, which is similar to C-6.1 and C-6.2 except for the length, and inner diameter was 13 cm and 0.2 cm, respectively. Herein, the bio-oil itself acted as a flushing agent. The clogging in the tube is pushed by the incoming bio-oil vapours from the reactor-1/reactor-2 and majority of the bio-oil deposit at the bottom of condenser, as shown in figure 4.35. Further, a 20 µl pipette filled with isopropanol/methanol was used to drive the remaining bio-oil in the Teflon tube into GC vials during post-experiment. The main advantage was the relatively less usage of the flushing solvent compared to C-6.1 and C-6.2 condenser. Overall, the RBF type condenser was superior in product collection and inferior with regards to the residence time of gas vapours compared to the spiral based condenser.

4.2.6 Condensing medium

The last stage on the development of hydropyrolysis setup was the condensing medium. The condensing medium is crucial for the recovery of the condensable products from thermochemical conversion technique. The key requirement for the condensing medium is the rate of condensation which depends on the cooling source. All the condensers developed in the previous section needs to be placed inside the cooling source. Herein, Dewar vacuum flask were utilized to hold the condenser and cooling source. Care must be taken to handle the Dewar flask during setting up the hydropyrolysis setup due to its fragile nature.

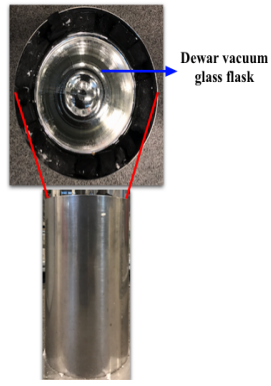

Figure 4.36: Dewar vacuum flask for placing condenser and ice

Two candidates were identified to function as a cooling source. Firstly, the condenser (RBF/spiral condenser) was placed in the middle of the vacuum flask. Secondly, the condenser was placed in an ethylene glycol-water mixture filled in the vacuum flask, as shown in figure 4.37. The former is simple as it is filled with ice at 0°C and the vacuum flask prevents the ice from melting, as shown in figure 4.36. In contrast, the latter utilizes a refrigeration unit which condenses the ethylene glycol and water mixture to - 7°C. This cold mixture is circulated through copper coils placed in the vacuum flask, thereby cooling the similar mixture inside a vacuum flask. Figure 4.37 shows an illustration of the placement of copper coils inside the vacuum flask. Total solution of 9 litres of ethylene glycol and water mixture (60:30 wt.%) was prepared, of which 7 litres was used inside the refrigeration unit and 2 litres in the vacuum flask. The cooling bath has the potential to tune the rate of condensation by adjusting the temperature of the circulating liquid mixture. It is to be noted that the cooling bath was available only during the last stages of the master thesis. Therefore, cooling bath could be utilized for any experiment conducted in this master thesis.

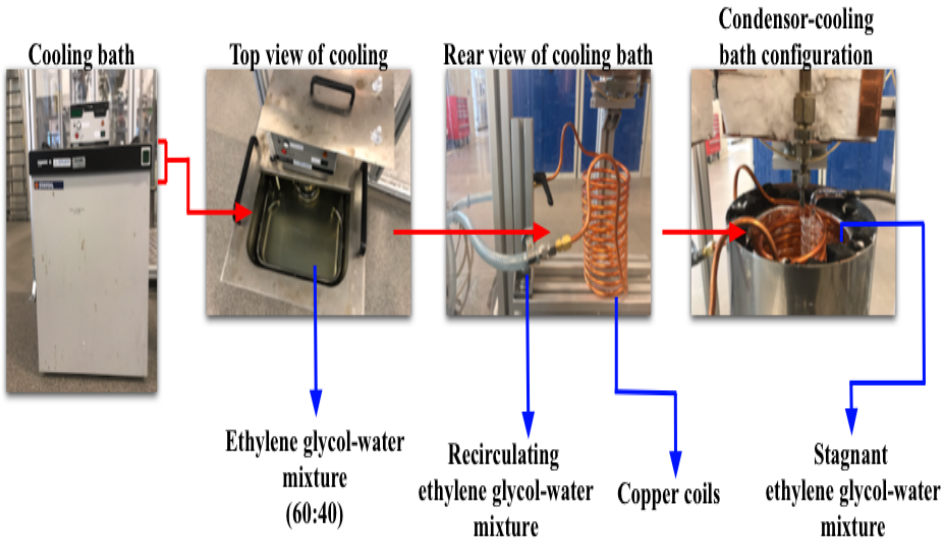

Figure 4.37: Cooling bath

4.3 Testing phase

The final developed setup for hydropyrolysis with ex-situ catalytic up-gradation configuration is shown in figure 4.38. The reactor-1 with length and internal diameter of 42 and 1 cm was used as a hydropyrolysis (non-catalytic) reactor. The reactor-2 for ex-situ catalytic up-gradation was 39 cm long with internal diameter of 1 cm. The interconnection between 2 reactor was heated with electric coil at 350°C. Three biomass filled cylindrical mesh was loaded into 24 cm biomass loading zone. The reactor-1 and reactor-2 is heated upto 500-600°C and 350°C, respectively. The ball valve was manually opened after stabilization of temperature in both the reactors for 1 hour. The pre-heated N_2 and H_2 gas at 350°C was used as a carrier gas. Herein, the nitrogen and hydrogen function as an internal standard for gas analysis and reactive atmosphere for volatalizaion of biomass/ex-situ catalytic up-grading of volatalized biomass components, respectively. The experiment is conducted for 12 minutes. The C-5, C-6.1 and C-6.3 condenser with ice/Dewar flask was used to collect the liquid products and gas bag was used to collect the non-condensable gas products.

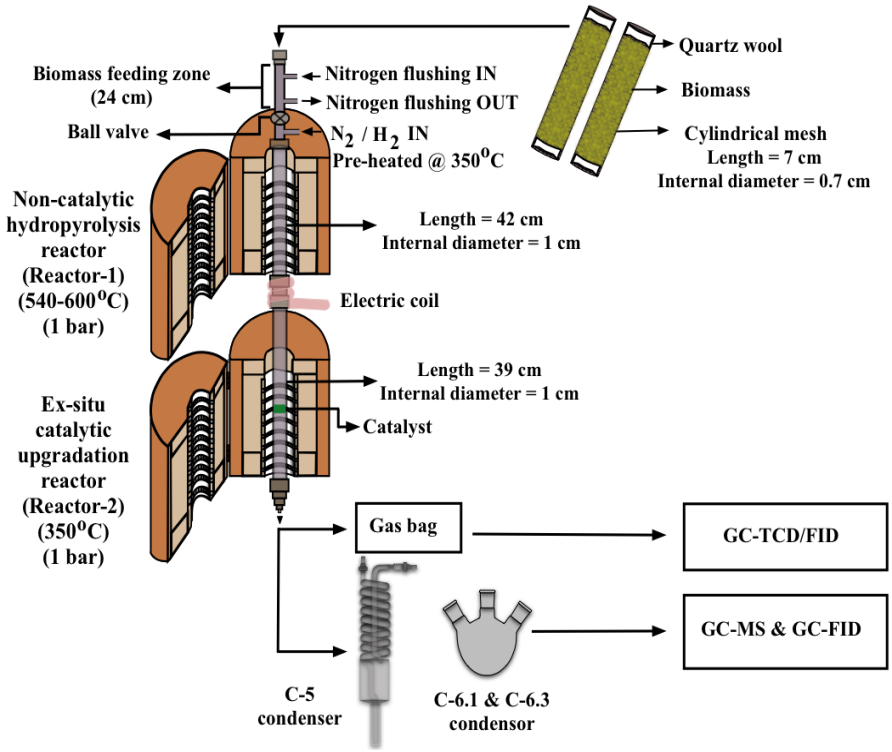

Figure 4.38: Final setup flowsheet for hydropyrolysis with ex-situ catalytic up-gradation

The reactor power supply is shut-down post experiment. The reactor, condenser, fittings is weighed again and compared with the weights before experiment to calculate the amount of bio-oil, coke and char. The non-condensable gas and liquid is analyzed using GC-TCD/FID and GC-MS/FID, respectively.

The single-stage hydropyrolysis experiment was successfully conducted exclusively with R-1 reactor. The product yield is shown in table 4.5. The consistency of the gas, liquid and char weight distribution data was verified by repeating the same experiment three times. The experiment-1, 2 and 3 show the product distribution (weight basis), respectively. Two important observation was derived: Firstly, the gas and char yield stays constant between 14-15 wt.%. The gas and char yield is close to the values reported in the literature (gas, solid char is $\approx$ 13 and 12 wt.% respectively in fast pyrolysis) [181]. Secondly, liquid wt. % is 54-55 wt.% whereas up to 75 wt.% is observed, as previously mentioned in section 2.5. It is reported that non-catalytic fast pyrolysis in H_2 atmosphere yield marginally higher bio-oil compared to its counterpart N_2 atmosphere [12]. This suggests that the hydropyrolysis setup must be further optimized. It is to be noted during gas analysis that, many unknown peaks were observed in the GC chromatograms apart from N_2, H_2, CO_2, CO, CH_4 and C1-C6 (including corresponding alkane and alkenes) , as shown in figure H.1 (Appendix). Therefore, the RBF based condenser and ice as cooling medium requires further optimization for high bio-oil recovery.

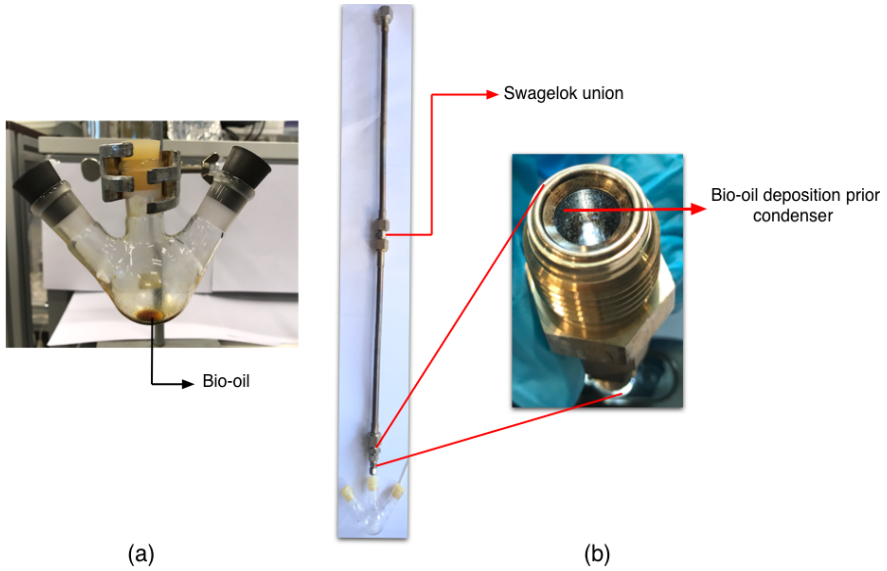

Figure 4.39: Deposition of bio-oil prior condenser

Similarly, two-stage non-catalytic hydropyrolysis (using two reactors) was utilized to check for the product yield consistency with a single-stage reactor. Surprisingly, the product was similar to experiment-1, 2 and 3. The gas, solid and liquid were $\approx$ 14, 14 and 55 wt%, as observed from experiment-5 in table 4.5. It was suspected that higher flowrate (total flow = 100 ml/min) might be one of the plausible reason for lower liquid recovery in the RBF condenser. Therefore, experiment-4 conducted at lowered flowrate (total flow = 30 ml/min) in a single-stage reactor. However, product yield for gas (14.02 wt%), liquid (53.17%) and solid (15.30 wt %) were similar to experiment-1, 2 and 3, as observed from table 4.5. The liquid and gaseous product distribution for experiment 4 and 5 were similar to the experiment 1, 2, and 3, which will be discussed in section 4.3.1.

	Single-stage				Two-stage
H_2 flow rate (ml/min)	80	80	80	24	80
N_2 flow rate (ml/min)	20	20	20	6	20
Condenser type (RBF)	C-6.1			C-6.3	C-6.1
Condenser medium	Ice				
Product distribution (weight basis)	**Exp-1**	**Exp-2**	**Exp-3**	**Exp-4**	**Exp-5**
Biomass (mg)	450	450	450	600	450
Catalyst	—	—	—	—	—
Solid (wt.%)	15.11	14.89	14.74	15.30	14.34
Gas (wt.%)	14.67	15.28	14.44	13.99	14.02
Liquid (wt.%)	54.11	55.19	54.64	53.17	55.30
Total collected (wt.%)	83.89	85.37	83.83	82.46	83.65
Lost product (wt.%)	16.11	14.63	16.17	17.54	16.35

Table 4.5: Mass balance for single and two-stage non-catalytic hydropyrolysis (temperature = 540-600°C and pressure = 1 bar)

Two-stage Catalytic hydropyrolysis				
H_2 flow rate (ml/min)	24	24	24	24
N_2 flow rate (ml/min)	6	6	6	6
Condenser (RBF/spiral)	C-6.3			C-5
Condenser medium	ice/dewar flask			
Product distribution (weight basis)	**Exp-6**	**Exp-7**	**Exp-8**	**Exp-9**
Biomass (mg)	600	600	600	600
Catalyst	3 wt.% Cu/TiO_2	3 wt.% Cu/TiO_2	1wt.% Ru/TiO_2	1wt.% Ru/TiO_2
Solid wt.%	14.92	15.53	13.54	13.06
Coke wt.%	5.39	4.94	4.88	6.40
Gas wt.%	21.54	20.02	19.01	20.18
Liquid wt.%	39.59	32.99	40.55	48.31
Total collected wt.%	81.44	73.48	77.98	87.96
Lost product (wt.%)	18.56	26.52	22.02	12.04

Table 4.6: Mass balance for non-catalytic hydropyrolysis with ex-situ catalytic up-gradation (temperature: reactor-1 = 540-600°C; reactor-2 = 350°C and pressure =1 bar)

It is worth mentioning that the lower liquid product recovery is not due to condensation at Swagelok union or reactor bottom. The former could not be photo captured since the camera angle and the inner walls of Swagelok union is 0 degree, whereas the latter was photo captured with reasonable picture quality, as shown in figure 4.39. The condensed

fraction is $\leq$ 2 and 3 wt.%, respectively, compared to total biomass input in all the conducted experiments.

The successful validation of the non-catalytic hydropyrolysis led to the testing of the 2-stage ex-situ up-gradation configuration. Table 4.6 shows experiment - 6, 7, 8 and 9 conducted with Ru and Cu based catalyst in an ice-cooled condensing medium. 3 wt.% Cu-TiO_2 catalyst at 30 ml/min and 600 mg was used in experiment 6 and 7. it was observed that char, coke a gas was close to $\approx$ 13, 5 and 20 wt.% whereas the liquid collected was only $\approx$ 40 wt.%. The low liquid yield led to check for the consistency of experiment 6. Unfortunately, the liquid yield dropped by approx 7 wt.% whereas char, coke and gases yield remained similar to experiment 6. It was previously mentioned in section 4 that residence time is higher for spiral condenser compared to RBF based condenser. Therefore, in response to the improvement in the liquid yield and consistency, experiment 8 and 9 was conducted with 1 wt.% Ru-TiO2 in an RBF and spiral condenser, respectively. The char, coke and gas yield was $\approx$ 13, 5 and 20 wt % which is similar to experiment 6 and 7. Interestingly, the liquid yield increased from 40 to 48 wt.% when switching from RBF (C-6.3) to spiral (C-5) condenser. This is 8 wt.% increase in bio-oil recovery. However, the product dilution was an concern with spiral condenser. The product distribution will be discussed in section 4.3.2.

4.3.1 Product distribution of non-catalytic hydropyrolysis experiment

Table 4.7 and 4.8 shows the product distribution of non-catalytic hydropyrolysis at 540-600°C and 1 bar. The CO_2 and CO in fast pyrolysis/hydropyrolysis always dominates among the non-condensable gaseous products [42]. With regards to liquid product, it can be observed that hydroxyacetaldehyde is the major product among the oxygenates. This is due to the degradation of the cellulose fraction of pine wood [42]. Gopakumar et al. conducted hydropyrolysis of pine wood and observed a similar liquid product distribution, as shown in table 4.7. In regards to furan compounds, furfural and furanone were the major products [20]. Unlike cellulose and hemicellulose, phenolics are attributed to its low O/C content and mainly derived from lignin degradation [20]. The main phenolics were cresol, catechol, 1,2-benzenediol, 4-methyl. However, single oxygenated phenol compounds are always lower compared to catalytic hydropyrolysis of pine wood [42]. The commonly found non-catalytic hydropyrolysis oxygen-free aromatic compounds such as benzene, xylene, toluene could not be identified from the GC chromatograms. This might be due to overlapping of the peak of the products with the baseline of the GC chromatogram. Herein, the biomass loading is low compared to hydropyrolysis experiments (10-80 g) conducted with fixed-bed in literature, as mentioned in section 2.7.3. As per section 2.8, only 40% of liquid product is detected by the GC chromatography. In spite of low solvent usage and easier product collection from RBF type condenser compared to other condensers, the RBF condenser still requires optimization to increase its liquid product recovery in the presence of catalyst in reactor-2.

Chemical compounds	FID area (%)
Oxygenates	
Acetaldehyde, hydroxy	5.7
2-Propanone, 1-hydroxy	1.3
2-Hydroxy-3-pentanone	0.9
Acetic acid	5.0
2-Propanone, 1-hydroxy-	4.8
1-Hydroxy-2-butanone	0.7
Succindialdehyde	2.2
2-Cyclopenten-1-one, 2-hydroxy-	3.9
Othes	21.2
Aromatics and Phenolics	
Phenol	1.1
Phenol, 3-methyl-	1.7
Phenol, 2-methoxy-	2.7
Cresol	4.1
Catechol	3.9
Vanillin	1.4
1,2-Benzenediol, 4-methyl-	3.5
others	15.1
Furan derivatives	
Furfural	2.4
2-Furanmethanol	1.6
2(5H)-Furanone	2.2
5-Hydroxymethylfurfural	1.8
2-Furancarboxaldehyde, 5-methyl-	0.9

Table 4.7: Product distribution from non-catalytic hydropyrolsis (Temperature = 540-600 °C and pressure = 1 atm)

Gas compounds	wt.%
CO_2	7.27
CO	6.66
C1-C5	0.05

Table 4.8: Gas composition of non-catalytic hydropyrolysis (Temperature = 540-600 °C and pressure = 1 atm)

4.3.2 Product distribution of ex-situ up-gradation of non-catalytic hydropyrolysis experiment

The liquid product distribution is not reported due to inconsistency in recovery of bio-oil during the ex-situ upgradation of biomass derived oxygenates via C-C coupling catalyst (3 wt.% Cu/TiO_2 and 1 wt.% Ru/TiO_2). However, the physical observation of the bio-oil gave few insights over the C-C coupling catalyst. Firstly, the aqueous fraction of bio-oil increased compared to the non-catalytic hydropyrolysis with no ex-situ up-gradation catalyst. The additional water was formed due to ketonization and aldol condensation reaction. This argument is further confirmed by the appearance of non-homogeneous mixture of bio-oil due to relatively large presence of aqueous fraction in bio-oil. Therefore, additional flushing solvent isopropanol had to be mixed in order to analyze in the GC-MS/FID. The aqueous fraction of bio-oil could not be separated from organic phase by any method mentioned in section 2.8 due to very low loading of biomass compared to the reported biomass loading in literature, as previously mentioned in section 2.7.3 and unavailability of other characterization technique, respectively. In spite of high recovery of bio-oil in C-5 condenser compared to C-6 RBF condenser, high dilution in GC chromatogram was observed due to usage of high quantity of flushing solvent to recover bio-oil.

The effect of C-C coupling catalyst could be seen by comparing the gaseous components between various experiments. The gas yield had shown 5 wt.% increase compared to sole non-catalytic hydropyrolysis, as observed from table 4.6 and 4.5. Further, the increase in aqueous fraction could be supported by the increase in CO_2/CO ratio compared to non-catalytic hydropyrolysis experiment, as shown in table 4.9. The increase in CO_2 is due to the ketonization reaction, which produced CO_2 as a by-product. However, these data should be taken with caution due to uncertainty in one-point calibration of standard gas compound in the GC-TCD/FID detector compared to multi-point calibration. The latter increases the accuracy in quantification of gaseous components. Therefore, the hydrogen consumption is not reported for any experiments conducted in this work.

Setup	Experiment no.	Catalyst	CO_2/CO
Non-catalytic hydropyrolysis (single/two stage)	1-5	-	1.07-1.09
Non-catalytic hydropyrolysis in reactor-1 with ex-situ C-C coupling catalyst placed in reactor-2	6	3 wt.% Cu/TiO_2	1.34
	7	3 wt.% Cu/TiO_2	1.32
	8	1 wt.% Ru/TiO_2	1.29
	9	1 wt.% Ru/TiO_2	1.28

Table 4.9: Comparison of CO_2/CO ratio between non-catalytic hydropyrolysis and ex-situ up-gradation of non-catalytic hydropyrolysis experiment

4.4 Technical difficulties

There were many setbacks faced during the course of the master thesis. These include either modification in the hydropyrolysis setup which was either utilized or made available for future work, technical assistance for the GC instruments etc. Among them, One of the major issues was the of technical assistance and daily time restriction on campus during the corona pandemic. Other issues are as follows:

1) As previously discussed in section 2, Firstly, a separate H_2 gas line (marked as **2** in figure 4.40) was made available to the reactor-2. This was modified for conducting pyrolysis/hydropyrolysis in reactor-1 and hydropyrolysis in reactor-2. In this manner, the comparison of product distribution between the presence of hydrogen in reactor-1 could be studied. Secondly, To understand the effect of a small amount of air in the pyrolysis/hydropyrolysis of biomass, air gas line was made available to the reactor 1. Thirdly, an additional gas inflow route to reactor-1 was made through the gas feeding chamber, as shown in figure 4.40, which is marked as **1**. In this manner, the Nitrogen/hydrogen/air will pass the top zone of the biomass feeding chamber towards the reactor when the ball valve is opened. However, the existing nitrogen sweep gas is still utilized to make the feeding chamber inert.

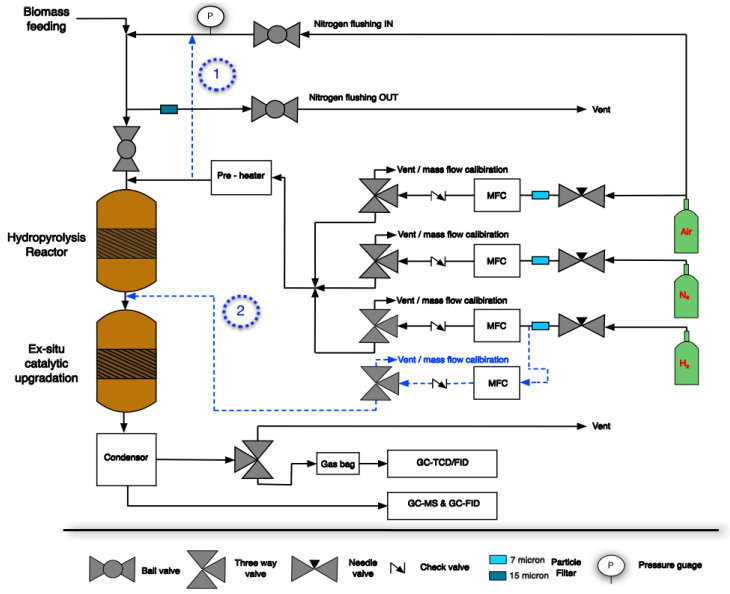

Figure 4.40: Modified flow-sheet for additional gas lines

2) During the initial development of the hydropyrolysis setup, mass flow controller calibration and heating of the oven, flushing of hydrogen from the setup was a challenging task. Initially, the mixing of the hydrogen and nitrogen was accomplished far away from the reactor-1. Despite flushing the reactor with nitrogen (50 ml/min) for two days, the hydrogen gas alarm in the setup went 'ON' on frequent occasions while dismantling the

connection and reactor for washing, after weighing analysis for coke etc. In order to avoid these delays, the gas mixing was accomplished just before the reactor-1 and pre-heater, as shown in figure 4.41. Afterwards, the hydrogen flushing after after each successful experiment was easily flushed with nitrogen in $\approx$ 15 min.

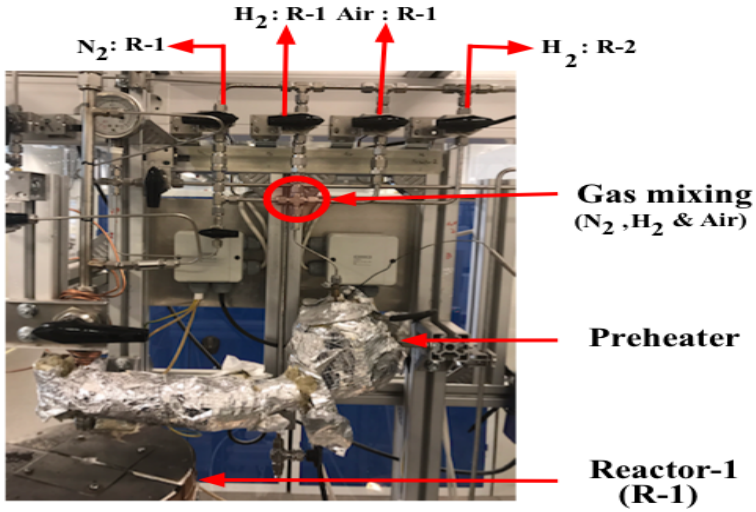

Figure 4.41: Modified gas lines for feasible hydrogen flushing during post-experiment analysis

3) The microsyringe (via autosampler) was utilized for injecting the liquid samples into the GC for liquid analysis. Despite automatic instrument-controlled ethanol wash of the column and microsyringe, multiple needle breakdown was observed during the each consecutive injection in the GC instrument. This is shown in figure 4.42 (a). The issue was overcome by manually washing the microsyringe with ethanol after every post liquid sample injection into the GC. Additionally, the GC injector septa, liner were either contaminated/ damaged during method optimization of liquid products in GC instrument, as shown in figure 4.42 (b).

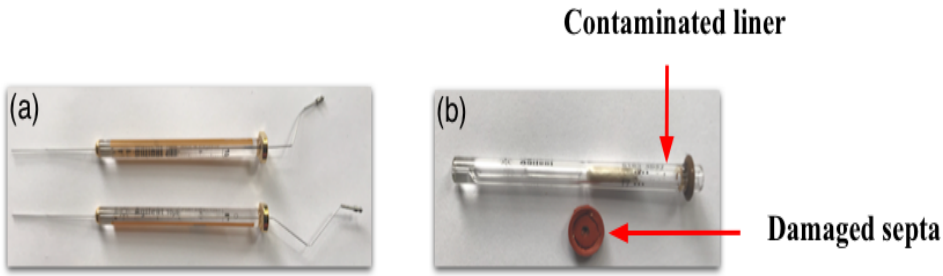

Figure 4.42: Damaged GC parts during experiments

4) The interconnection between the glass and the metal, as shown in figure 4.43, was broken frequently during pre and post dismantling of the reactors for weighing analysis. Two significant issues were the brittle of the interconnection and poor heat resistant above 120°C, respectively.

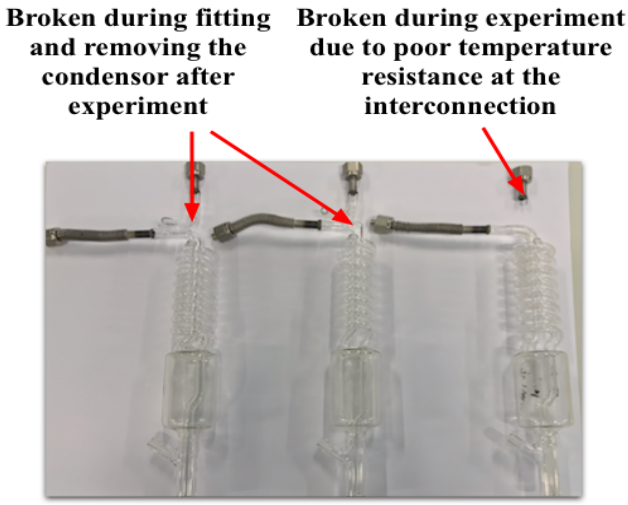

Figure 4.43: Broken spiral condenser during pre/post experiment analysis

6) The metal junction of the spiral condenser which connects to the reactor-1/reactor-2 is frequently bloated due to over-tightening and heat gradient from the reactor, as shown in figure 4.44. Therefore, each spiral based condenser had limited usability and needed a replacement after 2-4 experiments.

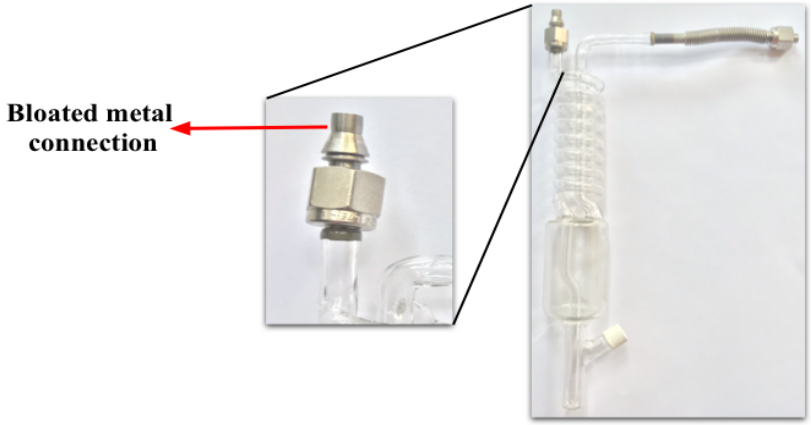

Figure 4.44: Damaged spiral condenser-metal fitting

7) The delay for ordering a new vacuum flask was one of the major setbacks during the course of this work. Unfortunately, the previous vacuum flask was broken during setup modification.

5) The air contamination in the GC lines for gas analysis was an issue. This was overcome by increasing the loading time in the GC analysis method (The GC lines are flushed with the gas collected during the hydropyrolysis experiment). The optimum loading time of 10 seconds is enough to flush the GC sample line.

8) Multiple shutdowns of the setup during experiments either due to hydrogen leak or malfunction of the heating ovens were experienced.

9) Due to time constraints, Ru/C catalyst could not characterized by XRD, NH_3 and CO_2-TPD. However, the BET and SEM data had been presented in this report.

Chapter 5

Conclusion

A fast catalytic screening unit was built and optimized to mimic the large scale continuous biomass feeding operation (H_2-Bio-oil technology) in a semi-batch manner. The experimental setup consisted of two fixed-bed reactors in a series configuration. The non-catalytic hydropyrolysis was conducted in reactor-1, and ex-situ catalytic up-gradation was performed in reactor-2. The biomass was loaded inside three cylindrical mesh (wrapped with 2 mm stainless steel wire) and fed into reactor-1 once the desired temperature was achieved. In this regard, the dimensions of the biomass feeding compartment and reactor-1 were optimized. Next, an optimal location for set-point controlled thermocouple was found to be at bottom and mid-zone of reactor-1 and reactor-2, respectively. The GC-TCD/FID detectors were calibrated for CO_2, CO, N_2, H_2, CH_4, ethane, ethene, propane, propene, butane, butene, pentane and pentene gases based on one-point calibration curve. Unfortunately, the lack of adequate standard chemicals representing the bio-oil components led to semi-quantification of bio-oil based on GC-FID peak area in this work.

The single and two-stage non-catalytic hydropyrolysis experiments were validated exclusively with reactor-1 and combination of both reactor-1 and 2, respectively. The mass balance of solid char (15 wt.%) and gas (15 wt.%) products complied with the existing literature, whereas, liquid yield up to 54 wt.% was observed, which was 70% of the reported value. In response, a total of 8 condensers was designed and tested for high bio-oil recovery. The round bottom flask based condensers were found to be reliable during post-experiment bio-oil collection due to the low bio-oil produced, which is $\approx$ 0.1 ml. In contrast, spiral condensers recovered high quantity on bio-oil (48 wt.%) compared to round bottom flask based condenser (40 wt.%) during ex-situ catalytic up-gradation. However, the product dilution due to large usage of flushing solvent to recover the bio-oil from the spiral condenser was a major concern in both single/two-stage non-catalytic hydropyrolysis and ex-situ up-gradation of the hydropyrolyzed biomass vapours from reactor-1, respectively. The experimental results from the ex-situ catalytic up-gradation configuration could not be validated due to time constraints.

The C-C coupling catalyst, 0.5, 1, 3 and 7 wt.% Cu-TiO_2, 1 wt.% Ru/TiO_2, 1 wt.% Au/TiO_2 and hydrodeoxygenation catalyst, 1 wt.% Ru-MoFeP/Al_2O_3 was synthesized and characterized by SEM, BET, XRD, NH_3 and CO_2 TPD. The prepared catalyst could not be tested with the developed experimental setup, except for 3 wt.% Cu/TiO_2 and 1 wt.% Ru/TiO_2 due to time constraints. The liquid product distribution was not analyzed due to fluctuations in the bio-oil recovery in the designed condensers. However, the C-C coupling catalyst influenced the product distribution by increasing the aqueous fraction and CO_2/CO ratio compared to the non-catalytic hydropyrolysis experiments. This is attributed to the ketonization and aldol condensation reaction. However, the product distribution should be taken with caution since the setup was not validated for ex-situ up-gradation due to limited time.

There is no published literature on the activity of synthesized C-C coupling and hydrodeoxygenation catalyst with real biomass as feedstock. Based on the literature review and characterization, few insights over the catalytic activity can be hypothesized. In spite of relatively low BET surface of the support material TiO_2 ($\approx$ 50 m^2/g) compared to the existing ketonization catalyst over model compounds, the intrinsic nature of reducible oxides can show high activity in the C-C coupling reaction. Further, deposition of a hydrogenating metal such as Cu, Au and Ru could enhance the catalytic activity by creating more oxygen vacancy TiO_2. Herein, unsaturated metal cations (lewis acid) are crucial to stabilizing the two vicinal carboxylate intermediates after the abstraction of the α- hydrogen from the acid molecules by oxides on the surface (Brønsted base) for a successful C-C coupling reaction. Based on the NH_3 and CO_2-TPD, the lewis acidity and (weak+strong) basicity were the highest and lowest for Ru/TiO_2. This characteristic of RuTiO_2 might be enough to outperform in C-C coupling reaction compared to other catalysts. Further, the distribution of Ru over the support TiO_2 is homogeneously distributed, which is confirmed from the SEM and XRD results. In contrast, Au/TiO_2 was observed to be active in C-C coupling compared to Ru/TiO_2 in simulated bio-oil as feedstock, as observed by a former PhD student. However, the difference in the final liquid product distribution from the synthesized C-C coupling catalyst might not be observable due to complex product distribution from real biomass compared to model compounds as feedstock. Similarly, for HDO catalyst, the presence of large lewis acid sites had shown high deoxygenation activity, which otherwise leads to cracking and undesired side reaction in the presence of high Brønsted acid sites. The MoFeP and Ru species was reported to increase the lewis acidity in 1 wt.% Ru-MoFeP/Al_2O_3. Similar to C-C coupling catalyst, the HDO catalysts must be tested in order to compare the catalytic activity.

Overall, the developed experimental setup in this work can be taken as a preliminary design for future optimization for high recovery of bio-oil. The tandem catalytic approach of C-C coupling and hydrodeoxygenation catalyst seems an attractive option for conversion of biomass-derived oxygenates to fuel range chemical compounds (gasoline, diesel, jet fuel). Further, the extensive literature review on the past ten years of atmospheric C-C coupling and HDO study will provide insights on the preparation of the active catalyst.

Chapter 6

Future work

This section will provide a few useful insights on how to improve the two-stage fast catalyst screening unit. The current advantage of the setup is the successful establishment of non-catalytic hydropyrolysis experiments. However, the bio-oil recovery is approx 53 wt.% of the biomass input, which is 70% of the reported value in the literature. The main problems can be condensed as follows; 1) The biomass loading of 600 mg is still considered low due to the losses due to unavoidable condensation prior inlet of the condenser. The is due to the trade-off between residence time of bio-oil vapours and easy product collection in the condenser. 2) This led to low bio-oil recovery from the condenser, thereby less sample available for multiple GC analysis of the liquid products.

The following suggestion could be tried to overcome the aforementioned problems:

1) Low-temperature up to -20°C gives cooling bath an advantage over ice on a higher rate of condensation of bio-oil vapours. The cooling bath should be tested with the developed setup to check if the unreliable bio-oil recovery by ice as a condensing medium could be overcome.

2) The spiral condenser had higher bio-oil recovery compared to RBF condenser during ex-situ catalytic up-gradation of hydropyrolysis vapours. Unfortunately, further experiments could be not be conducted to check for the consistency of the reported data. Therefore, catalytic experiments must be conducted again with spiral condenser and cooling bath as a condensing medium.

3) The char formed in the 1^{st} stage non-catalytic hydropyrolysis reactor is approx 15%. The fixed-bed can operate until the char plugs the flow of sweep gas. Therefore, semi-continuous feeding of biomass could operate the two-stage fixed reactor to produce more bio-oil. This could be accomplished by an hopper and screw feeding device for injecting biomass into the reactor. The higher bio-oil yield can decrease product dilution in GC analysis. However, this approach need many trial experiments to record the maximum biomass loading at which the fixed-bed reactor gets clogged.

4) The RBF and spiral based condenser should be further optimized if the biomass loading is not increased. The former could be modified by increasing the residence time from inlet to the outlet of the condenser. In contrast, the spiral should be reduced in the latter.

5) Large tubing and proper Swagelok fittings of internal diameter 2-4 cm should be utilized for the two-stage reactor setup developed in this work. Therefore, the biomass loading could be increased up to 2-4 grams by designing a corresponding larger diameter cylindrical mesh device for biomass loading.

6) If the biomass loading is increased, the unwanted condensation of the bio-oil prior inlet of the condenser could be avoided. This is accomplished by replacing the glass condenser by metal spiral condenser. Herein, the metal-glass junction which had poor heat resistant characteristic could be overcome. The interconnection could be heated with an external heating coil up to the 2^{nd}-stage reactor temperature, thereby, increasing the product recovery of heavy bio-oil components.

7) Calcium oxide (CaO) can be mixed with C-C coupling catalyst which captures and forms into $CaCO_3$. There are two advantage in this catalyst combination. Firstly, CaO is a basic catalyst which can produce ketones from acid via bulk ketonization pathway. Secondly, the local heat generated during the formation of $CaCO_3$ might aid in improving the product distribution of bio-oil.

8) The GC-TCD/FID for gas analysis should be calibrated using different composition of gas cylinders. The multi-point calibration is more reliable than the single-point calibration of gaseous products. Similarly, GC-MS/FID for liquid analysis must be calibrated for large number of standard chemicals representing bio-oil components.

Bibliography

[1] Paul Adams, Tony Bridgwater, Amanda Lea-Langton, Andrew Ross, and Ian Watson. Biomass conversion technologies. In *Greenhouse Gas Balances of Bioenergy Systems*, pages 107–139. Elsevier, 2018.

[2] Vladislav Lizunkov, Ekaterina Politsinskaya, Elena Malushko, Alexandr Kindaev, and Mikhail Minin. Population of the world and regions as the principal energy consumer. *International journal of energy economics and policy*, 8(3):250–257, 2018.

[3] Bhavya Balagurumurthy and Thallada Bhaskar. Hydropyrolysis of lignocellulosic biomass: state of the art review. *Biomass conversion and biorefinery*, 4(1):67–75, 2014.

[4] Antonio García-Olivares, Jordi Solé, and Oleg Osychenko. Transportation in a 100% renewable energy system. *Energy Conversion and Management*, 158:266–285, 2018.

[5] Bhavya Balagurumurthy, Twinkle S Oza, Thallada Bhaskar, and Dilip Kumar Adhikari. Renewable hydrocarbons through biomass hydropyrolysis process: challenges and opportunities. *Journal of Material Cycles and Waste Management*, 15(1):9–15, 2013.

[6] Michael W Nolte and Brent H Shanks. A perspective on catalytic strategies for deoxygenation in biomass pyrolysis. *Energy Technology*, 5(1):7–18, 2017.

[7] Martin Stas, David Kubicka, Josef Chudoba, and Milan Pospísil. Overview of analytical methods used for chemical characterization of pyrolysis bio-oil. *Energy & Fuels*, 28(1):385–402, 2014.

[8] Georg Feulner. The future of earth's climate after paris. In *International Climate Protection*, pages 5–11. Springer, 2019.

[9] Shanshan Shao, Xianliang Xiang, Xiaohua Li, Huiyan Zhang, Rui Xiao, and Yixi Cai. Synergy in the selective production of ketone platform compounds from

biomass pyrolysis vapors over CeO_2 catalysts. *Industrial & Engineering Chemistry Research*, 59(14):6460–6469, 2020.

[10] Kishore Rajendran. Catalytic conversion of biomass derived oxygenates to fuels and chemicals (H_2-bio-oil). Technical report.

[11] Guanqun Luo, Fernanco Resende, and Todd A Murray. Bio-oil: an introduction to fast pyrolysis and its applications. 2014.

[12] RV Pindoria, IN Chatzakis, J-Y Lim, AA Herod, DR Dugwell, and R Kandiyoti. Hydropyrolysis of sugar cane bagasse: effect of sample configuration on bio-oil yields and structures from two bench-scale reactors. *Fuel*, 78(1):55–63, 1999.

[13] Fernando LP Resende. Recent advances on fast hydropyrolysis of biomass. *Catalysis Today*, 269:148–155, 2016.

[14] Hongzhang Chen. Biotechnology of lignocellulose. *Theory and Practice. China: Chemical Industry Press and Springer*, 2014.

[15] Mayra Melián Rodríguez. Lignin biomass conversion into chemicals and fuels. 2016.

[16] Furkan H Isikgor and C Remzi Becer. Lignocellulosic biomass: a sustainable platform for the production of bio-based chemicals and polymers. *Polymer Chemistry*, 6(25):4497–4559, 2015.

[17] Michael B Griffin, Kristiina Iisa, Huamin Wang, Abhijit Dutta, Kellene A Orton, Richard J French, Daniel M Santosa, Nolan Wilson, Earl Christensen, Connor Nash, et al. Driving towards cost-competitive biofuels through catalytic fast pyrolysis by rethinking catalyst selection and reactor configuration. *Energy & Environmental Science*, 11(10):2904–2918, 2018.

[18] Ashok Pandey, Thallada Bhaskar, Michael Stöcker, and Rajeev Sukumaran. *Recent advances in thermochemical conversion of biomass*. Elsevier, 2015.

[19] Qi Zhang, Jie Chang, Tiejun Wang, and Ying Xu. Review of biomass pyrolysis oil properties and upgrading research. *Energy conversion and management*, 48(1):87–92, 2007.

[20] Suchithra Thangalazhy-Gopakumar, Sushil Adhikari, Ram B Gupta, Maobing Tu, and Steven Taylor. Production of hydrocarbon fuels from biomass using catalytic pyrolysis under helium and hydrogen environments. *Bioresource technology*, 102(12):6742–6749, 2011.

[21] Theodore Dickerson and Juan Soria. Catalytic fast pyrolysis: a review. *Energies*, 6(1):514–538, 2013.

[22] Dinesh Mohan, Charles U Pittman Jr, and Philip H Steele. Pyrolysis of wood/biomass for bio-oil: a critical review. *Energy & fuels*, 20(3):848–889, 2006.

[23] M Verma, S Godbout, SK Brar, O Solomatnikova, SP Lemay, and JP Larouche. Biofuels production from biomass by thermochemical conversion technologies. *International Journal of Chemical Engineering*, 2012, 2012.

[24] Anthony V Bridgwater and G Grassi. *Biomass pyrolysis liquids upgrading and utilization*. Springer Science & Business Media, 2012.

[25] AJ Güell, CZ Li, AA Herod, BJ Stokes, P Hancock, and R Kandiyot. Effect of H_2-pressure on the structures of bio-oils from the mild hydropyrolysis of biomass. *Biomass and Bioenergy*, 5(2):155–171, 1993.

[26] Meyer Steinberg, Peter T Fallon, and MS Sundaram. Flash pyrolysis of biomass with reactive and non-reactive gas. *Biomass*, 9(4):293–315, 1986.

[27] J Dilcio Rocha, Carlos A Luengo, and Colin E Snape. The scope for generating bio-oils with relatively low oxygen contents via hydropyrolysis. *Organic Geochemistry*, 30(12):1527–1534, 1999.

[28] Meyer Steinberg. The flash hydropyrolysis and methanolysis of coal with hydrogen and methane. In *Hydrogen Systems*, pages 257–285. Elsevier, 1986.

[29] David P Gamliel, Laura Wilcox, and Julia A Valla. The effects of catalyst properties on the conversion of biomass via catalytic fast hydropyrolysis. *Energy & Fuels*, 31(1):679–687, 2017.

[30] Metta Chareonpanich, Tippanakarin Boonfueng, and Jumras Limtrakul. Production of aromatic hydrocarbons from mae-moh lignite. *Fuel Processing Technology*, 79(2):171–179, 2002.

[31] M Canel, Z Mısırlıogˇlu, and A Sınagˇ. Hydropyrolysis of a turkish lignite (tunçbilek) and effect of temperature and pressure on product distribution. *Energy Conversion and Management*, 46(13-14):2185–2197, 2005.

[32] Meyer Steinberg. The flash hydropyrolysis and methanolysis of coal with hydrogen and methane. In *Hydrogen Systems*, pages 257–285. Elsevier, 1986.

[33] Trine MH Dabros, Magnus Zingler Stummann, Martin Høj, Peter Arendt Jensen, Jan-Dierk Grunwaldt, Jostein Gabrielsen, Peter M Mortensen, and Anker Degn Jensen. Transportation fuels from biomass fast pyrolysis, catalytic hydrodeoxygenation, and catalytic fast hydropyrolysis. *Progress in Energy and Combustion Science*, 68:268–309, 2018.

[34] MZ Stummann, M Høj, B Davidsen, AB Hansen, LP Hansen, P Wiwel, CB Schandel, J Gabrielsen, PA Jensen, and AD Jensen. Effect of the catalyst in fluid bed catalytic hydropyrolysis. *Catalysis Today*, 2019.

[35] Calvin Mukarakate, Xiaodong Zhang, Alexander R Stanton, David J Robichaud, Peter N Ciesielski, Kara Malhotra, Bryon S Donohoe, Erica Gjersing, Robert J Evans, David S Heroux, et al. Real-time monitoring of the deactivation of HZSM-5 during upgrading of pine pyrolysis vapors. *Green Chemistry*, 16(3):1444–1461, 2014.

[36] Oliver Jan, Ryan Marchand, Luiz CA Anjos, Gabriel VS Seufitelli, Eranda Nikolla, and Fernando LP Resende. Hydropyrolysis of lignin using Pd/HZSM-5. *Energy & Fuels*, 29(3):1793–1800, 2015.

[37] Devin S Chandler and Fernando LP Resende. Comparison between catalytic fast pyrolysis and catalytic fast hydropyrolysis for the production of liquid fuels in a fluidized bed reactor. *Energy & Fuels*, 33(4):3199–3209, 2019.

[38] J Dilcio Rocha, Carlos A Luengo, and Colin E Snape. The scope for generating bio-oils with relatively low oxygen contents via hydropyrolysis. *Organic Geochemistry*, 30(12):1527–1534, 1999.

[39] MZ Stummann, M Høj, CB Schandel, AB Hansen, P Wiwel, J Gabrielsen, PA Jensen, and AD Jensen. Hydrogen assisted catalytic biomass pyrolysis. effect of temperature and pressure. *Biomass and Bioenergy*, 115:97–107, 2018.

[40] Terry L Marker, Larry G Felix, Martin B Linck, and Michael J Roberts. Integrated hydropyrolysis and hydroconversion (IH^2) for the direct production of gasoline and diesel fuels or blending components from biomass, part 1: Proof of principle testing. *Environmental Progress & Sustainable Energy*, 31(2):191–199, 2012.

[41] Rakesh Agrawal and Navneet R Singh. Synergistic routes to liquid fuel for a petroleum-deprived future. *AIChE journal*, 55(7):1898–1905, 2009.

[42] Trine MH Dabros, Magnus Zingler Stummann, Martin Høj, Peter Arendt Jensen, Jan-Dierk Grunwaldt, Jostein Gabrielsen, Peter M Mortensen, and Anker Degn Jensen. Transportation fuels from biomass fast pyrolysis, catalytic hydrodeoxygenation, and catalytic fast hydropyrolysis. *Progress in Energy and Combustion Science*, 68:268–309, 2018.

[43] Bhavya B Krishna, Bijoy Biswas, Priyanka Ohri, Jitendra Kumar, Rawel Singh, and Thallada Bhaskar. Pyrolysis of cedrus deodara saw mill shavings in hydrogen and nitrogen atmosphere for the production of bio-oil. *Renewable Energy*, 98:238–244, 2016.

[44] Harshal D Kawale and Nanda Kishore. Production of hydrocarbons from a green algae (Oscillatoria) with exploration of its fuel characteristics over different reaction atmospheres. *Energy*, 178:344–355, 2019.

[45] Shule Wang, Henry Persson, Weihong Yang, and Par Goran Jonsson. Effect of H_2 as pyrolytic agent on the product distribution during catalytic fast pyrolysis of biomass using zeolites. *Energy & Fuels*, 32(8):8530–8536, 2018.

[46] Bhavya Balagurumurthy, Thallada Bhaskar, KLN Shiva Kumar, Hari Bhagwan Goyal, and Dilip Kumar Adhikari. Effect of pressure on the hydropyrolysis of jatropha seed deoiled cake. *Journal of Material Cycles and Waste Management*, 15(3):328–334, 2013.

[47] Bhavya Balagurumurthy, Rawel Singh, Twinkle S Oza, KLN Shiva Kumar, Sandeep Saran, GM Bahuguna, RK Chauhan, and Thallada Bhaskar. Effect of pressure and

temperature on the hydropyrolysis of cotton residue. *Journal of Material Cycles and Waste Management*, 16(3):442–448, 2014.

[48] Jie Zhang, Nan Zheng, and Jie Wang. Comparative investigation of rice husk, thermoplastic bituminous coal and their blends in production of value-added gaseous and liquid products during hydropyrolysis/co-hydropyrolysis. *Bioresource technology*, 268:445–453, 2018.

[49] Sirimirin Meesuk, Jing-Pei Cao, Kazuyoshi Sato, Yukiko Ogawa, and Takayuki Takarada. Study of catalytic hydropyrolysis of rice husk under nickel-loaded brown coal char. *Energy & fuels*, 25(11):5438–5443, 2011.

[50] Shaolong Wan, Trung Pham, Sarah Zhang, Lance Lobban, Daniel Resasco, and Richard Mallinson. Direct catalytic upgrading of biomass pyrolysis vapors by a dual function Ru/TiO_2 catalyst. *AIChE Journal*, 59(7):2275–2285, 2013.

[51] Eleni F Iliopoulou. Review of CC coupling reactions in biomass exploitation processes. *Current Organic Synthesis*, 7(6):587–598, 2010.

[52] Tu N Pham, Tawan Sooknoi, Steven P Crossley, and Daniel E Resasco. Ketonization of carboxylic acids: mechanisms, catalysts, and implications for biomass conversion. *Acs Catalysis*, 3(11):2456–2473, 2013.

[53] Tetiana Kulik, Borys Palianytsia, and Mats Larsson. Catalytic pyrolysis of aliphatic carboxylic acids into symmetric ketones over ceria-based catalysts: Kinetics, isotope effect and mechanism. *Catalysts*, 10(2):179, 2020.

[54] Huajuan Ling, Zichun Wang, Leizhi Wang, Catherine Stampfl, Dan Wang, Jianfeng Chen, and Jun Huang. Composition-structure-function correlation of $Ca/Zn/AlO_x$ catalysts for the ketonization of acetic acid. *Catalysis Today*, 351:58–67, 2020.

[55] Raj Kumar Dahal, Omid Norouzi, Jesse Cameron, Arun Pandian, Ankita Shrestha, Bishnu Acharya, PK Srividya, and Animesh Dutta. A study on potential recovery of energy and value-added chemicals from in-situ pyrolysis of bambusa balcooa over basic metal oxides. *Journal of Analytical and Applied Pyrolysis*, page 104801, 2020.

[56] Alexey V Ignatchenko. Multiscale approach for the optimization of ketones production from carboxylic acids by the decarboxylative ketonization reaction. *Catalysis Today*, 2019.

[57] Alexey V Ignatchenko and Evguenii I Kozliak. Distinguishing enolic and carbonyl components in the mechanism of carboxylic acid ketonization on monoclinic zirconia. *ACS Catalysis*, 2(8):1555–1562, 2012.

[58] Osamu Nagashima, Satoshi Sato, Ryoji Takahashi, and Toshiaki Sodesawa. Ketonization of carboxylic acids over CeO_2-based composite oxides. *Journal of Molecular Catalysis A: Chemical*, 227(1-2):231–239, 2005.

[59] GAH Mekhemer, SA Halawy, MA Mohamed, and MI Zaki. Ketonization of acetic acid vapour over polycrystalline magnesia: in situ fourier transform infrared spectroscopy and kinetic studies. *Journal of Catalysis*, 230(1):109–122, 2005.

[60] Marcel Schlaf and Z Conrad Zhang. *Reaction pathways and mechanisms in thermocatalytic biomass conversion I: Cellulose structure, depolymerization and conversion by heterogeneous catalysts*. Springer, 2015.

[61] ST Almutairi, EF Kozhevnikova, and IV Kozhevnikov. Ketonisation of acetic acid on metal oxides: Catalyst activity, stability and mechanistic insights. *Applied Catalysis A: General*, 565:135–145, 2018.

[62] Binbo Jiang, Zhixiang Xi, Feipeng Lu, Zhengliang Huang, Yao Yang, Jingyuan Sun, Zuwei Liao, Jingdai Wang, and Yongrong Yang. Ce/MgAl mixed oxides derived from hydrotalcite LDH precursors as highly efficient catalysts for ketonization of carboxylic acid. *Catalysis Science & Technology*, 9(22):6335–6344, 2019.

[63] Rawesh Kumar, Nagasuresh Enjamuri, Sneha Shah, Ahmed Sadeq Al-Fatesh, Juan J Bravo-Suárez, and Biswajit Chowdhury. Ketonization of oxygenated hydrocarbons on metal oxide based catalysts. *Catalysis Today*, 302:16–49, 2018.

[64] Jia Wang, Chao Xu, Zhaoping Zhong, Aidong Deng, Naijia Hao, Mi Li, Xianzhi Meng, and Arthur J Ragauskas. Catalytic conversion of bamboo sawdust over ZrO_2–CeO_2/γ-Al_2O_3 to produce ketonic hydrocarbon precursors and furans. *ACS Sustainable Chemistry & Engineering*, 6(11):13797–13806, 2018.

[65] Gianfranco Pacchioni. Ketonization of carboxylic acids in biomass conversion over TiO_2 and ZrO_2 surfaces: a DFT perspective. *ACS Catalysis*, 4(9):2874–2888, 2014.

[66] Yafen Zhang, David R Mullins, and Aditya Savara. Effect of Sr substitution in $LaMnO_3$ (100) on catalytic conversion of acetic acid to ketene and combustion-like products. *The Journal of Physical Chemistry C*, 123(7):4148–4157, 2019.

[67] Jing Zhang, Yong S Choi, and Brent H Shanks. Tailoring the composition of bio-oil by vapor-phase removal of organic acids. *ChemSusChem*, 8(24):4256–4265, 2015.

[68] Eleni Heracleous, Dong Gu, Ferdi Schüth, James A Bennett, Mark A Isaacs, Adam F Lee, Karen Wilson, and Angelos A Lappas. Bio-oil upgrading via vapor-phase ketonization over nanostructured FeO_x and MnO_x : Catalytic performance and mechanistic insight. *Biomass Conversion and Biorefinery*, 7(3):319–329, 2017.

[69] Sergio Tosoni, Hsin-Yi Tiffany Chen, Antonio Ruiz Puigdollers, and Gianfranco Pacchioni. TiO_2 and ZrO_2 in biomass conversion: why catalyst reduction helps. *Philosophical Transactions of the Royal Society A: Mathematical, Physical and Engineering Sciences*, 376(2110):20170056, 2018.

[70] Taiwo Omotoso, Sunya Boonyasuwat, and Steven P Crossley. Understanding the role of TiO_2 crystal structure on the enhanced activity and stability of Ru/TiO_2 catalysts for the conversion of lignin-derived oxygenates. *Green Chemistry*, 16(2):645–652, 2014.

[71] Javier Fermoso, Patricia Pizarro, Juan M Coronado, and David P Serrano. Advanced biofuels production by upgrading of pyrolysis bio-oil. *Wiley Interdisciplinary Reviews: Energy and Environment*, 6(4):e245, 2017.

[72] Hossein Bayahia, Elena F Kozhevnikova, and Ivan V Kozhevnikov. Ketonisation of carboxylic acids over Zn-Cr oxide in the gas phase. *Applied Catalysis B: Environmental*, 165:253–259, 2015.

[73] M Gliński, G Zalewski, E Burno, and A Jerzak. Catalytic ketonization over metal oxide catalysts. xiii. comparative measurements of activity of oxides of 32 chemical elements in ketonization of propanoic acid. *Applied Catalysis A: General*, 470:278–284, 2014.

[74] Hossein Bayahia, Elena Kozhevnikova, and Ivan Kozhevnikov. High catalytic activity of silicalite in gas-phase ketonisation of propionic acid. *Chemical Communications*, 49(37):3842–3844, 2013.

[75] Bartosz Rozmysłowicz, Jher Hau Yeap, Ahmed MI Elkhaiary, Masoud Talebi Amiri, Robert L Shahab, Ydna M Questell-Santiago, Charilaos Xiros, Benjamin P Le Monnier, Michael H Studer, and Jeremy S Luterbacher. Catalytic valorization of the acetate fraction of biomass to aromatics and its integration into the carboxylate platform. *Green Chemistry*, 21(10):2801–2809, 2019.

[76] Rebecca AL Baylon, Junming Sun, Libor Kovarik, Mark Engelhard, Houqian Li, Austin D Winkelman, and Yong Wang. Structural identification of $Zn_xZr_yO_z$ catalysts for cascade aldolization and self-deoxygenation reactions. *Applied Catalysis B: Environmental*, 234:337–346, 2018.

[77] Alberto Veses, Begona Puertolas, Jose Manuel Lopez, María Soledad Callen, Benjamín Solsona, and Tomas Garcia. Promoting deoxygenation of bio-oil by metal-loaded hierarchical ZSM-5 zeolites. *ACS Sustainable Chemistry & Engineering*, 4(3):1653–1660, 2016.

[78] Wenchao Ma, Bin Liu, Xiang Ji, Xiangping Li, Beibei Yan, Zhanjun Cheng, and Guanyi Chen. Catalytic co-cracking of distilled bio-oil and ethanol over Ni-ZSM-5/MCM-41 in a fixed-bed. *Biomass and Bioenergy*, 102:31–36, 2017.

[79] Dieni Mansur, Takuya Yoshikawa, Koyo Norinaga, Jun-ichiro Hayashi, Teruoki Tago, and Takao Masuda. Production of ketones from pyroligneous acid of woody biomass pyrolysis over an iron-oxide catalyst. *Fuel*, 103:130–134, 2013.

[80] Mi Lu, Andrew W Lepore, Jae-Soon Choi, Zhenglong Li, Zili Wu, Felipe Polo-Garzon, and Michael Z Hu. Acetic acid/propionic acid conversion on metal doped molybdenum carbide catalyst beads for catalytic hot gas filtration. *Catalysts*, 8(12):643, 2018.

[81] Aqeel Ahmad Taimoor, Alain Favre-Reguillon, Laurent Vanoye, and Isabelle Pitault. Upgrading of biomass transformation residue: influence of gas flow composition on acetic acid ketonic condensation. *Catalysis Science & Technology*, 2(2):359–363, 2012.

[82] James A Bennett, Christopher MA Parlett, Mark A Isaacs, Lee J Durndell, Luca Olivi, Adam F Lee, and Karen Wilson. Acetic acid ketonization over Fe_3O_4/SiO_2 for pyrolysis bio-oil upgrading. *ChemCatChem*, 9(9):1648–1654, 2017.

[83] Justin Weber, Aaron Thompson, Jared Wilmoth, Vidya S Batra, Nida Janulaitis, and James R Kastner. Effect of metal oxide redox state in red mud catalysts on ketonization of fast pyrolysis oil derived oxygenates. *Applied Catalysis B: Environmental*, 241:430–441, 2019.

[84] Changjun Liu, Ayman M Karim, Vanessa M Lebarbier, Donghai Mei, and Yong Wang. Vapor phase ketonization of acetic acid on ceria based metal oxides. *Topics in Catalysis*, 56(18-20):1782–1789, 2013.

[85] Sikander H Hakim, Brent H Shanks, and James A Dumesic. Catalytic upgrading of the light fraction of a simulated bio-oil over $CeZrO_x$ catalyst. *Applied Catalysis B: Environmental*, 142:368–376, 2013.

[86] Feipeng Lu, BinBo Jiang, Jingdai Wang, Zhengliang Huang, Zuwei Liao, Yongrong Yang, and Jie Zheng. Promotional effect of Ti doping on the ketonization of acetic acid over a CeO_2 catalyst. *RSC advances*, 7(36):22017–22026, 2017.

[87] Tu N Pham, Dachuan Shi, and Daniel E Resasco. Kinetics and mechanism of ketonization of acetic acid on Ru/TiO_2 catalyst. *Topics in Catalysis*, 57(6-9):706–714, 2014.

[88] Konstantinos G Kalogiannis, SD Stefanidis, SA Karakoulia, KS Triantafyllidis, Haris Yiannoulakis, C Michailof, and AA Lappas. First pilot scale study of basic vs acidic catalysts in biomass pyrolysis: deoxygenation mechanisms and catalyst deactivation. *Applied Catalysis B: Environmental*, 238:346–357, 2018.

[89] SD Stefanidis, SA Karakoulia, KG Kalogiannis, EF Iliopoulou, A Delimitis, H Yiannoulakis, T Zampetakis, AA Lappas, and KS Triantafyllidis. Natural magnesium oxide (MgO) catalysts: a cost-effective sustainable alternative to acid zeolites for the in situ upgrading of biomass fast pyrolysis oil. *Applied Catalysis B: Environmental*, 196:155–173, 2016.

[90] Mahzad Yaghmaei Sabegh, Omid Norouzi, Sajedeh Jafarian, Ahmad Tavasoli, et al. Pyrolysis of marine biomass to produce bio-oil and its upgrading using a novel multi-metal catalyst prepared from the spent car catalytic converter. *Bioresource technology*, 249:473–478, 2018.

[91] V Anand, Ribhu Gautam, and R Vinu. Non-catalytic and catalytic fast pyrolysis of schizochytrium limacinum microalga. *Fuel*, 205:1–10, 2017.

[92] Shuang Ding, Jiankang Zhao, and Qiang Yu. Effect of zirconia polymorph on vapor-phase ketonization of propionic acid. *Catalysts*, 9(9):768, 2019.

[93] Jianpeng Cao, Shuang Ding, Hua Wang, Jinyu Han, Qingfeng Ge, and Xinli Zhu. Conversion of C_{2-4} carboxylic acids to hydrocarbons on HZSM-5: Effect of carbon chain length. *Industrial & Engineering Chemistry Research*, 58(24):10307–10316, 2019.

[94] AC Psarras, CM Michailof, EF Iliopoulou, KG Kalogiannis, AA Lappas, E Heracleous, and KS Triantafyllidis. Acetic acid conversion reactions on basic and acidic catalysts under biomass fast pyrolysis conditions. *Molecular Catalysis*, 465:33–42, 2019.

[95] Antonie Castille, Claudie Bessette, Francois Thomas, and Mania Etemad. Sustainable hydrocarbon production via simultaneous condensation-hydrodeoxygenation of propionic acid with furfural over red mud-supported noble metal catalysts. *Catalysis Communications*, 121:5–10, 2019.

[96] Hessam Jahangiri, Amin Osatiashtiani, Miloud Ouadi, Andreas Hornung, Adam F Lee, and Karen Wilson. Ga/HZSM-5 catalysed acetic acid ketonisation for upgrading of biomass pyrolysis vapours. *Catalysts*, 9(10):841, 2019.

[97] Feipeng Lu, BinBo Jiang, Jingdai Wang, Zhengliang Huang, Zuwei Liao, and Yongrong Yang. Insights into the improvement effect of Fe doping into the CeO_2 catalyst for vapor phase ketonization of carboxylic acids. *Molecular Catalysis*, 444:22–33, 2018.

[98] Hossein Bayahia. Gas-phase ketonization of acetic acid over Co–Mo and its supported catalysts. *Journal of Taibah University for Science*, 12(2):191–196, 2018.

[99] Michael A Jackson. Ketonization of model pyrolysis bio-oil solutions in a plug-flow reactor over a mixed oxide of Fe, Ce, and Al. *Energy & fuels*, 27(7):3936–3943, 2013.

[100] Hector Hernando, Begona Puertolas, Patricia Pizarro, Javier Fermoso, Javier Perez-Ramirez, and David P Serrano. Cascade deoxygenation process integrating acid and base catalysts for the efficient production of second-generation biofuels. *ACS Sustainable Chemistry & Engineering*, 7(21):18027–18037, 2019.

[101] Beatriz Valle, Naiara García-Gómez, Aingeru Remiro, Ana G Gayubo, and Javier Bilbao. Cost-effective upgrading of biomass pyrolysis oil using activated dolomite as a basic catalyst. *Fuel Processing Technology*, 195:106142, 2019.

[102] James E Rekoske and Mark A Barteau. Kinetics, selectivity, and deactivation in the aldol condensation of acetaldehyde on anatase titanium dioxide. *Industrial & engineering chemistry research*, 50(1):41–51, 2011.

[103] Mai M Khalaf and Antar A Abdelhamid. Sol–gel derived mixed oxide zirconia: titania green heterogeneous catalysts and their performance in acridine derivatives synthesis. *Catalysis Letters*, 146(3):645–655, 2016.

[104] Kumar Ranjan Routb Xiang Feng Wenzhao Fu Xuezhi Duan Isaac Yeboah, Yahao Li and De Chen. Multi-functional catalysts induced tandem reactions for simulated-bio-oil upgrading to jet-fuel range hydrocarbons. Technical report.

[105] M Zamora, T López, M Asomoza, R Meléndrez, and R Gómez. Alkaline doped TiO_2 sol–gel catalysts: Effect of sintering on catalyst activity and selectivity for acetone condensation. *Catalysis today*, 116(2):234–238, 2006.

[106] Daolai Sun, Shizuka Moriya, Yasuhiro Yamada, and Satoshi Sato. Vapor-phase self-aldol condensation of butanal over Ag-modified TiO_2. *Applied Catalysis A: General*, 524:8–16, 2016.

[107] Anirudhan Gangadharan, Min Shen, Tawan Sooknoi, Daniel E Resasco, and Richard G Mallinson. Condensation reactions of propanal over $Ce_xZr_{1-x}O_2$ mixed oxide catalysts. *Applied Catalysis A: General*, 385(1-2):80–91, 2010.

[108] Elif I Gürbüz, Edward L Kunkes, and James A Dumesic. Dual-bed catalyst system for C-C coupling of biomass-derived oxygenated hydrocarbons to fuel-grade compounds. *Green Chemistry*, 12(2):223–227, 2010.

[109] Jinfan Yang, Shanshan Li, Leilei Zhang, Xiaoyan Liu, Junhu Wang, Xiaoli Pan, Ning Li, Aiqin Wang, Yu Cong, Xiaodong Wang, et al. Hydrodeoxygenation of furans over Pd-FeO_x/SiO_2 catalyst under atmospheric pressure. *Applied Catalysis B: Environmental*, 201:266–277, 2017.

[110] Zhan Si, Xinghua Zhang, Chenguang Wang, Longlong Ma, and Renjie Dong. An overview on catalytic hydrodeoxygenation of pyrolysis oil and its model compounds. *Catalysts*, 7(6):169, 2017.

[111] Sang Dinh Ngo, Thi Tuong Vi Tran, Suwadee Kongparakul, Prasert Reubroycharoen, Pinit Kidkhuntod, Narong Chanlek, Jing Wang, Guoqing Guan, and Chanatip Samart. Catalytic pyrolysis of napier grass with nickel-copper core-shell bifunctional catalyst. *Journal of Analytical and Applied Pyrolysis*, 145:104745, 2020.

[112] Zhiyu Li, Enchen Jiang, Xiwei Xu, Yan Sun, and Ren Tu. Hydrodeoxygenation of phenols, acids, and ketones as model bio-oil for hydrocarbon fuel over Ni-based catalysts modified by Al, La and Ga. *Renewable Energy*, 146:1991–2007, 2020.

[113] María Soledad Zanuttini, Bruno Oscar Dalla Costa, Carlos Alberto Querini, and María Ariela Peralta. Hydrodeoxygenation of m-cresol with Pt supported over mild acid materials. *Applied Catalysis A: General*, 482:352–361, 2014.

[114] Ji Daoyu, Liu Di, Zhang Zongliang, Xu Dongmei, and Gao Peng. Bulk Ni-Mo composites prepared by solid reaction method and their hydrodeoxygenation performance. *China Petroleum Processing & Petrochemical Technology*, 20(3):73–77, 2018.

[115] Tao He, Xinxin Liu, Yuanzheng Ge, Dezhi Han, Jianqing Li, Zhiqi Wang, and Jinhu Wu. Gas phase hydrodeoxygenation of anisole and guaiacol to aromatics with a high selectivity over Ni-Mo/SiO_2. *Catalysis Communications*, 102:127–130, 2017.

[116] Matthew M Yung, Guo Shiou Foo, and Carsten Sievers. Role of Pt during hydrodeoxygenation of biomass pyrolysis vapors over Pt/hbea. *Catalysis Today*, 302:151–160, 2018.

[117] Guo Shiou Foo, Allyson K Rogers, Matthew M Yung, and Carsten Sievers. Steric effect and evolution of surface species in the hydrodeoxygenation of bio-oil model compounds over Pt/HBEA. *ACS Catalysis*, 6(2):1292–1307, 2016.

[118] Jie Zhang, Chengcheng Zhao, Chuang Li, Shenggang Li, Chi-Wing Tsang, and Changhai Liang. The role of oxophilic mo species in Pt/MgO catalysts as extremely active sites for enhanced hydrodeoxygenation of dibenzofuran. *Catalysis Science & Technology*, 10(9):2948–2960, 2020.

[119] Junming Sun, Ayman M Karim, He Zhang, Libor Kovarik, Xiaohong Shari Li, Alyssa J Hensley, Jean-Sabin McEwen, and Yong Wang. Carbon-supported bimetallic Pd–Fe catalysts for vapor-phase hydrodeoxygenation of guaiacol. *Journal of Catalysis*, 306:47–57, 2013.

[120] KA Resende, FB Noronha, and CE Hori. Hydrodeoxygenation of phenol over metal supported niobia catalysts. *Renewable Energy*, 149:198–207, 2020.

[121] Sudhakar Pichaikaran and Pandurangan Arumugam. Vapour phase hydrodeoxygenation of anisole over ruthenium and nickel supported mesoporous aluminosilicate. *Green Chemistry*, 18(9):2888–2899, 2016.

[122] Yongchun Hong, He Zhang, Junming Sun, Karim M Ayman, Alyssa JR Hensley, Meng Gu, Mark H Engelhard, Jean-Sabin McEwen, and Yong Wang. Synergistic catalysis between Pd and Fe in gas phase hydrodeoxygenation of m-cresol. *ACS Catalysis*, 4(10):3335–3345, 2014.

[123] Sunya Boonyasuwat, Taiwo Omotoso, Daniel E Resasco, and Steven P Crossley. Conversion of guaiacol over supported Ru catalysts. *Catalysis letters*, 143(8):783–791, 2013.

[124] Pouya Sirous-Rezaei, Jungho Jae, Jeong-Myeong Ha, Chang Hyun Ko, Ji Man Kim, Jong-Ki Jeon, and Young-Kwon Park. Mild hydrodeoxygenation of phenolic lignin model compounds over a $FeReO_x/ZrO_2$ catalyst: Zirconia and rhenium oxide as efficient dehydration promoters. *Green Chemistry*, 20(7):1472–1483, 2018.

[125] Sarah M Schimming, Onaje D LaMont, Michael Koenig, Allyson K Rogers, Andrew D D'Amico, Matthew M Yung, and Carsten Sievers. Hydrodeoxygenation of guaiacol over ceria–zirconia catalysts. *ChemSusChem*, 8(12):2073–2083, 2015.

[126] Sadia Afrin and Praveen Bollini. Cerium oxide catalyzes the selective vapor-phase hydrodeoxygenation of anisole to benzene at ambient pressures of hydrogen. *Industrial & Engineering Chemistry Research*, 58(31):14603–14607, 2019.

[127] Yujian Wu, Xiwei Xu, Yan Sun, Enchen Jiang, Xudong Fan, Ren Tu, and Jiamin Wang. Gas-phase hydrodeoxygenation of guaiacol over Ni-based husy zeolite catalysts under atmospheric H_2 pressure. *Renewable Energy*, 152:1380–1390, 2020.

[128] Surapas Sitthisa and Daniel E Resasco. Hydrodeoxygenation of furfural over supported metal catalysts: a comparative study of Cu, Pd and Ni. *Catalysis letters*, 141(6):784–791, 2011.

[129] Xiaofei Wang and Jixiang Chen. Effects of indium on Ni/SiO_2 catalytic performance in hydrodeoxygenation of anisole as model bio-oil compound: Suppression of benzene ring hydrogenation and C–C bond hydrogenolysis. *Chinese Journal of Catalysis*, 38(11):1818–1830, 2017.

[130] Jia Wang, Bo Zhang, Zhaoping Zhong, Kuan Ding, Aidong Deng, Min Min, Paul Chen, and Roger Ruan. Catalytic fast co-pyrolysis of bamboo residual and waste lubricating oil over an ex-situ dual catalytic beds of MgO and HZSM-5: Analytical PY-GC/MS study. *Energy Conversion and Management*, 139:222–231, 2017.

[131] Lei Nie, Bo Peng, and Xinli Zhu. Vapor-phase hydrodeoxygenation of guaiacol to aromatics over Pt/HBeta: Identification of the role of acid sites and metal sites on the reaction pathway. *ChemCatChem*, 10(5):1064–1074, 2018.

[132] Camila A Teles, Raimundo C Rabelo-Neto, Jerusa R de Lima, Lisiane V Mattos, Daniel E Resasco, and Fabio B Noronha. The effect of metal type on hydrodeoxygenation of phenol over silica supported catalysts. *Catalysis Letters*, 146(10):1848–1857, 2016.

[133] Adriana M Barrios, Camila A Teles, Priscilla M de Souza, Raimundo C Rabelo-Neto, Gary Jacobs, Burtron H Davis, Luiz EP Borges, and Fabio B Noronha. Hydrodeoxygenation of phenol over niobia supported Pd catalyst. *Catalysis Today*, 302:115–124, 2018.

[134] Priscilla M de Souza, Raimundo C Rabelo-Neto, Luiz EP Borges, Gary Jacobs, Burtron H Davis, Tawan Sooknoi, Daniel E Resasco, and Fabio B Noronha. Role of keto intermediates in the hydrodeoxygenation of phenol over Pd on oxophilic supports. *Acs Catalysis*, 5(2):1318–1329, 2015.

[135] Shin-Kuan Wu, Po-Chen Lai, Yu-Chuan Lin, Hou-Peng Wan, Hom-Ti Lee, and Ying-Hsi Chang. Atmospheric hydrodeoxygenation of guaiacol over alumina-, zirconia-, and silica-supported nickel phosphide catalysts. *ACS Sustainable Chemistry & Engineering*, 1(3):349–358, 2013.

[136] Teerawit Prasomsri, Manish Shetty, Karthick Murugappan, and Yuriy Román-Leshkov. Insights into the catalytic activity and surface modification of MoO_3 during the hydrodeoxygenation of lignin-derived model compounds into aromatic hydrocarbons under low hydrogen pressures. *Energy & Environmental Science*, 7(8):2660–2669, 2014.

[137] Patrick D Coan, Michael B Griffin, Peter N Ciesielski, and J Will Medlin. Phosphonic acid modifiers for enhancing selective hydrodeoxygenation over Pt catalysts: The role of the catalyst support. *Journal of Catalysis*, 372:311–320, 2019.

[138] Manish Shetty, Karthick Murugappan, William H Green, and Yuriy Roman-Leshkov. Structural properties and reactivity trends of molybdenum oxide catalysts supported on zirconia for the hydrodeoxygenation of anisole. *Acs Sustainable Chemistry & Engineering*, 5(6):5293–5301, 2017.

[139] Lei Nie, Priscilla M de Souza, Fabio B Noronha, Wei An, Tawan Sooknoi, and Daniel E Resasco. Selective conversion of m-cresol to toluene over bimetallic Ni–Fe catalysts. *Journal of Molecular Catalysis A: Chemical*, 388:47–55, 2014.

[140] Lujiang Xu, Zheng Han, Ying Zhang, and Yao Fu. In situ synthesis of molybdenum oxide@ N-doped carbon from biomass for selective vapor phase hydrodeoxygenation of lignin-derived phenols under H_2 atmosphere. *RSC advances*, 6(110):108217–108228, 2016.

[141] Xiwei Xu, Enchen Jiang, Yanhong Du, and Bosong Li. BTX from the gas-phase hydrodeoxygenation and transmethylation of guaiacol at room pressure. *Renewable Energy*, 96:458–468, 2016.

[142] Guofeng Zhou, Peter A Jensen, Duy M Le, Niels O Knudsen, and Anker D Jensen. Atmospheric hydrodeoxygenation of biomass fast pyrolysis vapor by MoO_3. *ACS Sustainable Chemistry & Engineering*, 4(10):5432–5440, 2016.

[143] Teerawit Prasomsri, Tarit Nimmanwudipong, and Yuriy Román-Leshkov. Effective hydrodeoxygenation of biomass-derived oxygenates into unsaturated hydrocarbons by MoO_3 using low H_2 pressures. *Energy & Environmental Science*, 6(6):1732–1738, 2013.

[144] Artit Ausavasukhi, Yi Huang, Anh T To, Tawan Sooknoi, and Daniel E Resasco. Hydrodeoxygenation of m-cresol over gallium-modified beta zeolite catalysts. *Journal of catalysis*, 290:90–100, 2012.

[145] Danni Gao, Christopher Schweitzer, Hyun Tae Hwang, and Arvind Varma. Conversion of guaiacol on noble metal catalysts: reaction performance and deactivation studies. *Industrial & Engineering Chemistry Research*, 53(49):18658–18667, 2014.

[146] Andrew J Foster, Phuong TM Do, and Raul F Lobo. The synergy of the support acid function and the metal function in the catalytic hydrodeoxygenation of m-cresol. *Topics in Catalysis*, 55(3-4):118–128, 2012.

[147] Priscilla M de Souza, Raimundo C Rabelo-Neto, Luiz EP Borges, Gary Jacobs, Burtron H Davis, Uschi M Graham, Daniel E Resasco, and Fabio B Noronha. Effect of zirconia morphology on hydrodeoxygenation of phenol over Pd/ZrO_2. *ACS Catalysis*, 5(12):7385–7398, 2015.

[148] Miguel Ángel González-Borja and Daniel E Resasco. Anisole and guaiacol hydrodeoxygenation over monolithic Pt–Sn catalysts. *Energy & Fuels*, 25(9):4155–4162, 2011.

[149] Feifei Yang, Hua Wang, Jinyu Han, Qingfeng Ge, and Xinli Zhu. Influence of Re addition to Ni/SiO_2 catalyst on the reaction network and deactivation during hydrodeoxygenation of m-cresol. *Catalysis Today*, 2018.

[150] Jie Zhang, Chuang Li, Weixiang Guan, Xiaozhen Chen, Xiao Chen, Chi-Wing Tsang, and Changhai Liang. Deactivation and regeneration study of a Co-promoted MoO_3 catalyst in hydrogenolysis of dibenzofuran. *Industrial & Engineering Chemistry Research*, 59(10):4313–4321, 2020.

[151] Ping Liu, Luyang Sun, Xinxin Jia, Chen Zhang, Wei Zhang, Yongji Song, Hong Wang, and Cuiqing Li. Efficient one-pot conversion of furfural into 2-methyltetrahydrofuran using non-precious metal catalysts. *Molecular Catalysis*, 490:110951, 2020.

[152] Joaquin Resasco, Feifei Yang, Tong Mou, Bin Wang, Phillip Christopher, and Daniel E Resasco. Relationship between atomic scale structure and reactivity of Pt catalysts: Hydrodeoxygenation of m-cresol over isolated Pt cations and clusters. *ACS Catalysis*, 10(1):595–603, 2019.

[153] Xuefang Lan, Emiel JM Hensen, and Thomas Weber. Hydrodeoxygenation of guaiacol over Ni_2P/SiO_2–reaction mechanism and catalyst deactivation. *Applied Catalysis A: General*, 550:57–66, 2018.

[154] Qi Lu, Cha-Jung Chen, Wesley Luc, Jingguang G Chen, Aditya Bhan, and Feng Jiao. Ordered mesoporous metal carbides with enhanced anisole hydrodeoxygenation selectivity. *ACS Catalysis*, 6(6):3506–3514, 2016.

[155] Gregory S Hutchings, Wesley Luc, Qi Lu, Yang Zhou, Dionisios G Vlachos, and Feng Jiao. Nanoporous Cu–Al–Co alloys for selective furfural hydrodeoxygenation to 2-methylfuran. *Industrial & Engineering Chemistry Research*, 56(14):3866–3872, 2017.

[156] Sunya Boonyasuwat, Taiwo Omotoso, Daniel E Resasco, and Steven P Crossley. Conversion of guaiacol over supported Ru catalysts. *Catalysis letters*, 143(8):783–791, 2013.

[157] HY Zhao, D Li, P Bui, and ST Oyama. Hydrodeoxygenation of guaiacol as model compound for pyrolysis oil on transition metal phosphide hydroprocessing catalysts. *Applied Catalysis A: General*, 391(1-2):305–310, 2011.

[158] Xinli Zhu, Lance L Lobban, Richard G Mallinson, and Daniel E Resasco. Bifunctional transalkylation and hydrodeoxygenation of anisole over a Pt/HBeta catalyst. *Journal of Catalysis*, 281(1):21–29, 2011.

[159] Yunhua Li, Juan Fu, and Binghui Chen. Highly selective hydrodeoxygenation of anisole, phenol and guaiacol to benzene over nickel phosphide. *RSC advances*, 7(25):15272–15277, 2017.

[160] S Ted Oyama, Tatsuki Onkawa, Atsushi Takagaki, Ryuji Kikuchi, Sou Hosokai, Yoshizo Suzuki, and Kyoko K Bando. Production of phenol and cresol from guaiacol on nickel phosphide catalysts supported on acidic supports. *Topics in Catalysis*, 58(4-6):201–210, 2015.

[161] Shin-Kuan Wu, Po-Chen Lai, and Yu-Chuan Lin. Atmospheric hydrodeoxygenation of guaiacol over nickel phosphide catalysts: Effect of phosphorus composition. *Catalysis letters*, 144(5):878–889, 2014.

[162] Xiwei Xu and Enchen Jiang. "btx" from guaiacol hdo under atmospheric pressure: effect of support and carbon deposition. *Energy & Fuels*, 31(3):2855–2864, 2017.

[163] Priscilla M de Souza, Lei Nie, Luiz EP Borges, Fabio B Noronha, and Daniel E Resasco. Role of oxophilic supports in the selective hydrodeoxygenation of m-cresol on Pd catalysts. *Catalysis letters*, 144(12):2005–2011, 2014.

[164] Andrew Ng Kay Lup, Faisal Abnisa, Wan Mohd Ashri Wan Daud, and Mohamed Kheireddine Aroua. Atmospheric hydrodeoxygenation of phenol as pyrolytic-oil model compound for hydrocarbon production using Ag/TiO_2 catalyst. *Asia-Pacific Journal of Chemical Engineering*, 14(2):e2293, 2019.

[165] Mark M Sullivan and Aditya Bhan. Acetone hydrodeoxygenation over bifunctional metallic–acidic molybdenum carbide catalysts. *ACS Catalysis*, 6(2):1145–1152, 2016.

[166] Andreas Eschenbacher, Alireza Saraeian, Brent H Shanks, Peter Arendt Jensen, Chengxin Li, Jens Øllgaard Duus, Asger Baltzer Hansen, Uffe Vie Mentzel, Ulrik Birk Henriksen, Jesper Ahrenfeldt, et al. Enhancing bio-oil quality and energy recovery by atmospheric hydrodeoxygenation of wheat straw pyrolysis vapors using Pt and Mo-based catalysts. *Sustainable Energy & Fuels*, 4(4):1991–2008, 2020.

[167] Yunwu Zheng, Jida Wang, Can Liu, Yi Lu, Xu Lin, Wenbin Li, and Zhifeng Zheng. Optimizing Ni–Ce/HZSM-5 catalysts for ex-situ conversion of pine wood pyrolytic vapours into light aromatics and phenolic compounds. *International Journal of Hydrogen Energy*, 2020.

[168] Tu Nguyet Pham, Dachuan Shi, Tawan Sooknoi, and Daniel E Resasco. Aqueous-phase ketonization of acetic acid over Ru/TiO_2/carbon catalysts. *Journal of catalysis*, 295:169–178, 2012.

[169] R Pestman, RM Koster, JAZ Pieterse, and Vladimir Ponec. Reactions of carboxylic acids on oxides: 1. selective hydrogenation of acetic acid to acetaldehyde. *Journal of catalysis*, 168(2):255–264, 1997.

[170] NM Deraz. The comparative jurisprudence of catalysts preparation methods: i. precipitation and impregnation methods. *J. Ind. Environ. Chem*, 2(1):19–21, 2018.

[171] Completely Revised Second, Enlarged Edition, Gerhard Ertl, Helmuth Knözinger, Ferdi Schüth, Jens Weitkamp, and Wiley-VCH Verlag GmbH& Co KGaA. Handbook of heterogeneous catalysis. *Chem. Phys*, 22:377, 1989.

[172] NM Deraz. The comparative jurisprudence of catalysts preparation methods: Ii. deposition-precipitation and adsorption methods. *Journal of Industrial Environmental Chemistry*, 2(2):1–3, 2018.

[173] N Pernicone and F Traina. Catalyst activation by reduction. In *Studies in Surface Science and Catalysis. Vol. 3.\ Proc. Conf.\, Louvain-la-Neuve, Belgium*, number 1979, pages 321–351, 1978.

[174] Ib Chorkendorff and Johannes W Niemantsverdriet. *Concepts of modern catalysis and kinetics*. John Wiley & Sons, 2017.

[175] Samikannu Ajaikumar, Johan Ahlkvist, William Larsson, Andrey Shchukarev, A-R Leino, K Kordas, and J-P Mikkola. Oxidation of α-pinene over gold containing bimetallic nanoparticles supported on reducible TiO_2 by deposition-precipitation method. *Applied Catalysis A: General*, 392(1-2):11–18, 2011.

[176] K Chiang, R Amal, and T Tran. Photocatalytic degradation of cyanide using titanium dioxide modified with copper oxide. *Advances in Environmental Research*, 6(4):471–485, 2002.

[177] Laura Clarizia, Giuseppe Vitiello, Deborah Katia Pallotti, Brigida Silvestri, Mallikarjuna Nadagouda, Stefano Lettieri, Giuseppina Luciani, Roberto Andreozzi, Pasqualino Maddalena, and Raffaele Marotta. Effect of surface properties of copper-modified commercial titanium dioxide photocatalysts on hydrogen production through photoreforming of alcohols. *International Journal of Hydrogen Energy*, 42(47):28349–28362, 2017.

[178] MD Norman et al. Catalytic and physicochemical characterizations of novel oxide-supported copper catalysts. part 1.—hydrosol-prepared Cu/TiO_2 and effects of pre-reduction on hydrogenation and oligomerization of acetone. *Journal of Materials Chemistry*, 3(7):743–750, 1993.

[179] S Rahimnejad, S Rahman Setayesh, and MR Gholami. A credible role of copper oxide on structure of nanocrystalline mesoporous titanium dioxide. *Journal of the Iranian Chemical Society*, 5(3):367–374, 2008.

[180] Lifeng Zhang, Xiaotao Bi, and John R Grace. Measurements of electrostatic charging of powder mixtures in a free-fall test device. *Procedia engineering*, 102:295–304, 2015.

[181] Sunggyu Lee and Yatish T Shah. *Biofuels and bioenergy: processes and technologies*. CRC Press, 2012.

Appendix A

Characteristics of pyrolysis reactors

Pyrolyzer	Status (units)	Bio-oil yield (wt.\%)	Operational complexity
Fixed bed	Lab & pilot scale	75	Medium
Fluidized bed	Lab & pilot scale	75	Medium
Recirculating bed	Lab & pilot scale	75	High
Rotating cone	Demo plant	70	Medium
Abalative	Lab & pilot scale	75	High
Auger reactor	Lab & pilot scale	70	Low
Vaccum	Lab & pilot scale	60	High

Pyrolyzer	Particle size	Biomass variability	Scale-up	Inert gas flow rate
Fixed bed	Large	High	Hard	Low
Fluidized bed	Small	Low	Easy	High
Recirculating bed	Medium	Low	Hard	High
Rotating cone	Medium	High	Medium	Low
Abalative	Large	High	Hard	Low
Auger reactor	Medium	High	Easy	Low
Vaccum	Large	Medium	Hard	Low

Table A.1: Features of pyrolysis reactors [1]

Appendix B

Synthesis of carbon-carbon coupling catalyst

S.No	Catalyst	Loading (wt.%) over TiO2	Precursor with hydration (g)	water required for dissolving chemical precursor (ml) *
1	Cu/TiO_2	0.5	0.2562	1.72
2	Cu/TiO_2	1	0.5125	1.68
3	Cu/TiO_2	3	1.5375	1.55
4	Cu/TiO_2	7	3.5874	1.28
5	Ru/TiO_2	1	0.9192	1.73

*: Hydration water was subtracted from the total water required to dissolve the metal precursor

Table B.1: Required water and chemical precursor loading during catalyst preparation via incipient wetness method

Appendix C

GC calibiration and bio-oil

C.1 Gas composition for calibration of GC-TCD/FID detectors

Gas name	Composition, mol-%
Methane	1
Ethane	0.101
Ethene	0.101
Propane	0.1
Propene	0.1
Butane-n	0.15
Pentane-n	0.15
Hexane-n	0.098
Carbon monoxide	30.4
Hydrogen	63.8
carbon dioxide	1
Nitrogen	3

Table C.1: Gas composition of the cylinder used for GC/FID/TCD calibration

C.2 Low quantity of bio-oil for GC analysis

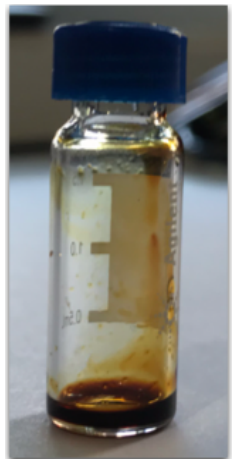

Figure C.1: Low quantity of bio-oil for GC-MS and GC-FID analysis

C.3 Calibration graphs for standard chemicals

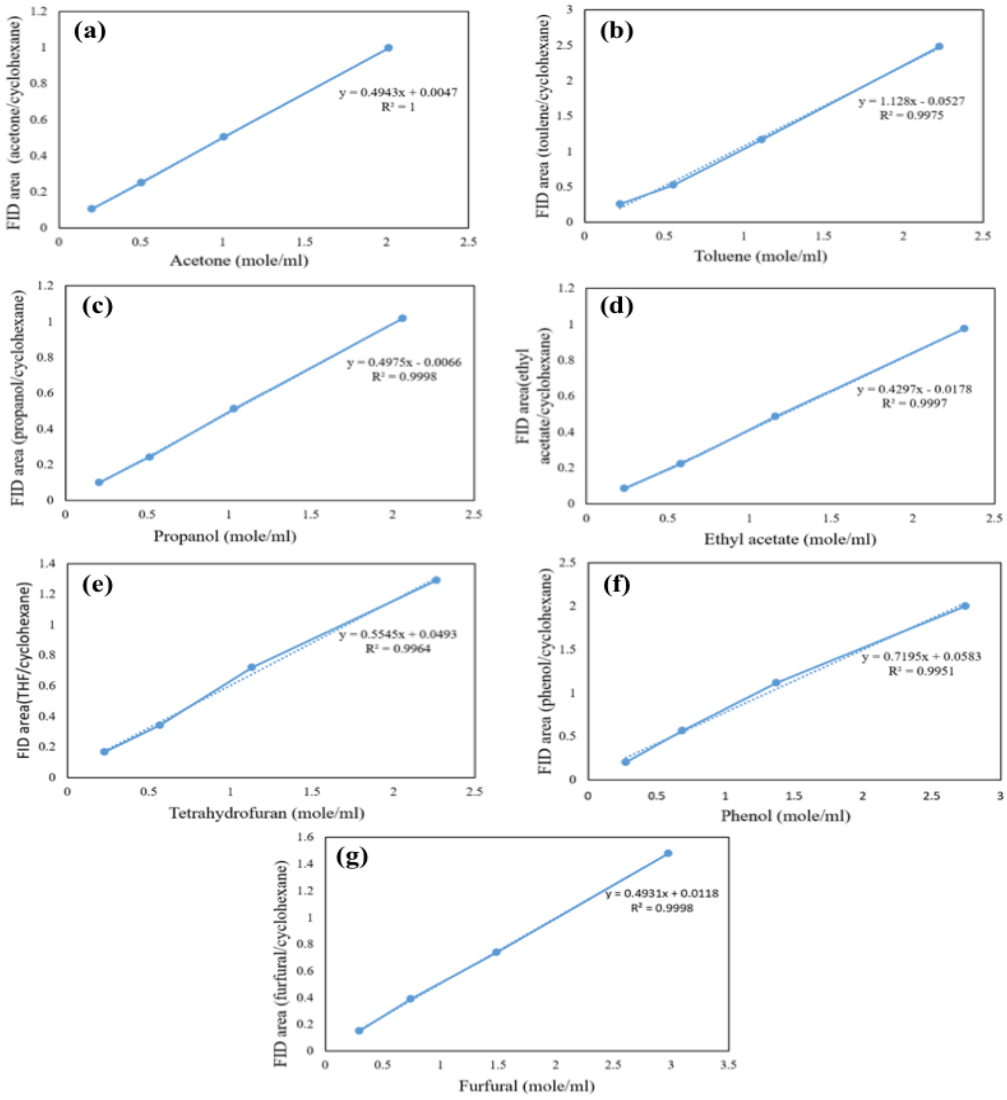

Figure C.2: Response factor for standard chemicals

C.4 Model components quantified in GC-FID for liquid quantification

Standard chemicals	Response factor
Acetone	0.50
Toulene	1.06
Propanol	0.48
Ethyl acetate	0.42
Tetrahydofuran	0.58
Phenol	0.74
Furfural	0.51

Table C.2: Response factor for standard bio-oil components

Appendix D

MFC calibiration

D.1 Digital flow meter for mass flow controller calibration

Figure D.1: Agilent digital flow meter

D.2 Calibration of N_2 and H_2 mass flow controller

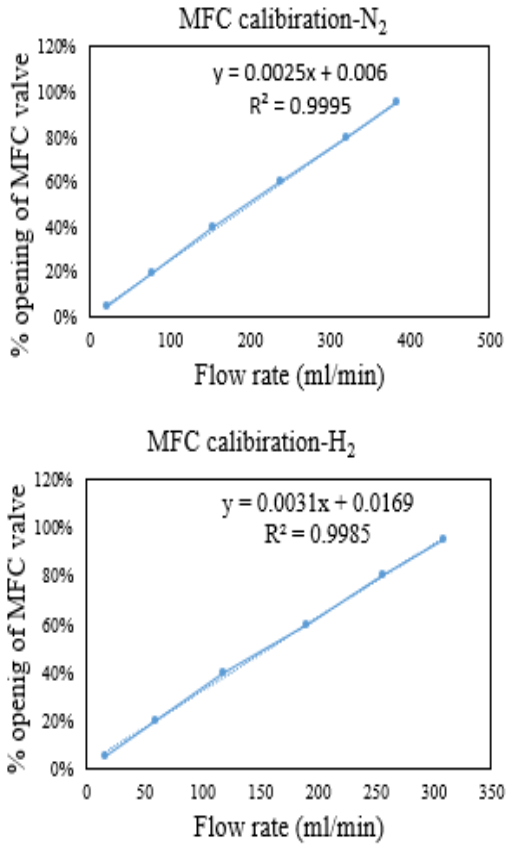

Figure D.2: Mass flow controller calibration for H_2 and N_2

Appendix E

Swagelok tubes and fittings used in developing setup

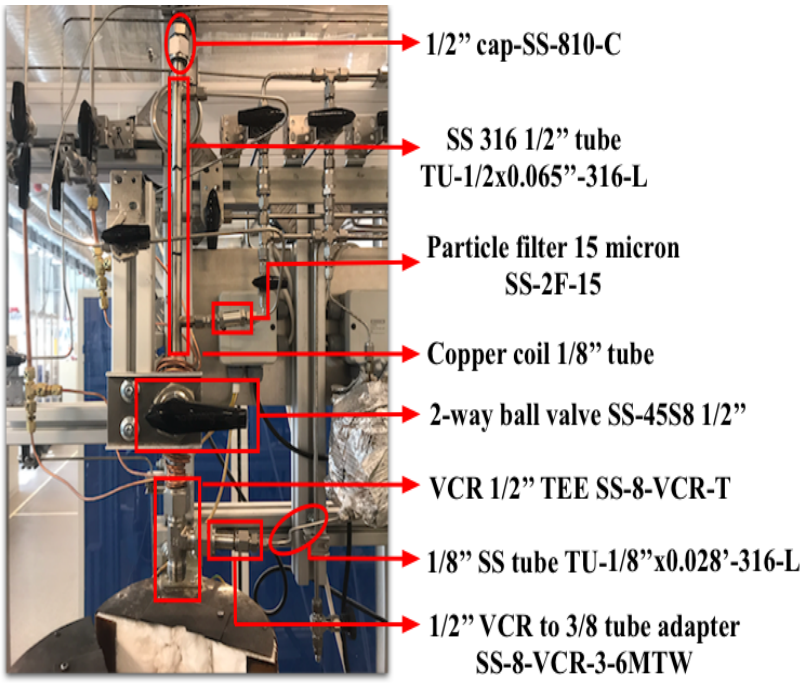

Figure E.1: Parts of biomass feeding compartment

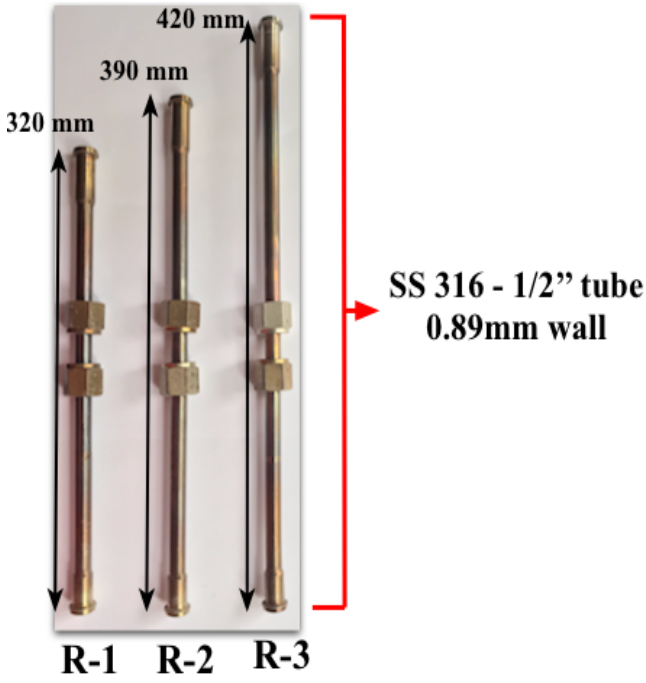

Figure E.2: Reactor tubing

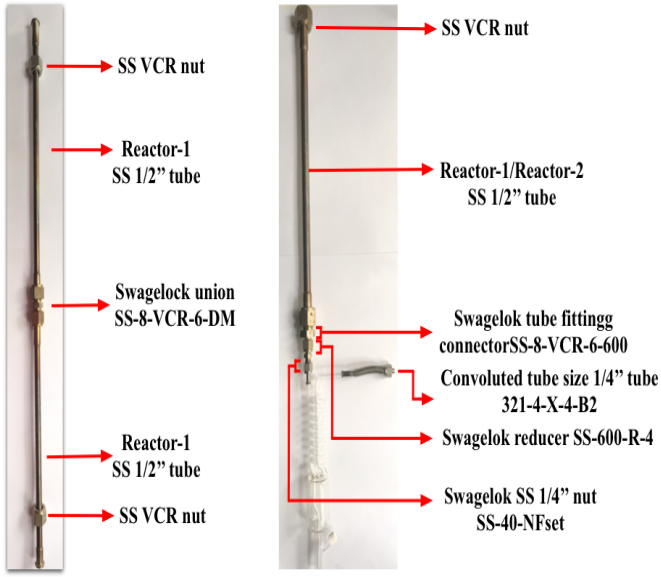

Figure E.3: Reactor tubing and condenser

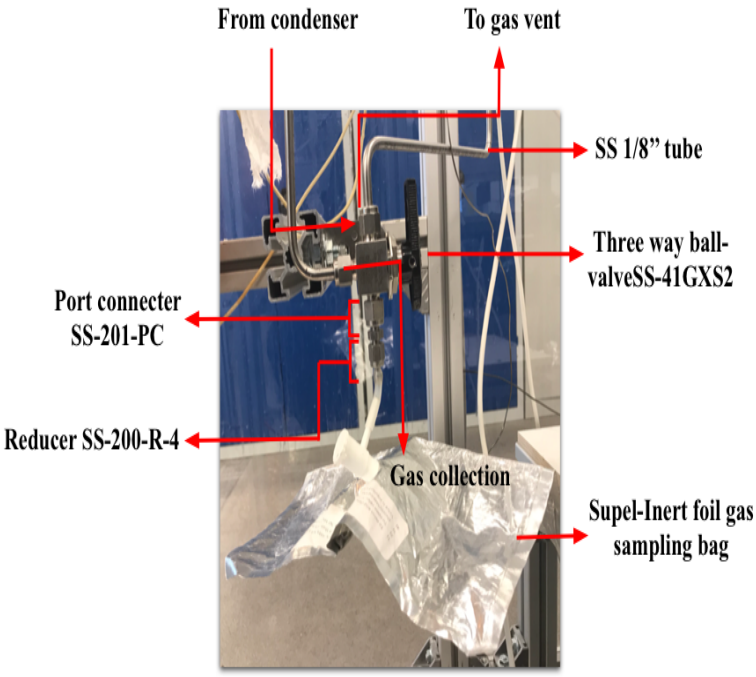

Figure E.4: Gas sampling zone

Figure E.5: Other accessories

Appendix F

Biomass calibration

	Mesh number	Wt. of biomass loaded (g)	Wt. of loading device (g)	Wt. of loading device exiting feeding zone (g) [a,b]	Loss of biomass (wt%)
Trial-1	1	0.1554	2.2464	7.0006	**0.5045**
	2	0.1661	2.4845		
	3	0.1344	2.2720		
Total		**0.4559**	**7.0029**		
Trial-2	1	0.1656	2.4877	6.9712	**0.5853**
	2	0.1169	2.2507		
	3	0.1446	2.2353		
Total		**0.4271**	**6.9737**		
Trial-3	1	0.1264	2.2587	6.9545	**0.5285**
	2	0.1611	2.4790		
	3	0.1288	2.2190		
Total		**0.4163**	**6.9567**		

a: The biomass loaded cylindrical mesh is collected in an air bag after exiting the feeding zone (Version-).
b: The weight of the air-bag utilized to collect the cylindrical mesh is not shown. The reported valve are subtracted from the additional weight from air bag.

Table F.1: Biomass calibration

Appendix G

Interconnection between the C-1 condenser and reactor-1/reactor-2

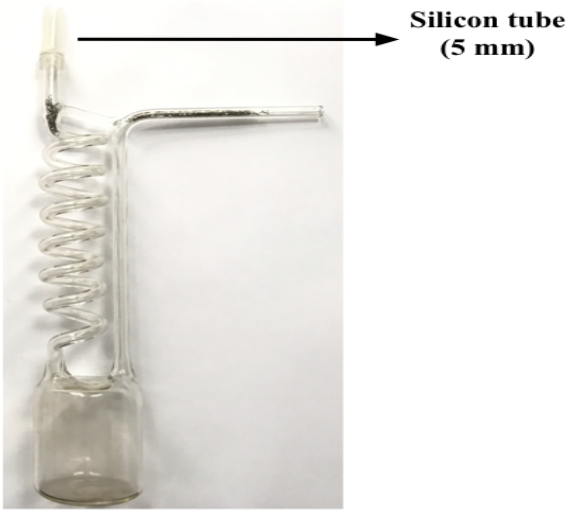

Figure G.1: Silicon tube for connecting reactor and C-1 condenser

Appendix H

Poor condensation by spiral/RBF condenser

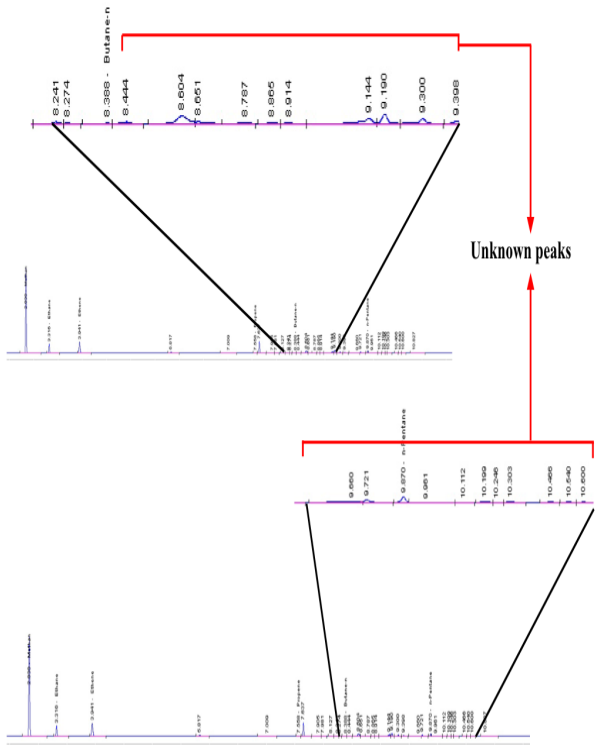

Figure H.1: Unknown chemical compound from GC chromatogram